
Electronic Thesis and Dissertation Repository

1-25-2017 12:00 AM

Numerical Simulation of Air Flow in Aeroengine Compressors

Shady Mohamed Mohamed Ali, *The University of Western Ontario*

Supervisor: Prof. Chao Zhang, *The University of Western Ontario*

Joint Supervisor: Prof. Eric Savory, *The University of Western Ontario*

A thesis submitted in partial fulfillment of the requirements for the Doctor of Philosophy degree
in Mechanical and Materials Engineering

© Shady Mohamed Mohamed Ali 2017

Follow this and additional works at: <https://ir.lib.uwo.ca/etd>



Part of the [Aerodynamics and Fluid Mechanics Commons](#)

Recommended Citation

Ali, Shady Mohamed Mohamed, "Numerical Simulation of Air Flow in Aeroengine Compressors" (2017).
Electronic Thesis and Dissertation Repository. 4392.

<https://ir.lib.uwo.ca/etd/4392>

This Dissertation/Thesis is brought to you for free and open access by Scholarship@Western. It has been accepted for inclusion in Electronic Thesis and Dissertation Repository by an authorized administrator of Scholarship@Western. For more information, please contact wlsadmin@uwo.ca.

Abstract

The performance of an aeroengine is influenced by the performance of the compressor system. A typical compressor consists of multistage axial compressors followed by a centrifugal stage. Here, a high-speed centrifugal and an axial stage are investigated in terms of turbulence modelling, flow blockage and rotor-stator (R-S) gap using the commercial software ANSYS CFX.

The curvature corrected Shear stress transport (SST-CC) model of Smirnov and Menter is investigated for the first time in a high-speed centrifugal stage in terms of curvature and rotation effects. The SST-CC predictions are compared with the standard SST, Speziale, Sarkar, and Gatski Reynolds stress model (RSM-SSG) and the experimental data in terms of the global performance as well as the velocity profiles at the impeller-diffuser interface. The comparisons show that SST-CC has the best agreement with the experiments at choke condition while SST has better performance at the stall condition. The production term shows the expected sensitivity to the convex and concave curvatures.

A new method to quantify blockage for both axial and centrifugal compressors is developed. Both steady and unsteady simulations are used to examine the flow blockage in the axial transonic stage. The variation of the rotor tip blockage with respect to the blade loading shows good agreement with previous studies. The total planar blockage indicates that stall might initiate at the stator trailing edge. The differences between the steady and unsteady predictions are mainly attributed to the local differences in the total pressure profiles at the inlet guide vanes–rotor interface.

It was previously argued that reducing the R-S gap improves the efficiency of axial compressors due to reduced viscous mixing of the rotor wake. However, the current simulations show that the smallest R-S gap has the highest levels of total pressure losses within the stator passage and the highest levels of unsteady stator forces at reduced mass flow rates. The unsteadiness in the stator flow field is attributed to the larger stator suction surface boundary layer separation associated with the smallest gap. The smallest R-S gap reduces the viscous mixing of the wake at the expense of the efficiency.

Keywords

CFD, centrifugal compressor, curvature correction, axial transonic compressor, blockage, rotor-stator gap, time transformation, rotor wake decay.

Co-Authorship Statement

This doctoral thesis is prepared in accordance with the regulations for an Integrated-Article thesis stipulated by the School of Graduate and Postdoctoral Studies (SGPS) at the University of Western Ontario. This document includes co-authored articles where the contribution of each author will be explicitly stated below.

Chapter 2: Investigation of the performance of turbulence models with respect to high flow curvature in centrifugal compressors

The numerical simulations were carried out by Shady Ali and Kevin Elliott with guidance from Profs. Chao Zhang, Eric Savory, Robert Martinuzzi and Dr. William Lin. The literature review was completed by Shady Ali and Kevin Elliott. The data analysis and principal discussion points were completed by Shady Ali. Profs. Eric Savory, Chao Zhang, Robert Martinuzzi, Dr. William Lin, and Kevin Elliott supervised the work, provided advice, read the draft versions, and suggested revisions. This chapter was published as *ASME Journal of Fluids Engineering* **138**(5), 051101-051101-10, FE-15-1215, 2015.

Chapter 3: Numerical investigation of blockage development in an aeroengine transonic axial compressor stage

The numerical simulations were carried out by Shady Ali with guidance from Profs. Chao Zhang and Eric Savory. The literature and data analysis were completed by Shady Ali. Profs. Eric Savory and Chao Zhang supervised the work, provided advice, read the draft versions, and suggested revisions. A version of this chapter has been prepared for submission to the *ASME Journal of Turbomachinery*, 2017, and is presently being pre-reviewed by Pratt and Whitney Canada.

Chapter 4: Numerical simulation of the influence of rotor-stator axial gap on the unsteady 3D flow field in a single stage axial compressor

The numerical simulations were carried out by Shady Ali with guidance from Profs. Chao Zhang and Eric Savory. The literature and data analysis were completed by Shady Ali. Profs. Eric Savory and Chao Zhang supervised the work, provided advice, read the draft

versions, and suggested revisions. A version of this chapter is being prepared for submission to the *ASME Journal of Turbomachinery*, 2017, following a pre-review by Pratt and Whitney Canada.

Acknowledgments

I would like to thank my supervisors Prof. Chao Zhang and Prof. Eric Savory for their great assistance and support during my research. I am grateful for their patience and encouragement which aided the completion of this work. I also would like to thank Prof. Robert Martinuzzi from the University of Calgary for his guidance and assistance on running simulations on WestGrid. I want to acknowledge my advisory committee members Prof. Girma Bitsuamlak and Prof. Anthony Straatman for providing insight into the success of this work. I would like to thank Jason Bourgeois for assisting in the simulation setup. Thanks are due to WestGrid and SHARCNET for providing the computational resources for running the simulations in this research. My gratitude is expressed to Pratt and Whitney Canada (P&WC) and MITACS for giving me the opportunity to work on this project.

I would also like to thank my colleagues in the Advanced Fluid Mechanics (AFM) research group for providing an encouraging and friendly environment. I am thankful to Dr. William Lin and Kevin Elliott for reviewing and co-authoring the second chapter of this thesis. Finally, many thanks to my parents and brothers for their help and support along the way.

Table of Contents

| | |
|--|-------|
| Abstract | ii |
| Co-Authorship Statement..... | iv |
| Acknowledgments..... | vi |
| List of Tables | x |
| List of Figures | xi |
| List of Appendices | xviii |
| List of Abbreviations | xix |
| List of Symbols | xxi |
| Chapter 1 | 1 |
| 1 Introduction | 1 |
| 1.1 Geometry and description of compressors..... | 3 |
| 1.1.1 Centrifugal compressors | 3 |
| 1.1.2 Axial transonic compressors | 4 |
| 1.1.3 Turbomachinery notations and conventions | 5 |
| 1.2 Governing equations for compressible turbulent flow..... | 12 |
| 1.3 Turbulence modelling with respect to curvature and rotation | 15 |
| 1.4 Blockage in compressors | 16 |
| 1.5 The influence of rotor-stator gap on the aerodynamic performance of a transonic compressor stage..... | 20 |
| 1.6 Objectives | 21 |
| 1.7 Thesis organization | 22 |
| 1.8 References..... | 24 |
| Chapter 2..... | 27 |
| 2 Investigation of the performance of turbulence models with respect to high flow curvature in centrifugal compressors | 27 |

| | | |
|----------------|--|----|
| 2.1 | Introduction..... | 27 |
| 2.2 | Geometry and compressor stage details..... | 30 |
| 2.3 | Numerical method..... | 31 |
| 2.4 | Turbulence modelling..... | 32 |
| 2.5 | Results and discussion | 36 |
| 2.5.1 | Comparison with experimental data | 37 |
| 2.5.2 | Investigation of the production multiplier, f_{r1} | 42 |
| 2.6 | Conclusions..... | 49 |
| 2.7 | References..... | 51 |
| Chapter 3..... | | 53 |
| 3 | Numerical investigation of blockage development in an aeroengine transonic axial compressor stage | 53 |
| 3.1 | Introduction..... | 53 |
| 3.2 | Geometry and numerical method..... | 55 |
| 3.3 | Grid and time independence study..... | 58 |
| 3.4 | Performance characteristics of the compressor stage | 62 |
| 3.5 | Quantification of blockage..... | 63 |
| 3.6 | Comparison with previous work..... | 65 |
| 3.7 | Blockage development in the stage..... | 69 |
| 3.8 | The unsteadiness of the flow in the stage | 71 |
| 3.9 | The global performance with respect to the interface type..... | 73 |
| 3.10 | Conclusions..... | 76 |
| 3.11 | References..... | 78 |
| Chapter 4..... | | 81 |
| 4 | Numerical simulation of the influence of rotor-stator axial gap on the unsteady 3D flow field in a single stage axial compressor | 81 |

| | | |
|-----|---|-----|
| 4.1 | Introduction..... | 81 |
| 4.2 | Numerical procedure..... | 86 |
| 4.3 | Effect of the axial gap on the global and local performance | 89 |
| 4.4 | Effect on the stator forces | 95 |
| 4.5 | Effect on rotor wake decay | 97 |
| 4.6 | Recovery of the rotor wake..... | 103 |
| 4.7 | Conclusions..... | 106 |
| 4.8 | References..... | 107 |
| | Chapter 5..... | 111 |
| 5 | Conclusions and recommendations for future work | 111 |
| 5.1 | Conclusions..... | 111 |
| 5.2 | Recommendations for future work | 114 |
| | Appendices..... | 116 |
| | Appendix A..... | 116 |
| | Curriculum Vitae | 124 |

List of Tables

| | |
|---|----|
| Table 2-1 Closure coefficients for the turbulence models | 36 |
| Table 2-2 Differences between the CFD results and experimental data for the tangential and radial velocities at the mixing plane..... | 41 |
| Table 3-1 Mesh data for each component..... | 58 |
| Table 3-2 Grid independence results. The values are based on the RMS differences normalized by the fine mesh mean profiles, except for the flow angle. | 61 |
| Table 3-3 RMS of the change in time step resolution. The values are normalized by their mean profiles at 200 ts. | 61 |
| Table 4-1 Mesh data for each component for different R-S spacing configurations..... | 89 |

List of Figures

| | |
|---|----|
| Figure 1-1 Types of aeroengines, (a) turboprop, (b) turbojet and (c) turbofan [1]..... | 2 |
| Figure 1-2 Centrifugal compressor stage | 4 |
| Figure 1-3 Axial compressor stage | 5 |
| Figure 1-4 Centrifugal compressor impeller passage showing the turbomachinery coordinates and velocity diagrams..... | 7 |
| Figure 1-5 Axial compressor stage showing (a) the turbomachinery coordinates and (b) velocity diagrams at a midspan section | 8 |
| Figure 1-6 Velocity components used in turbomachinery in (a) isometric view and (b) meridional view | 9 |
| Figure 1-7 Two dimensional velocity profile on a flat plate showing the boundary layer and the displacement thickness | 17 |
| Figure 1-8 Calculation of blockage, (a) main flow mass flux streamwise angle at the rotor mid-chord. The scattered data represent the relative velocity angle and the surface fit represents the main flow velocity angle, (b) a streamwise plane showing defect and core regions and (c) inviscid main flow flux surface fit. The scattered data represent the main flow flux and the surface fit represents the inviscid main flow flux. | 19 |
| Figure 1-9 Axial velocity contours at a midspan plane showing the rotor wake and the rotor-stator gap..... | 21 |
| Figure 2-1 Geometry of the compressor stage | 31 |
| Figure 2-2 Centrifugal compressor computational domain | 32 |
| Figure 2-3 Pressure characteristic for the SST, SST-CC, and RSM-SSG models as compared to the experimental data. The bars on the experimental points indicate experimental uncertainty..... | 38 |

Figure 2-4 Efficiency characteristic for the SST, SST-CC, and RSM-SSG models as compared to the experimental data. The bars on the experimental points indicate experimental uncertainty..... 39

Figure 2-5 Circumferential velocity at the mixing plane, normalized by the blade tip speed. The bars on the experimental points indicate experimental uncertainty..... 40

Figure 2-6 Radial velocity at the mixing plane, normalized by the blade tip speed. The bars on the experimental points indicate experimental uncertainty. 41

Figure 2-7 Normalized axial velocity contours (C_x) at the diffuser exit; (a) experimental data [1], (b) SST, (c) SST-CC, and (d) RSM-SSG [17] 43

Figure 2-8 Normalized circumferential velocity (C_θ) contours at the diffuser exit; (a) experimental data [1], (b) SST, (c) SST-CC, and (d) RSM-SSG [17]..... 43

Figure 2-9 Streamwise planes and lines of interest and corresponding f_{rI} contours and radius of curvature component; (a) planes and lines shown on the impeller, (b) curvature of interest and corresponding f_{rI} at $\xi = 0.21$, (c) curvature of interest and corresponding f_{rI} at $\xi = 0.65$, and (d) curvature of interest and corresponding f_{rI} at $\xi = 0.96$ 45

Figure 2-10 Profiles of turbulence production and production multiplier; (a) along the circumferential direction at $\xi = 0.21$ and $\xi = 0.5$, (b) along the spanwise direction at $\xi = 0.65$, and $\theta = 0.5$ and (c) along circumferential direction at $\xi = 0.96$, and $\theta = 0.5$ 49

Figure 2-11 Contours of r^* and \tilde{r} at planes; (a, b) $\xi = 0.21$, (c, d) $\xi = 0.65$, and (e, f) $\xi = 0.96$ 49

Figure 3-1 The computational domain of the axial compressor stage; (a) intake section, inlet guide vane (IGV), rotor (R), stator (S) and variable exit nozzle, (b) a close-up view of the main components showing the inlet and outlet planes for each component and the leading and trailing edge planes (RLE, RTE, SLE and STE). The streamwise, circumferential and spanwise directions are represented by ξ , θ and ζ , respectively. 57

| | |
|---|----|
| Figure 3-2 Grid independence test at the rotor and stator trailing edges (RTE and STE) for a low mass flow point | 60 |
| Figure 3-3 Time independence test showing the static pressure normalized by the total pressure at the inlet versus the time normalized by the rotor blade pass time (T_{RBP}) at (a) rotor tip leading edge and (b) stator leading edge tip | 61 |
| Figure 3-4 Performance characteristic for the normalized pressure ratio (PR/PR_{ref}) and isentropic efficiency ($\eta_{is} - \eta_{is,ref}$) vs. the normalized mass flow rate (\dot{m}/\dot{m}_{ref}). The abbreviations MP, TT, HE and PPR stand for mixing plane, time transformation, high efficiency and peak pressure ratio. The marked operating points are used in Section 3.6 | 63 |
| Figure 3-5 Variation of blockage parameter vs. loading parameter and comparison with Khalid [8]. The operating points are illustrated in Figure 3-4. | 67 |
| Figure 3-6 Variation of blockage parameter vs. loading parameter and comparison with Khalsa [9] and Khalid <i>et al.</i> [10]. The shaded area represents the region of experimental uncertainty of the measurements. | 68 |
| Figure 3-7 Contours of the circumferential blockage at different normalized streamwise and spanwise locations for; (a) MP-HE, (b) MP-PPR, (c) TT-HE, (d) TT-PPR | 70 |
| Figure 3-8 Contours of Mach number at 75% span for; (a) MP-PPR and (b) TT-PPR.... | 70 |
| Figure 3-9 Total blockage development along the stage | 71 |
| Figure 3-10 Variation of the blockage parameter against Khalid's loading parameter at TT-PPR at different time steps..... | 72 |
| Figure 3-11 Variation of total blockage along the streamwise position at TT-PPR at different rotor positions..... | 73 |
| Figure 3-12 Streamwise profile of the total pressure at HE..... | 74 |
| Figure 3-13 Spanwise profile of the circumferential average of the total pressure at HE | 74 |

| | |
|--|----|
| Figure 3-14 Total pressure contours for the isolated rotor steady simulations at the rotor inlet, mid-streamwise location and outlet | 75 |
| Figure 3-15 Total pressure ratio for each isolated rotor simulation with respect to the TT_{in} - TT_{out} case..... | 76 |
| Figure 4-1 The computational domain of the axial compressor stage; (a) intake section, inlet guide vane (IGV), rotor (R), stator (S) and variable exit nozzle, (b) a close-up view of the mesh at the hub section for the three R-S axial gaps used. The axial spacing is normalized by the rotor chord at the hub section. The highlighted line represents the location of the rotor-stator interface. | 88 |
| Figure 4-2 Global performance of the compressor; (a) total pressure ratio and (b) total-to-total efficiency from steady (MP) and unsteady (TT) simulations | 90 |
| Figure 4-3 The variation of the total efficiency with axial gap from the literature and present CFD work at (a) the HE point and (b) PPR point..... | 91 |
| Figure 4-4 Global total pressure loss coefficient for (a,b) the gap, (c,d) the stator and (e,f) the gap and stator combined. The left and right column figures are calculated at the HE and PPR points, respectively. | 92 |
| Figure 4-5 Total pressure loss coefficient at 50% spanwise section for (a,b) the gap, (c,d) the stator and (e,f) the gap and stator combined. The left and right column figures are calculated at the HE and PPR points, respectively. | 94 |
| Figure 4-6 The variation of the total pressure loss coefficients at the STE with R-S axial gap. The results are obtained from the present CFD predictions at $\zeta = 0.25, 0.50$ and 0.75 as well as Yu and Lakshminarayana [12]. | 94 |
| Figure 4-7 The first Fourier harmonic of the streamwise component (a,b) and tangential component (c,d) of the forces on the stator blade at spanwise locations of 1%, 25%, 50%, 75% and 99%. The left and right column figures are calculated at the HE and PPR points, respectively. | 96 |

| | |
|--|-----|
| Figure 4-8 Surface streamlines of the average velocity on the stator blade suction surface for (a) small gap, (b) medium gap and (c) large gap at the PPR point | 96 |
| Figure 4-9 The variation of the first Fourier harmonics of the (a) axial and (b) tangential forces on the stator blade with R-S axial gap. The results are obtained from the CFD predictions at $\zeta = 0.25, 0.50$ and 0.75 , Gallus <i>et al.</i> [10] and Yu and Lakshminarayana [12]. | 97 |
| Figure 4-10 Illustration of wake decay mechanisms due to (a) viscous mixing and (b) viscous mixing and stretching..... | 99 |
| Figure 4-11 The wake profile at a midpitch line against normalized time. The time is normalized by the rotor blade passing period and the velocity is normalized by the rotor tip speed. | 100 |
| Figure 4-12 The wake decay along the midpitch of the stator passage at (a) HE and (b) PPR. The CFD data are plotted for small (S), medium (M), large (L) axial gaps and without the stator (N). The experimental data are obtained from [16] for a NASA 37 stator and the model (Mod) plots are obtained from Equation 4-3. | 101 |
| Figure 4-13 Wake decay model predictions due to total decay (lines), inviscid stretching (triangular markers) and viscous mixing (circular markers) for small and large axial gaps at (a) HE and (b) PPR | 102 |
| Figure 4-14 Wake decay CFD predictions using the rotor trailing edge profile as the initial condition at (a) HE and (b) PPR. The locations of the stator trailing edge are illustrated for each axial gap configuration. | 102 |
| Figure 4-15 Reversible wake recovery across the gap and the stator passage for small (S), medium (M), large (L) and no stator (N) at (a) HE and (b) PPR points..... | 105 |
| Figure 4-16 Sources of losses in the stator passage at the midspan section for (a) HE and (b) PPR points..... | 105 |

Figure A-1 Standard deviation of the pressure on the rotor and stator blades and on their hub and shroud at HE and PPR. The values are normalized by the rotor inlet total pressure. 116

Figure A-2 Standard deviation of the entropy within the rotor and stator passages at HE and PPR. The values are normalized by the rotor inlet entropy. 117

Figure A-3 Standard deviation of the velocity magnitude within the rotor and stator passages at HE and PPR. The values are normalized by the rotor inlet. 118

Figure A-4 Total pressure loss coefficient at 1% spanwise section for (a,b) the gap, (c,d) the stator and (e,f) the gap and stator combined. The left and right column figures are calculated at the HE and PPR points, respectively. 119

Figure A-5 Total pressure loss coefficient at 25% spanwise section for (a,b) the gap, (c,d) the stator and (e,f) the gap and stator combined. The left and right column figures are calculated at the HE and PPR points, respectively. 119

Figure A-6 Total pressure loss coefficient at 75% spanwise section for (a,b) the gap, (c,d) the stator and (e,f) the gap and stator combined. The left and right column figures are calculated at the HE and PPR points, respectively. 120

Figure A-7 Total pressure loss coefficient at 99% spanwise section for (a,b) the gap, (c,d) the stator and (e,f) the gap and stator combined. The left and right column figures are calculated at the HE and PPR points, respectively. 120

Figure A-8 The time average of the streamwise component (a b) and tangential component (c,d) of the total forces on the stator blade. The left and right column figures are calculated at the HE and PPR points, respectively. 121

Figure A-9 The first Fourier harmonic of the streamwise component (a,b) and tangential component (c,d) of the total forces on the stator blade. The left and right column figures are calculated at the HE and PPR points, respectively. 121

Figure A-10 The second Fourier harmonic of the streamwise component (a,b) and tangential component (c,d) of the total forces on the stator blade. The left and right column figures are calculated at the HE and PPR points, respectively. 122

Figure A-11 The time average of the streamwise component (a,b) and tangential component (c,d) of the forces on the stator blade at spanwise locations of 1%, 25%, 50%, 75% and 99%. The left and right column figures are calculated at the HE and PPR points, respectively. 122

Figure A-12 The second Fourier harmonic of the streamwise component (a,b) and tangential component (c,d) of the forces on the stator blade at spanwise locations of 1%, 25%, 50%, 75% and 99%. The left and right column figures are calculated at the HE and PPR points, respectively. 123

List of Appendices

| | |
|------------------|-----|
| Appendix A | 116 |
|------------------|-----|

List of Abbreviations

| | |
|--------|-------------------------------------|
| Avg | Time-averaged |
| BLK | Blockage parameter |
| CC | Curvature correction |
| CFD | Computational Fluid Dynamics |
| COF | Cutoff coefficient |
| EVM | Eddy viscosity model |
| H1, H2 | First and second harmonics |
| HE | High efficiency operating point |
| IGV | Inlet guide vanes |
| L | Large axial gap |
| LdP | Loading parameter (-) |
| LDV | Laser Doppler Velocimetry |
| M | Medium axial gap |
| MP | Mixing plane |
| N | No stator simulation |
| PPR | Peak pressure ratio operating point |
| PR | Total-to-total pressure ratio |
| PS | Pressure surface |
| PT | Profile transformation |

| | |
|---------|--|
| R | Rotor, recovery % |
| RANS | Reynolds-Averaged Navier-Stokes |
| RLE | Rotor leading edge |
| RMS | Root mean square |
| R-S | Rotor-stator |
| RSM-SSG | Speziale, Sarkar, and Gatski Reynolds stress model |
| RTE | Rotor trailing edge |
| S | Stator, small axial gap |
| SLE | Stator leading edge |
| SS | Suction surface |
| SST | Shear stress transport |
| SST-CC | Curvature corrected SST turbulence model |
| STE | Stator trailing edge |
| TKE | Turbulent kinetic energy (m^2/s^2) |
| ts | Time step |
| TT | Time transformation |
| URANS | Unsteady Reynolds-Averaged Navier-Stokes |

List of Symbols

Latin symbols

| | |
|-----------------|---|
| A | Area (m ²) |
| a_{ij} | Anisotropy tensor (-) |
| $B(\xi)$ | Streamwise blockage (-) |
| $B(\xi, \zeta)$ | Circumferential blockage at a given streamwise position (-) |
| b_2 | Impeller exit passage height (m) |
| C | Absolute velocity magnitude (m/s) |
| c_p | Specific heat capacity at constant pressure (kJ/kg K) |
| C_r | Radial velocity component (m/s) |
| C_R | Rotor chord (m) |
| C_{RX} | Rotor axial chord (m) |
| C_S | Stator chord (m) |
| C_{SX} | Stator axial chord (m) |
| C_x | Axial velocity component (m/s) |
| C_θ | Circumferential velocity component (m/s) |
| D | Diameter (m) |
| D_w | Relative wake depth , $\frac{U - U_{min}}{U}$ (-) |
| F | Force (N) |

| | |
|-----------------|--|
| f_{r1} | Production multiplier term (-) |
| h | Specific enthalpy (J/kg) |
| h_{is} | Specific isentropic enthalpy at location i (kJ/kg) |
| h_{oi} | Specific stagnation enthalpy at location i (kJ/kg) |
| k | Turbulent kinetic energy (m^2/s^2) |
| L_W | Wake length (m) |
| \dot{m} | Mass flow rate (kg/s) |
| \dot{m}_{c1} | Inlet corrected mass flow rate (kg/s) |
| \dot{m}_{ref} | Reference mass flow rate (kg/s) |
| P | Static pressure (Pa) |
| P_{ij} | Production of Reynolds stress tensor (kg/ms^3) |
| P_k | Production of TKE (kg/ms^3) |
| Pr | Prandtl number (-) |
| P_T | Total pressure (Pa) |
| q | Heat flux (W/m^2) |
| Q | Dynamic head (Pa) |
| r | Radius (m) |
| r^* | Ratio of the strain rate and rotation rate tensor magnitudes (-) |
| \tilde{r} | Argument in the determination of the production multiplier (-) |

| | |
|-----------|--|
| R_c | Radius of curvature (m) |
| Re | Reynolds number (-) |
| Ro | Rossby number (-) |
| s | Blade-to-blade spacing (m) |
| S | Strain rate magnitude (s^{-1}) |
| S_{ij} | Strain rate tensor (s^{-1}) |
| t | Time (s) |
| T | Temperature (K) |
| T_{RBP} | Rotor blade pass period (s) |
| u | Velocity (m/s) |
| U | Blade speed, freestream velocity (m/s) |
| U_2 | Blade tip speed (at impeller exit) (m/s) |
| u_i | Fluctuating velocity component in the i th direction (m/s) |
| U_i | Mean velocity component in the i th direction (m/s) |
| u_m | Main flow velocity (m/s) |
| U_{min} | Minimum wake velocity (m/s) or mass flux (kg/m^2s) |
| U_R | Blade speed (m/s) |
| U_t | Blade tip speed (m/s) |
| W | Relative velocity magnitude (m/s) |

| | |
|-------|--|
| x | Axial location (m) |
| y | Minimum distance to a no-slip wall (m) |
| y^+ | Non-dimensional minimum distance to a no-slip wall (-) |

Greek symbols

| | |
|----------------------|--|
| α | Absolute flow angle (deg) |
| β | Relative flow angle (deg) |
| β_e | Main flow angle with the streamwise direction at the edge of the defect region (deg) |
| β_{vm} | Mean main flow angle with the streamwise direction at the mid-span (deg) |
| β_x | Flow angle with respect to the axial direction (deg) |
| β_ξ | Flow angle with respect to the streamwise direction (deg) |
| δ | Boundary layer thickness (m) |
| δ^* | Displacement thickness (m) |
| δ^{**} | Momentum displacement thickness (m) |
| δ_{ij} | Kronecker delta (-) |
| ΔS | Entropy difference (J/kg K) |
| $\Delta\theta_{P_R}$ | Rotor blade pitch angle (deg) |
| $\Delta\theta_{P_S}$ | Stator blade pitch angle (deg) |
| ε | Turbulence dissipation rate (m^2/s^3) |

| | |
|---------------------|---|
| ε_{ijk} | Permutation tensor (-) |
| ζ | Spanwise coordinate (-) |
| η | Efficiency (%) |
| η_{is} | Isentropic total-to-total efficiency (-) |
| η_{ts} | Total-to-static efficiency (-) |
| η_{tt} | Total-to-total efficiency (-) |
| θ | Circumferential (pitchwise) coordinate (-) |
| κ | Thermal conductivity (W/mK) |
| λ | Rotor-stator axial gap (m) |
| μ | Molecular dynamic viscosity (kg/ms) |
| μ_t | Eddy viscosity (kg/ms) |
| ξ | Streamwise coordinate (-) |
| ρ | Density (kg/m ³) |
| τ | Shear stress (Pa), tip clearance gap (m) |
| τ_{ji} | Shear stress tensor (Pa) |
| ϕ | Any resolved variable |
| Φ_{ij} | Pressure-strain correlation term (kg/ms ³) |
| φ_{vs} | Viscous dissipation (Pa. m/s) |
| ω | Specific dissipation rate (s ⁻¹), total pressure loss coefficient, rotational speed (rad/s) |

| | |
|------------------|--------------------------------------|
| Ω | Rotation rate magnitude (s^{-1}) |
| Ω_{ij} | Rotation rate tensor (s^{-1}) |
| Ω_m^{rot} | Rotation rate of the system (rad/s) |

Subscripts

| | |
|-------------------|--|
| 0 | Location 0 – inlet guide vanes inlet |
| 1 | Location 1 – impeller (rotor) inlet |
| 2 | Location 2 – impeller (rotor) exit / diffuser (stator) inlet |
| 3 | Location 3 – diffuser (stator) exit |
| b | Blockage related quantity |
| <i>Defect</i> | Defect related |
| e | Defect edge value, wake edge |
| ex | Outlet |
| <i>Freestream</i> | Freestream value |
| in | Component inlet plane |
| inv | Inviscid |
| is | Isentropic |
| l | Loss |
| <i>Local</i> | Local value |
| m | Main flow direction |

| | |
|-------------|----------------------------|
| <i>md</i> | Meridional direction |
| <i>min</i> | Minimum |
| <i>out</i> | Component outlet plane |
| <i>pert</i> | Perturbation value |
| <i>r</i> | Radial direction |
| <i>RBP</i> | Rotor blade pass |
| <i>ref</i> | Reference value |
| <i>s</i> | Isentropic property |
| <i>s.d.</i> | Standard deviation |
| <i>t</i> | Blade tip |
| <i>T</i> | Total property |
| <i>TLV</i> | Tip leakage vortex |
| <i>ts</i> | Total-to-static |
| <i>tt</i> | Total-to-total |
| <i>vm</i> | Mean main flow vector mean |
| <i>vs</i> | Viscous |
| <i>W</i> | Wake quantity |
| <i>x</i> | Axial direction |
| ζ | Spanwise direction |

| | |
|----------|----------------------|
| θ | Pitchwise direction |
| ξ | Streamwise direction |

Superscripts

| | |
|---------------------|--------------------------------|
| $\overline{(\)}$ | Reynold mean component |
| $(\)'$ | Reynolds fluctuating component |
| $(\)$ | Favre mean component |
| $(\)''$ | Favre fluctuating component |
| $\overline{(\)}^a$ | Area-weighted average |
| $\overline{(\)}^l$ | Length average |
| $\overline{(\)}^m$ | Mass-weighted average |

Chapter 1

1 Introduction

A gas generator of an aeroengine consists of three components; a compressor, a combustion chamber and a turbine. The compressor is a key component in an aeroengine as it increases the pressure of the air entering the combustion chamber for an efficient combustion process and more output work from the turbines. The high pressure combustion products are then directed to the turbine for the expansion process which produces the work required to drive the propeller (or fan) and compressor. An exhaust nozzle located downstream of the turbine converts the remaining pressure energy leaving the turbine to kinetic energy to produce thrust. Depending on the engine type a fan or a propeller driven by the turbine is placed at the front of the engine. An intake duct is used to direct the flow to the fan or compressors.

Figure 1-1 shows the three most common types of jet engine, turboprop, turbojet and turbofan. It is the turboprop engine which will be considered in the present study. The propeller at the front of the turboprop engine (see Figure 1-1(a)) draws a large mass of air at low speeds. Turboprop engines are most efficient at low and medium speeds (320-720 km/h) and relatively low altitudes (5,500 – 9,000 m), therefore, they are used in small low speed commuter planes [1]. The jet thrust is produced by the propellers and the exhaust gases leaving the nozzle. Turbojet engines, shown in Figure 1-1(b), are developed to operate efficiently at very high speeds and altitudes but they consume more power (more than three times) at takeoff compared with turboprop and turbofan engines [1]. The thrust is achieved by accelerating a relatively small mass of air from the intake to a very high velocity at the exhaust nozzle. These engines are used in military and passenger aircraft. The turbofan engine combines the advantages of turboprop and turbojet engines (see Figure 1-1(c)). The fan acts as the propeller and draws large amounts of air at low air speed which reduces the fuel consumption during takeoff. The turbofan engine operates as a turbojet engine during cruise by controlling the ratio of air bypassing the gas generator to the air flowing in the gas generator [1]. The thrust is developed by both the fan and the exhaust gases leaving the nozzle.

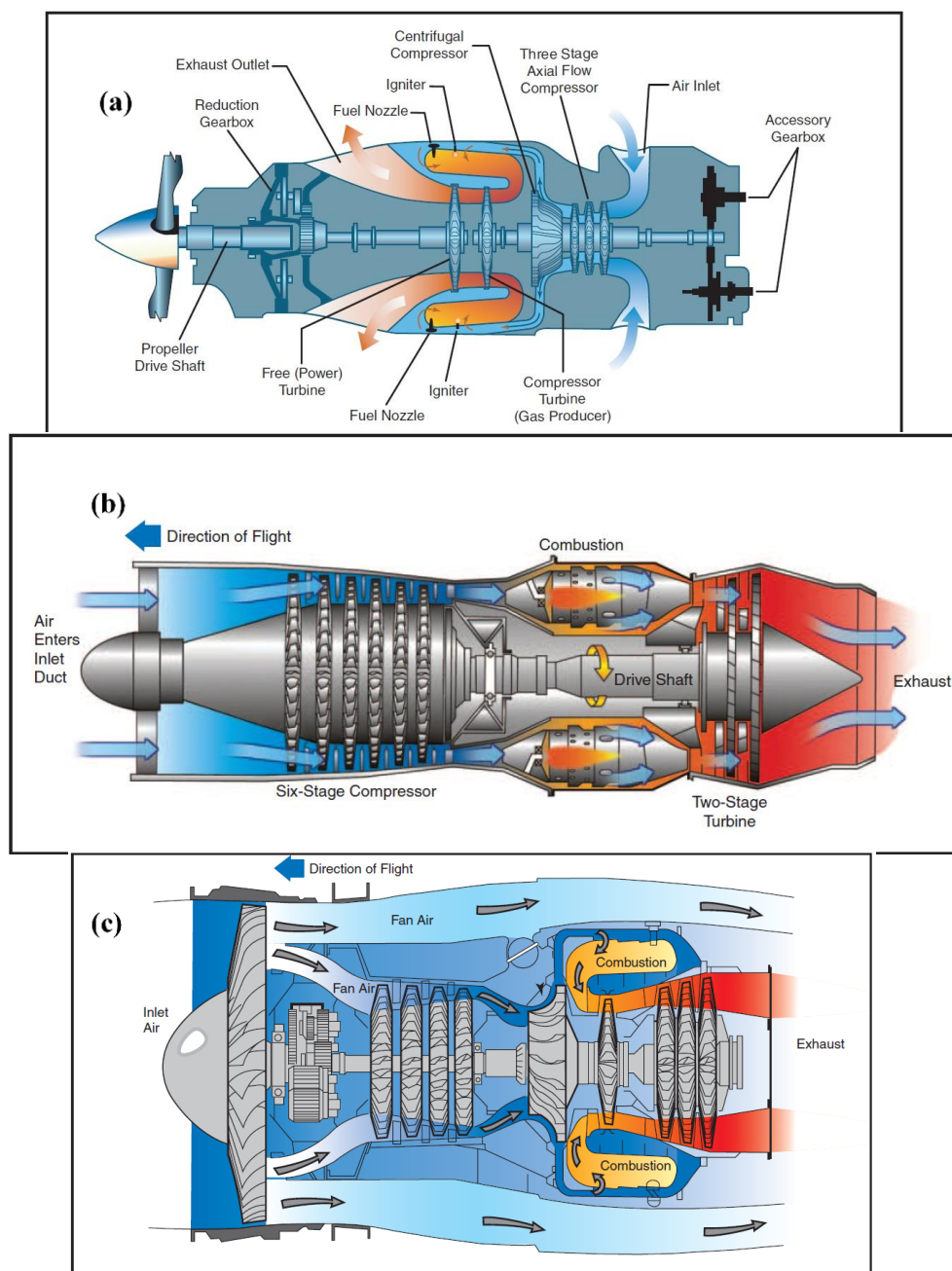


Figure 1-1 Types of aeroengines, (a) turboprop, (b) turbojet and (c) turbofan [1]

The operation of the engine is greatly influenced by the efficiency and the stability of the compressor. Large engines, such as a turbofan, handle large mass flow rates and utilize several axial compressor stages to obtain a pressure rise of 10 - 40 times the pressure at the inlet of the engine. Smaller aeroengines, such as a turboprop, may consist of a centrifugal

stage at the rear of the multistage axial compressor to increase the pressure ratio for the given lower flow rate [2]. Transonic axial compressors have been used in aeroengines to obtain a higher pressure ratio and, hence, reduced size, weight and cost [3]. Any small improvement in the compressor efficiency leads to a substantial saving in fuel costs. Increasing the stable operating range of a multistage compressor is a challenging design task. Therefore, a clear understanding of the flow mechanisms behind losses and instabilities is of a great interest to both researchers and designers.

1.1 Geometry and description of compressors

As mentioned earlier, centrifugal compressors deliver a higher pressure ratio per stage than axial compressors. This is due to the fact that the radius change in the flow path within the centrifugal blade passage increases the specific work. The contribution of centrifugal action does not exist in axial compressors because there is no change in the radius for a given streamline within a blade passage.

1.1.1 Centrifugal compressors

A centrifugal compressor stage is comprised of a rotating component (impeller) and a stationary component (diffuser). The impeller adds energy to the working fluid by drawing it from the inlet and whirling it radially which, in turn, increases the angular momentum [2]. While both static pressure and velocity increase in the impeller, the diffuser only increases the static pressure, by converting the kinetic energy leaving the impeller into pressure energy. In aerospace applications, a centrifugal compressor may have a pressure ratio ranging from 2 to 7 but, on the other hand, they operate at lower efficiencies than axial compressors (75% - 87%) [4]. For details on the definitions of efficiency and pressure ratio, refer to Section 1.1.3. Figure 1-2 shows the geometry of the centrifugal compressor used in this study. The tandem impeller blade consists of two parts, the inducer and exducer. Tandem impellers exhibit a lower efficiency than the conventional single blade impeller (0.5% – 3.8% efficiency reduction depending on the inducer-exducer clocking position). However, tandem impellers improve the impeller exit velocity uniformity which, in turn, improves the diffuser pressure recovery and stable operating range [5]. A fish-tail

diffuser is used since it has been shown to improve the efficiency by 6.8 - 8.8% compared with cambered and flat plate diffusers [6]. This improvement is due to the three-dimensional shape of the diffuser (compared with 2D-based flat plate and cambered diffusers) which accommodates non-uniform flow and thick boundary layers at the impeller exit.

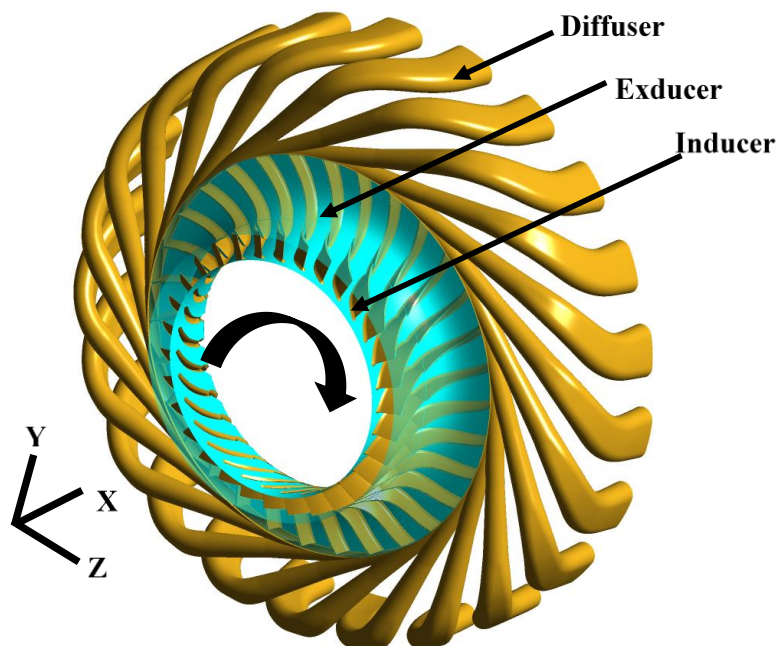


Figure 1-2 Centrifugal compressor stage

1.1.2 Axial transonic compressors

A typical axial compressor stage may consist of a rotating component (rotor) and a stationary component (stator). Inlet guide vanes may be placed upstream of the rotor to adjust the inlet whirl to the rotor of the first stage to accommodate different loading conditions. They act as a nozzle which increases the kinetic energy of the fluid at the expense of the pressure energy [2]. The function of the rotor is similar to the impeller in centrifugal compressors. The stator has two functions: to convert the rotor exit kinetic energy to pressure energy through diffusion and to guide the flow to the next stage rotor in the case of a multistage compressor. Figure 1-3 shows the transonic compressor stage used in this study. A single stage axial compressor delivers a relatively low pressure ratio of the

order of 1.1 – 1.45 [4]. Therefore, in aerospace applications, multiple stages are needed to achieve a pressure ratio of up to 40. For example, if a single axial stage produces a pressure ratio of 1.45, ten stages are needed to provide a pressure rise of 40 ($1.45^{10}=40$). Axial compressors operate at relatively higher efficiency (80% - 91%) [4]. A transonic compressor exhibits higher losses, due to the presence of shockwaves which interact with the blade boundary layer. On the other hand, high Mach numbers allow the compressor to run at a higher mass flow rate which means a more compact design. In addition, transonic compressors run at higher speeds and, hence, higher work and pressure ratio per stage are obtained [2].

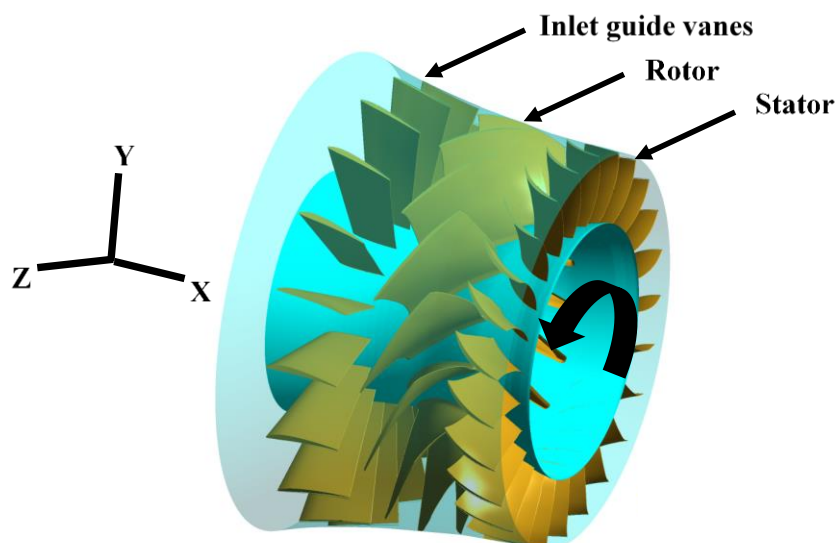


Figure 1-3 Axial compressor stage

1.1.3 Turbomachinery notations and conventions

In this section, the basic definitions of terms and conventions used in the present work are discussed in order for the reader to be familiar with the turbomachinery coordinates and velocity components. The notations are discussed for both of the centrifugal and axial stages in the current study. Since the numerical modelling investigation will be carried out on a reduced model (one or two blade passages only), the notations are shown on a single blade passage for clarity. The functions of each turbo component were discussed previously in Sections 1.1.1 and 1.1.2.

The velocities in turbomachines can be represented in a stationary or a rotating frame of reference. The velocity diagrams at each section are shown for the centrifugal stage in Figure 1-4 and for the axial stage in Figure 1-5(b). The absolute fluid velocity, \vec{C} , can be related to the relative fluid velocity, \vec{W} and the rotor or impeller speed, \vec{U} as follows:

$$\vec{C} = \vec{W} + \vec{U} \quad (1-1)$$

where $\vec{U} = \vec{\omega} \times \vec{r}$ is the local blade speed at a given radius \vec{r} and a rotational speed $\vec{\omega}$.

It is more convenient to use turbo coordinates rather than Cartesian or cylindrical coordinates since they accommodate the curvature of the flow path. The meridional plane is the projection of the flow path on the r - x plane as shown in Figure 1-6(a, b). The projection of the relative velocity magnitude on the meridional plane is the meridional velocity component, W_{md} . The meridional direction is decomposed into two components, the streamwise, ξ , and the spanwise, ζ , directions. The streamwise direction is the tangential vector to a plane located at a certain percentage of the distance between the hub and shroud. The spanwise direction is normal to the streamwise direction and they both share the meridional plane. The hub is the curved surface of the revolution bounded by the inner surface of the flow annulus. The shroud is the surface that defines the component outer diameter. The circumferential direction, θ , is the vector direction tangential to the blade speed direction, \vec{U} , as shown in Figure 1-4 and Figure 1-5. The planes of constant streamwise values, as well as the lines of constant spanwise and circumferential values, are shown for both the centrifugal and axial stages in Figure 1-4 and Figure 1-5(a).

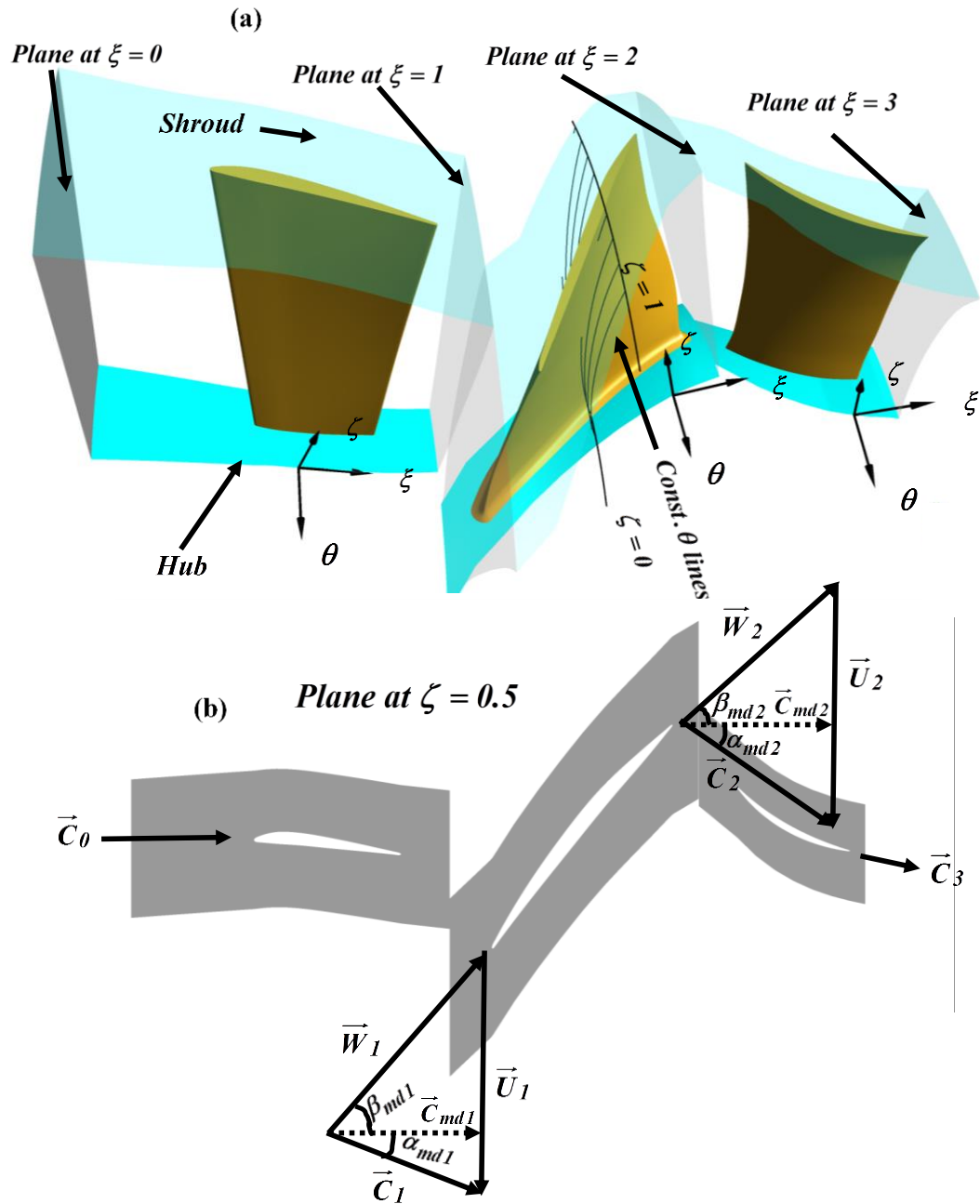


Figure 1-5 Axial compressor stage showing (a) the turbomachinery coordinates and (b) velocity diagrams at a midspan section

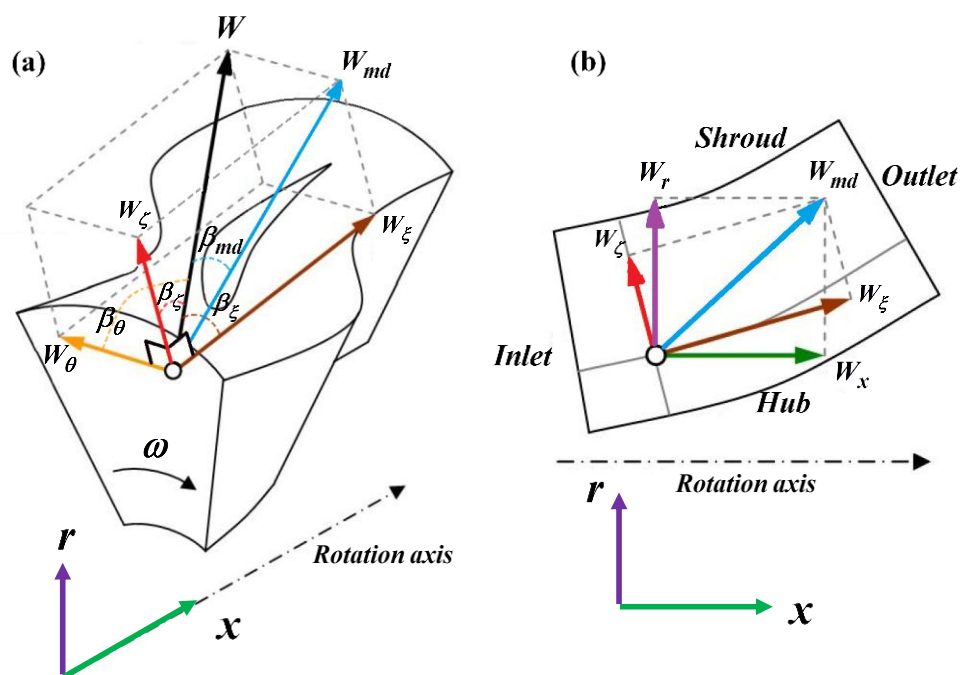


Figure 1-6 Velocity components used in turbomachinery in (a) isometric view and (b) meridional view

The streamwise planes range from 0 at the inlet of the component to 1 at the outlet of the component. The spanwise direction ranges from 0 at the hub to 1 at the shroud. A constant spanwise plane at a mid-distance between the hub and shroud of the axial stage is shown in Figure 1-5(b) where the velocity diagrams are illustrated with respect to the meridional direction. Figure 1-6 shows 3D and 2D views of a blade, illustrating the most important turbomachine velocity components. The streamwise and spanwise velocity components, W_ξ and W_ζ , are the projections of the meridional velocity, W_{md} , on ξ and ζ , respectively. Figure 1-6(b) shows the meridional plane within which the axial, radial, streamwise, spanwise, and meridional components lie. The tangential velocity, W_θ , is the projection of the velocity magnitude, W , on θ . From the velocity diagrams it can be shown that,

$$C_x = W_x \quad (1-2)$$

$$C_r = W_r \quad (1-3)$$

$$C_{md} = W_{md} \quad (1-4)$$

$$C_\xi = W_\xi \quad (1-5)$$

$$C_\zeta = W_\zeta \quad (1-6)$$

$$C_\theta = U + W_\theta \quad (1-7)$$

The velocity flow angles in rotating and stationary frame of references are given by Equations 1-8 and 1-9, respectively as follows:

$$\beta_i = \cos^{-1} \left(\frac{W_i}{W} \right) \quad (1-8)$$

$$\alpha_i = \cos^{-1} \left(\frac{C_i}{C} \right) \quad (1-9)$$

where i stands for any direction, x , r , ξ , ζ , θ , md , etc.

The global performance of compressors is monitored by plotting the pressure ratio, as well as the adiabatic efficiency, against the mass flow rate. The compressor is said to be at choke when it operates at the maximum allowable mass flow rate. Both efficiency and pressure ratio are degraded in this region of operation. The design point should lie within the mass flow rates corresponding to the maximum efficiency region. The stall limit is usually a reduced mass flow point where the pressure ratio reaches a maximum value. The total to static efficiency given by Equation 1-10 is used for the centrifugal stage since the kinetic energy is wasted at the diffuser before entering the combustion chamber. For the axial stage, the total-to-total efficiency given by Equation 1-11 is used since the kinetic energy leaving the stator to the next stage is significant,

$$\eta_{ts} = \frac{h_{3s} - h_{T1}}{h_{T3} - h_{T1}} = \frac{T_{3s} - T_{T1}}{T_{T3} - T_{T1}} \quad (1-10)$$

$$\eta_{tt} = \frac{h_{T3s} - h_{T0}}{h_{T3} - h_{T0}} = \frac{T_{T3s} - T_{T0}}{T_{T3} - T_{T0}} \quad (1-11)$$

where h and T are the enthalpy and temperature, respectively. The subscript, $3s$, in Equation 1-10 stands for the isentropic static condition at the diffuser exit. The subscripts, $T1$ and $T3$, in Equation 1-10 stand for the total condition at the impeller inlet and diffuser exit, respectively. The subscript, $T3s$, in Equation 1-11 stands for the isentropic total condition at the stator exit. The subscripts, $T0$ and $T3$, in Equation 1-11 stand for the total condition at the IGV inlet and stator exit, respectively. The total-to-total pressure ratio, PR, is given by

$$PR = \frac{P_{T,exit}}{P_{T,inlet}} \quad (1-12)$$

where the subscripts $T,inlet$ and $T,exit$ stand for the total pressure at the inlet and exit of the stage, respectively. The total pressure and temperature are mass-weighted average over the plane of interest.

The flow field in a compressor is unsteady, three-dimensional, compressible, viscous and turbulent, therefore, it is resolved using a set of non-linear partial differential equations called the Navier-Stokes equations. Since resolving these equations analytically is not feasible, a Computational Fluid Dynamics (CFD) tool is used to discretize the governing equations of the flow field. A well validated CFD solver is a useful and economic tool to capture more details of the compressor flow field than those captured by experimental investigations. The following section discusses the governing equations used in the present study.

1.2 Governing equations for compressible turbulent flow

The set of equations involves the conservation of continuity (Equation 1-13), momentum (Equation 1-14) and total energy (Equation 1-15). The instantaneous flow field equations are given in their conservation form by

$$\frac{\partial \rho}{\partial t} + \frac{\partial(\rho u_i)}{\partial x_i} = 0 \quad (1-13)$$

$$\frac{\partial(\rho u_i)}{\partial t} + \frac{\partial(\rho u_i u_j)}{\partial x_j} = -\frac{\partial P}{\partial x_i} + \frac{\partial}{\partial x_j} \left[\mu \left(\frac{\partial u_i}{\partial x_j} + \frac{\partial u_j}{\partial x_i} \right) \right] - \frac{2}{3} \frac{\partial}{\partial x_i} \left(\mu \frac{\partial u_k}{\partial x_k} \right) \quad (1-14)$$

$$\frac{\partial(\rho h_o)}{\partial t} + \frac{\partial(\rho h_o u_j)}{\partial x_j} = \frac{\partial P}{\partial t} + \frac{\partial}{\partial x_j} \left(\kappa \frac{\partial T}{\partial x_j} \right) + \frac{\partial}{\partial x_i} (\tau_{ji} u_j) \quad (1-15)$$

where ρ , u_i , P , μ , h_o , T , κ are the density, velocity components, pressure, dynamic viscosity, total enthalpy, temperature and thermal conductivity of the fluid, respectively.

The shear stress tensor, τ_{ji} , is given by

$$\tau_{ji} = \mu \left(\frac{\partial u_i}{\partial x_j} + \frac{\partial u_j}{\partial x_i} \right) - \frac{2}{3} \delta_{ij} \left(\mu \frac{\partial u_k}{\partial x_k} \right) \quad (1-16)$$

In order to resolve the turbulence in the flow, several models may be used. The most accurate method is Direct Numerical Simulation (DNS) which resolves all turbulent scales if the grid size is small enough to capture the Kolmogorov scales. The second most accurate model is Large Eddy Simulation (LES) which uses a filter based on the grid size to resolve turbulent scales which have a size larger than the filter. However, it is unfeasible in turbomachinery practice to use such models because they are computationally expensive. Eddy Viscosity Models (EVM), which are based on the Reynolds-Averaged Navier-Stokes equations (RANS), have been developed over many years to save computational effort. In this section, time averaging of the governing equations, as well as the closure of the RANS

equations, are briefly discussed. For Reynolds time averaging, an instantaneous field variable can be decomposed into mean and fluctuating components as follows:

$$\phi = \bar{\phi} + \phi' \quad (1-17)$$

where ϕ denotes any variable, such as u_i , T , P , etc. The mean and fluctuating components are $\bar{\phi}$ and ϕ' , respectively. Reynolds time averaging is suitable for an incompressible flow. However, for compressible flow, a complexity will be added to the decomposition due to the presence of a correlation between the density and other variables, $\overline{\rho'\phi'}$, as shown in Equation 1-18.

$$\overline{\rho\phi} = \overline{(\rho' + \bar{\rho})(\phi' + \bar{\phi})} = \bar{\rho}\bar{\phi} + \overline{\rho'\phi'} \quad (1-18)$$

In order to simplify the decomposition procedure, Favre averaging, which is a density-weighted averaging, is used as follows:

$$\phi = \tilde{\phi} + \phi'' \quad (1-19)$$

where $\tilde{\phi}$ is the Favre time averaged variable and ϕ'' is the fluctuating component. By multiplying Equation 1-19 by the density and taking the time average, Equation 1-20 reads,

$$\overline{\rho\phi} = \overline{\rho\tilde{\phi}} + \overline{\rho\phi''} = \overline{\rho\tilde{\phi}} \quad (1-20)$$

where the time average of the density-weighted fluctuations is zero. The Favre averaged variable is given by

$$\tilde{\phi} = \frac{\overline{\rho\phi}}{\bar{\rho}} = \frac{1}{\bar{\rho}\Delta t} \int_t^{t+\Delta t} \rho\phi dt \quad (1-21)$$

The Favre averaging is applied to the governing equations. For brevity, the final forms are shown for the continuity, momentum, and energy equations in Equations 1-22, 1-23 and 1-24, respectively.

$$\frac{\partial \bar{\rho}}{\partial t} + \frac{\partial (\bar{\rho} \tilde{u}_i)}{\partial x_i} = 0 \quad (1-22)$$

$$\frac{\partial (\bar{\rho} \tilde{u}_i)}{\partial t} + \frac{\partial (\bar{\rho} \tilde{u}_i \tilde{u}_j)}{\partial x_j} = -\frac{\partial \bar{P}}{\partial x_i} + \frac{\partial}{\partial x_j} \left[\mu \left(\frac{\partial \bar{u}_i}{\partial x_j} + \frac{\partial \bar{u}_j}{\partial x_i} \right) \right] - \frac{2}{3} \frac{\partial}{\partial x_i} \left(\mu \frac{\partial \bar{u}_k}{\partial x_k} \right) - \frac{\overline{\rho u_i'' u_j''}}{\partial x_j} \quad (1-23)$$

$$\begin{aligned} \frac{\partial (\bar{\rho} \tilde{h}_o)}{\partial t} + \frac{\partial (\bar{\rho} \tilde{h}_o \tilde{u}_j)}{\partial x_j} = \\ \frac{\partial \bar{P}}{\partial t} + \frac{\partial}{\partial x_j} \left(\bar{q}_j - \overline{\rho h_o'' u_j''} + \overline{\tau_{ji} u_i''} - 0.5 \overline{\rho u_i'' u_i'' u_j''} + \left[\bar{\tau}_{ij} - \overline{\rho u_i'' u_j''} \right] \tilde{u}_i \right) \end{aligned} \quad (1-24)$$

The number of unknowns is more than the number of equations due to the presence of the fluctuating component correlations in the momentum and energy equations. To solve this closure problem, the Boussinesq approach is used to link the Reynolds stresses to the mean flow gradients by a turbulent viscosity as follows:

$$-\overline{\rho u_i'' u_j''} = \mu_t \left(\frac{\partial \bar{u}_i}{\partial x_j} + \frac{\partial \bar{u}_j}{\partial x_i} \right) - \frac{2}{3} \delta_{ij} \left(\bar{\rho} k + \mu_t \frac{\partial \bar{u}_k}{\partial x_k} \right) \quad (1-25)$$

where $-\overline{\rho u_i'' u_j''}$ is the Reynolds stress tensor, μ_t is the turbulent viscosity (a property of the flow field) and k is the Turbulent Kinetic Energy (TKE) which is given by

$$k = \frac{1}{2} \overline{u_i'' u_i''} \quad (1-26)$$

By inserting Equation 1-25 into Equations 1-23 and 1-24 and applying the same concept for eddy diffusivity for Equation 1-24, the modeled momentum and energy equations are given by

$$\frac{\partial(\bar{\rho}\tilde{u}_i)}{\partial t} + \frac{\partial(\bar{\rho}\tilde{u}_i\tilde{u}_j)}{\partial x_j} = -\frac{\partial\bar{P}}{\partial x_i} + \frac{\partial}{\partial x_j} \left[(\mu + \mu_t) \left(\frac{\partial\bar{u}_i}{\partial x_j} + \frac{\partial\bar{u}_j}{\partial x_i} \right) \right] - \frac{2}{3} \frac{\partial}{\partial x_i} \left(\mu \frac{\partial\bar{u}_k}{\partial x_k} \right) - \frac{2}{3} \bar{\rho}k \quad (1-27)$$

$$\begin{aligned} \frac{\partial(\bar{\rho}\tilde{h}_o)}{\partial t} + \frac{\partial(\bar{\rho}\tilde{h}_o\tilde{u}_j)}{\partial x_j} = \\ \frac{\partial\bar{P}}{\partial t} + \frac{\partial}{\partial x_j} \left(\bar{q}_j - \frac{\mu_t}{Pr_t} \frac{\partial\tilde{h}_o}{\partial x_j} + \left[\bar{\tau}_{ij} - \mu_t \left(\frac{\partial\bar{u}_i}{\partial x_j} + \frac{\partial\bar{u}_j}{\partial x_i} \right) - \frac{2}{3} \delta_{ij} \left(\bar{\rho}k + \mu_t \frac{\partial u_k}{\partial x_k} \right) \right] \tilde{u}_i \right) \end{aligned} \quad (1-28)$$

The equations now have one additional unknown, the eddy viscosity. The purpose of the EVM is to find the value of the eddy viscosity by solving additional transport equation(s) for turbulent quantities. Examples are the TKE and turbulent dissipation rate ($k - \varepsilon$) or the TKE and specific dissipation rate ($k - \omega$). However, the Reynolds Stress Model (RSM) solves the Reynolds stress tensor, $-\overline{\rho u_i'' u_j''}$, without needing to use the Boussinesq approach. For 3D flows, six additional equations are solved. The next section briefly discusses the turbulence models applied in the present study for the centrifugal and axial stages.

1.3 Turbulence modelling with respect to curvature and rotation

The flow in centrifugal compressors involves high curvature and rotation. It has been shown that the convex curvature suppresses turbulence while the concave curvature enhances turbulence [7]. The rotation effect on the turbulence is significant in turbomachines due to the existence of two forces, the Coriolis and centrifugal forces. The Coriolis force plays a major role when the angle between the flow and rotation vector increases, such as in the region near the blade trailing edge of a centrifugal compressor. The rotation forces stabilize the turbulence on the suction surface (SS) because the force acts upward and destabilizes the turbulence on the pressure surface (PS) since the force acts inward [8]. The RSM is superior to the EVMs in terms of predicting the anisotropy of turbulence due to the curvature and rotation effects in turbomachinery [9]. Curvature correction (CC) models have been developed to improve the performance of EVMs [10,

11]. A comparison between the curvature corrected $k-\omega$ shear stress transport model ($k-\omega$ SST-CC), the $k-\omega$ SST without curvature correction, the RSM-SSG and experimental measurements in a highly curved centrifugal compressor stage will be discussed in Chapter 2.

1.4 Blockage in compressors

Flow blockage is the reduction in the effective flow area due to low velocity regions. It is analogous to the boundary layer displacement thickness. Blockage sources in axial compressors may be due to blade, hub and shroud boundary layers, tip and hub clearance flows and blade wakes due to the interaction between the suction and pressure side boundary layers downstream of the blade. All of these sources contribute to the losses in the compressor stage. Since blockage implies a reduction in the effective flow area, it will have a great influence on the choke limit. A small error in the estimation of blockage affects the matching of stages in a multistage compressor [12]. Since the boundary layers of the hub and shroud grow in the streamwise direction, the rear stages have higher blockage than the front stages. The choke mass flow and work done by rotors vary from one stage to another. The flow blockage at each stage needs to be predicted accurately for the design of a multistage compressor [12]. Tip clearance flow is the major contributing source to blockage in a compressor stage [13, 14]. Since the stall limit pressure rise is influenced by the tip flows, the blockage at the tip region can be a measure of blade loading at stall [14].

For a simple 2D compressible flow shown in Figure 1-7, the blockage as a percentage of the geometric area is given by

$$BLK\% = \frac{\delta^*}{A} = \frac{\int_0^{\delta} \left(1 - \frac{\rho(y) \cdot u(y)}{\rho U_{inv}} \right) \cdot dy}{A} * 100\% \quad (1-29)$$

where A is the geometric flow area per unit width and U_{inv} is the inviscid velocity. For 3D flow in a compressor, a main velocity component, $u(y) = u_m(y)$, and a criterion to determine the boundary layer or defect edge, δ , should be selected to represent the

blockage accurately. The main velocity component should be calculated such that any local change in the distribution of the blockage and the inviscid flow does not affect the bulk velocity at a constant mass flow rate [14], i.e.

$$\int_A \rho u_m \cdot dA = \rho U_{bulk} A \quad (1-30)$$

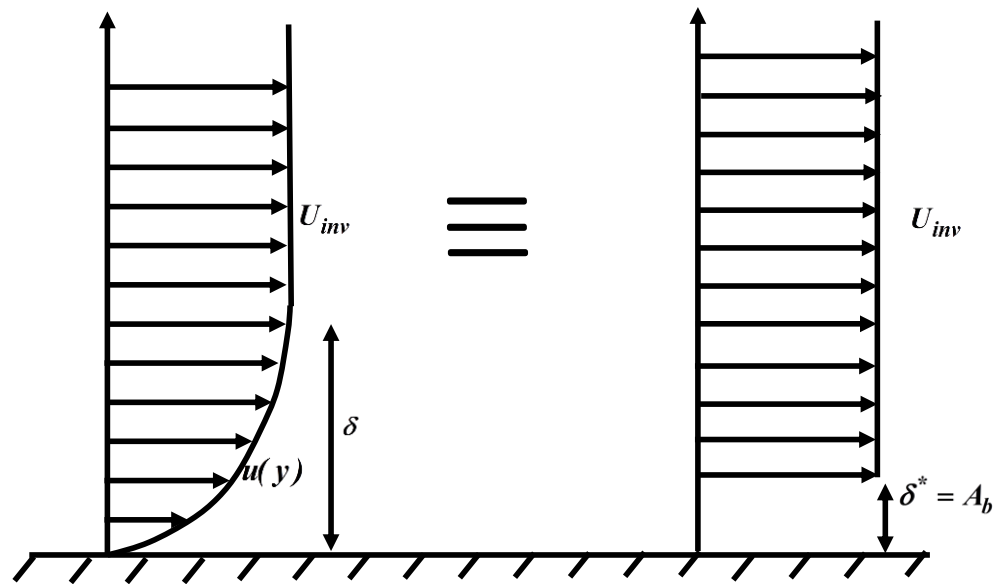


Figure 1-7 Two dimensional velocity profile on a flat plate showing the boundary layer and the displacement thickness

For example, if the rotor tip gap increases and the compressor runs at a constant mass flow rate, the blockage due to the tip flow will increase due to the reduction in the velocity. The core flow will compensate this reduction by an equivalent increase in the core velocity in a way that U_{bulk} remains constant. The velocity component u_m should satisfy this condition. Khalid [14] found that the most accurate component is driven from interpolation of the tangential flow angle at the mid-pitch of the component. In the present study, all the flow velocity components will be considered in order to determine the main flow direction to account for changes of the flow in the spanwise direction. The main flow angles in

streamwise, spanwise, and circumferential directions are obtained by a linear surface fit which excludes high gradient areas as shown in Figure 1-8(a).

To determine the edge that separates the core flow from the defect flow (analogous to the boundary layer thickness), a plane of constant streamwise location is selected first. Second, the gradient in the orthogonal directions (circumferential and spanwise) should be obtained. Third, a cut off value is set to extract the region of high gradients which corresponds to the defect region as shown in Figure 1-8(b). Finally, the inviscid velocity is assumed to be the same as the main flow inside the core region which gives zero blockage. The inviscid velocity inside the defect region is extrapolated from the core region main velocity as shown in Figure 1-8(c).

Chapter 3 presents a more general method to quantify the distribution of blockage along the spanwise and streamwise directions of a transonic axial compressor rotor and stator using both steady and unsteady RANS simulations. The study is carried out at different operating design and off-design conditions to give an insight into the possible mechanisms that trigger stall in the rotor and stator. The normalized blockage and loading parameters from the present work are compared against the previous experimental and numerical work found in refs. [14, 15]. The differences in global performance predictions between steady and unsteady simulations are investigated at the end of the chapter.

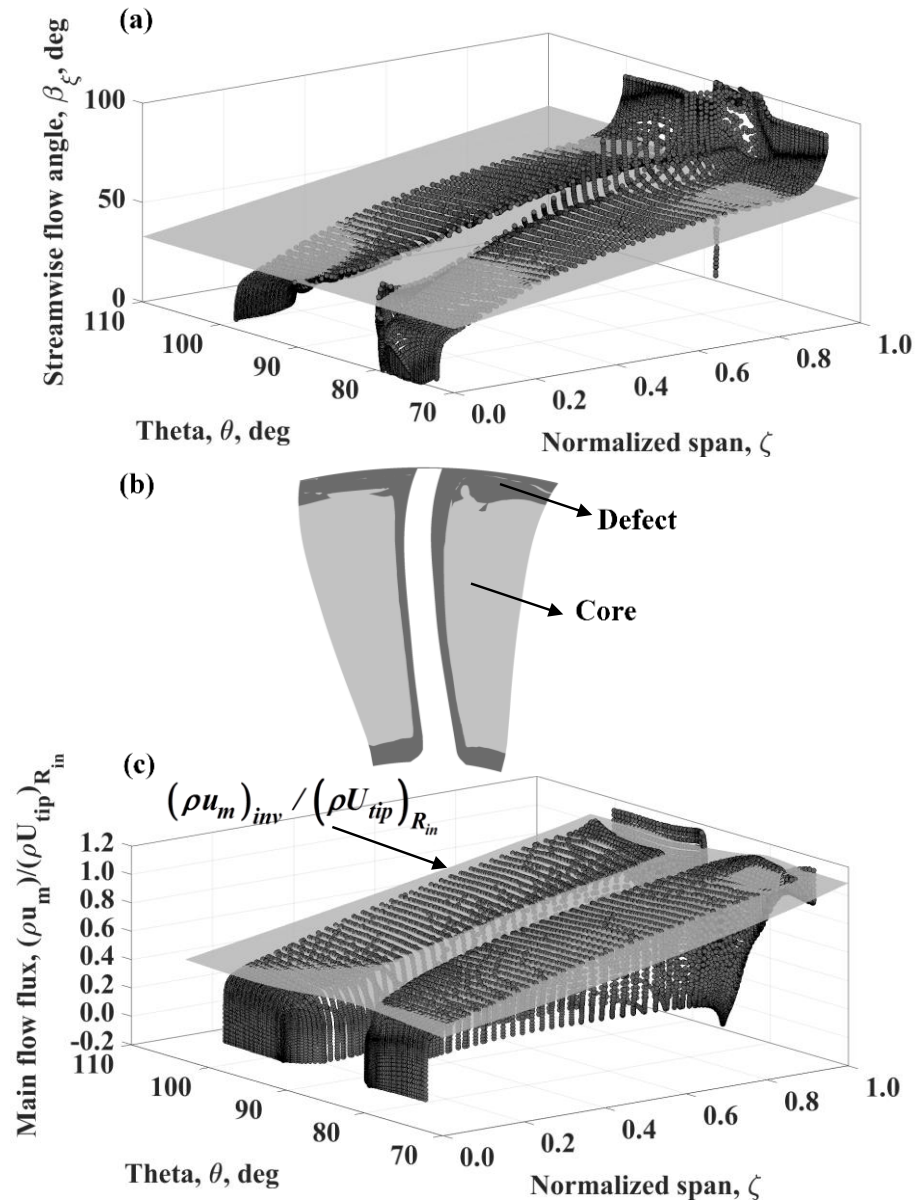


Figure 1-8 Calculation of blockage, (a) main flow mass flux streamwise angle at the rotor mid-chord. The scattered data represent the relative velocity angle and the surface fit represents the main flow velocity angle, (b) a streamwise plane showing defect and core regions and (c) inviscid main flow flux surface fit. The scattered data represent the main flow flux and the surface fit represents the inviscid main flow flux.

1.5 The influence of rotor-stator gap on the aerodynamic performance of a transonic compressor stage

Recent aeroengine design follows a trend towards higher performance and compact configurations. A higher pressure ratio per stage reduces the size and the weight of a multistage compressor. A small improvement in the efficiency saves a huge amount in fuel costs [3]. The flow in a compressor is inherently unsteady, due to the presence of different frames of reference. For example, the rotor wake shown by the axial velocity deficit in Figure 1-9 propagates into the stator passage as the rotor rotates from time t_1 to t_2 which induces unsteadiness in the stator flow field. The gap between the rotor and stator (R-S gap) has been found to have a significant influence on the overall performance of the compressor (efficiency and pressure rise) [13] as well as the local flow field (local losses within the gap and within the downstream stator passage) [16]. In general, the main advantages of reducing the blade row spacing are increasing the overall efficiency and the pressure ratio [13]. This general trend may be attributed to the benefits of the reversible rotor wake stretching occurring in the stator passage [17]. Most of the viscous wake decay due to mixing occurs at the R-S gap which increases blockage and, hence, the mixing losses. On the other hand, too close spacing increases the profile loss due to the stator blade boundary layer, such that the total loss at the stator trailing edge is higher than that for the larger gaps [16]. These factors may explain the contradictory relationship between the overall efficiency trends and the R-S gap [18]. The R-S gap affects the unsteady aerodynamic forces on the blades and, consequently, the lifetime of the blades. It has been found that a smaller axial gap increased the axial and tangential unsteady forces on the stator blade [16, 19]. The levels of noise and vibration are also affected by decreasing the R-S gap [16, 20, 21] but those factors are outside the scope of this study.

Most of the previous R-S gaps studies are based on either 2D numerical and theoretical models [16, 17] or experimental work [13]. Although 3D unsteady numerical simulations are found in the literature [21], more investigation is needed to accurately examine the energy loss due to different sources such as rotor wakes, secondary flows and boundary layers with respect to the R-S gap. A stator-free case is simulated to study the effect of the stator on the rotor wake mixing. In the present work a time efficient and accurate numerical

approach is carried out to investigate the unsteady flow field due to rotor wake-stator interaction [22]. The objective of this part of the research is to examine the mechanisms of rotor wake decay and the associated losses with different R-S gaps using the Time Transformation method (TT) in the CFD software ANSYS CFX 16.0.

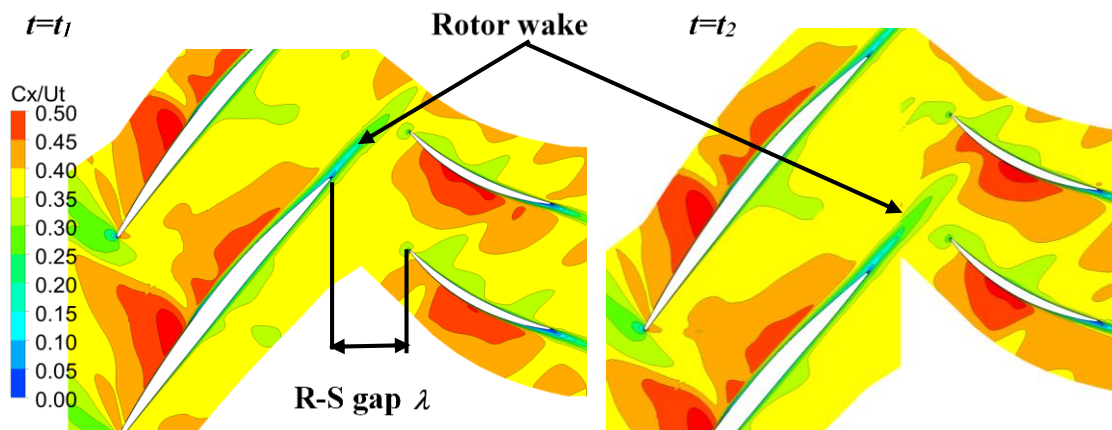


Figure 1-9 Axial velocity contours at a midspan plane showing the rotor wake and the rotor-stator gap

1.6 Objectives

The intent of this work is to investigate the flow field in turboprop engine compressors. Two types of compressors are examined, a high-speed centrifugal stage and a transonic axial stage. A 3D Navier-Stokes solver is used to simulate the air flow in the compressors. In industrial applications, CFD is a tool that aids in the design of turbomachines. However, there are sources of error associated with turbulence modelling and rotating-stationary component interface treatments which may lead to unrealistic solutions. In centrifugal compressors, the effect of rotation and curvature on turbulence is of a great interest. In multistage axial compressors, the flow blockage and component spacing are important design input parameters since they influence the losses and the stability of the compressor. This work has three main objectives as follows:

1. The EVMs are known for their stability and reduced computational cost when compared to RSM. However, the EVMs lack the ability to capture the effects of rotation and curvature. Therefore, curvature correction models have been

developed to include these effects [10, 11]. The SST-CC model has been previously tested in simple geometries [11]. The first objective of the thesis focuses on the assessment of SST-CC for a high-speed, high-curvature centrifugal stage in terms of the sensitivity of turbulence to curvature and rotation. The results are compared with both experimental data and numerical results from the RSM-SSG.

2. Flow blockage has been previously quantified by generating a main velocity component based on a single flow angle [14]. The purpose of this part of the thesis is to quantify and understand the mechanisms of flow blockage in a transonic axial stage using a main flow velocity based on three velocity angles. This method can be applied for both axial and centrifugal stages. This part also investigates the contribution of the rotor tip leakage blockage to the compressor stall. Both steady and unsteady numerical simulation results are compared against previous numerical and experimental studies.
3. The effect of the axial gap between the rotor and stator on the total energy loss remains debatable. The objective of this part of the thesis is to study the influence of the axial gap between the rotor and the downstream stator of the axial stage on both global performance and on the local flow field. The decay of the rotor wake and the losses along the stage are quantified with respect to the variation of the axial gap.

1.7 Thesis organization

The thesis is organized in three articles in which the three topics introduced in this chapter are discussed. Chapter 2 examines the SST-CC model in a highly curved flow in a centrifugal compressor stage. The model is validated against experimental data and compared with previous work conducted using the RSM-SSG. Chapter 3 discusses a method to quantify blockage in a transonic axial compressor stage using both steady and transient simulations. The blockage due to rotor tip flows is plotted against a normalized pressure coefficient and compared with previous studies. Chapter 4 discusses the influence of the axial gap between the rotor and the downstream stator in the same stage used in Chapter 3. Unsteady numerical simulations are carried out using the TT approach for

accurate representation of the propagation of the rotor wake within the stator passage. The rotor wake decay in the stator passage is compared with previous numerical and experimental studies. Chapter 5 provides an overall discussion of all the work presented in this thesis and its implications for engine design, together with a summary of the key findings and recommendations for further research.

1.8 References

- [1] U.S. Department of Transportation, *Airplane Flying Handbook*. Washington, DC, USA, U.S. Department of Transportation, Federal Aviation Administration, Airman Testing Standards Branch, 2004.
- [2] S. L. Dixon and C. A. Hall, *Fluid Mechanics and Thermodynamics of Turbomachinery*, 7th ed. Oxford, UK, Butterworth-Heinemann, 2014.
- [3] R. Biollo and E. Benini, “Recent advances in transonic axial compressor aerodynamics,” *Prog. Aerosp. Sci.*, vol. 56, no. 1, pp. 1–18, 2013.
- [4] M. P. Boyce, *Centrifugal Compressors: A Basic Guide*. Tulsa, Oklahoma, USA, PennWell Corporation, 2003.
- [5] D. A. Roberts and S. C. Kacker, “Numerical investigation of tandem-impeller designs for a gas turbine compressor,” *ASME J. Turbomach.*, vol. 124, no. 1, pp. 36–44, 2002.
- [6] D. P. Kenny, “A novel low-cost diffuser for high-performance centrifugal compressors,” *ASME J. Eng. Power*, vol. 91, no. 1, pp. 37–46, 1969.
- [7] V. Patel and F. Sotiropoulos, “Longitudinal curvature effects in turbulent boundary layers,” *Prog. Aerosp. Sci.*, vol. 33, no. 1–2, pp. 1–70, 1997.
- [8] J. P. Johnston, “Effects of system rotation on turbulence structure: A review relevant to turbomachinery flows,” *Int. J. Rotating Mach.*, vol. 4, no. 2, pp. 97–112, 1998.
- [9] P. Bernard and J. Wallace, *Turbulent Flow: Analysis, Measurement and Prediction*. Hoboken, NJ, USA, John Wiley & Sons Inc., 2002.
- [10] P. R. Spalart and M. Shur, “On the sensitization of turbulence models to rotation and curvature,” *Aerosp. Sci. Technol.*, vol. 1, no. 5, pp. 297–302, 1997.
- [11] P. Smirnov and F. Menter, “Sensitization of the SST turbulence model to rotation

- and curvature by applying the Spalart-Shur correction term,” *ASME J. Turbomach.*, vol. 131, no. 4, pp. 1–8, 2009.
- [12] N. A. Cumpsty, *Compressor Aerodynamics*. Essex, England, Longman Scientific & Technical, 1989.
- [13] L. H. Smith, “Casing boundary layers in multistage axial-flow compressors,” in *Flow Research on Blading*, L. S. Dzung, ed., Elsevier, Amsterdam, The Netherlands, 1970.
- [14] S. Khalid, “The effects of tip clearance on axial compressor pressure rise,” Ph.D. dissertation, Department of Mechanical Engineering, Massachusetts Institute of Technology, USA, 1995.
- [15] S. A. Khalid, A. S. Khalsa, I. A. Waitz, C. S. Tan, E. M. Greitzer, N. A. Cumpsty, J. J. Adamczyk, and F. E. Marble, “Endwall blockage in axial compressors,” *ASME J. Turbomach.*, vol. 121, no. 3, pp. 499–509, 1999.
- [16] W.-S. Yu and B. Lakshminarayana, “Numerical simulation of the effects of rotor-stator spacing and wake / blade count ratio on turbomachinery unsteady flows,” *ASME J. Turbomach.*, vol. 117, no. 4, pp. 639–646, 1995.
- [17] D. E. Van Zante, J. J. Adamczyk, A. J. Strazisar, and T. H. Okiishi, “Wake recovery performance benefit in a high-speed axial compressor,” *ASME J. Turbomach.*, vol. 124, no. 2, pp. 275–284, 2002.
- [18] M. Y. Layachi and A. Bolcs, “Effect of the axial spacing between rotor and stator with regard to the indexing in an axial compressor,” in *Proc. ASME Turbo Expo*, New Orleans, Louisiana, USA, 2001.
- [19] H. E. Gallus, H. Grollius, and J. Lambertz, “The influence of blade number ratio and blade row spacing on axial-flow compressor stator blade dynamic load and stage sound pressure level,” *ASME J. Eng. Power*, vol. 104, no. 3, pp. 633–641, 1982.

- [20] H. Dawson and J. D. Voce, “The effect of axial spacing on compressor tone noise,” in *Proc. 5e Congr Int d’Acoustique*, Liège, Belgium, 1965.
- [21] H. D. Li and L. He, “Toward intra-row gap optimization for one and half stage transonic compressor,” *ASME J. Turbomach.*, vol. 127, no. 3, pp. 589–598, 2005.
- [22] M. B. Giles, “Calculation of unsteady wake/rotor interaction,” *AIAA J. Propuls. Power*, vol. 4, no. 4, pp. 356–362, 1988.

Chapter 2

2 Investigation of the performance of turbulence models with respect to high flow curvature in centrifugal compressors

This chapter investigates three turbulence models with respect to flow with high curvature in a centrifugal compressor stage designed for an aeroengine. The models are compared with experimental data in terms of global performance and local flow field. Section 2.1 presents a survey of turbulence modelling approaches used to capture the rotation and curvature effects. Section 2.2 describes the geometry of the centrifugal compressor stage. Sections 2.3 and 2.4 discuss the governing equations for the implemented models. Section 2.5 presents the results of the simulations and comparisons with experimental work. Finally, Section 2.6 discusses the conclusions of the chapter.

2.1 Introduction

In the present drive to “green” the aircraft industry, one of the current key concerns is to reduce both engine noise and exhaust pollutants, whilst improving overall engine performance. This is being accomplished by developing a better understanding of their internal aerodynamics, leading to higher efficiency and reduced weight; these outcomes being essential to greener engine operation. The main area of focus is on the aerodynamics of regions within the engine where the airflow is strongly turned (high curvature), with specific application to a centrifugal compressor stage. The high curvature regions in a centrifugal compressor impeller can dramatically change the flow field and also have a significant effect on the flow turbulence. In the present work, the compressor stage is analyzed numerically to investigate the performance of state-of-the-art turbulence models that include “curvature correction”. The numerical results are compared to the existing Laser Doppler Velocimetry (LDV) data for the same compressor stage [1]. This research furthers the understanding of the detailed flow field inside centrifugal compressors and also investigates the accuracy of CFD modelling for future turbomachinery components with high curvature.

In industrial applications, CFD is an important tool to aid in the design and validation of turbomachinery components. For these purposes, the simulation of the finest flow structures, such as those obtainable with large eddy simulation (LES) or direct numerical simulation (DNS), is not as critical as a fast turn-around time in the engine design process. Thus, turbulent flow models based on the Reynolds-Averaged Navier-Stokes (RANS) equations are the workhorses of the aerospace industry. Since LES and DNS remain computationally-expensive for high Reynolds number flow, for industrial turbomachinery applications in particular, there is a need to assess and improve the approximate, RANS-based turbulence models that involve no more than the sufficient amount of complexity required to yield the relevant flow physics.

Commonly used turbulence models are based on either (1) the concept of kinematic eddy viscosity as a coefficient of proportionality to relate the Reynolds stress and the mean strain rate tensors [2], namely the eddy viscosity model (EVM) or (2) the differential equation for transport of the Reynolds stress [2], *viz.* the Reynolds stress model (RSM). In the RSM, a separate equation for each of the Reynolds stresses is solved, which enables sophisticated treatment of the anisotropy of turbulence. Thus, the RSM is inherently sensitive to curvature/rotation to some degree. On the other hand, the turbulent viscosity is assumed by the EVM to be locally isotropic, resulting in insensitivity to curvature/rotation effects. In response to this, various researchers have “corrected” different EVMs to account for the effect of system rotation or streamline curvature. For instance, Spalart and Shur [3] corrected the Spalart-Allmaras model by means of a multiplier to the production term in the eddy viscosity equation, York *et al.* [4] modified a constant coefficient (C_μ) to instead be dependent on strain and rotation rates and other researchers have implemented similar corrections to account for curvature effect in the k - ε and k - ω turbulence models [5, 6].

Furthermore, it has been posited that, theoretically, rotation and curvature play the same role [3, 7]. The effect of curvature depends on its magnitude, its directionality (convex or concave), the Reynolds number and the presence of pressure gradients [6, 8]. The most prominent effects, however, are dependent on the directionality of the curvature since convex curvature suppresses or stabilizes the turbulence, as revealed by the decrease in the

turbulence kinetic energy, turbulent mixing and shear stresses, whereas concave curvature enhances (destabilizes) the turbulence [6]. The rotation effect on the turbulence is significant in turbomachines due to the presence of two virtual forces, the Coriolis and centrifugal forces, arising from taking a steady rotating co-ordinate system. The Coriolis force plays a major role when the angle between the flow and rotation vector increases, such as in the region near the blade trailing edge of a radial compressor. The rotation forces stabilize the turbulence on the suction side because the force acts upwards and destabilizes the turbulence on the pressure side since the force acts inwards [9]. For the inducer blade compressor shown in Figure 2-1, the turbulence is stabilized on the suction side due to both convex curvature and rotation effects. On the other hand for the exducer concave suction side near the trailing edge, the curvature and rotation effects act in the opposite way. The aforementioned situation is reversed on the suction side. These effects are examined later in Section 2.5.2.

With respect to a centrifugal compressor, previous investigations [1, 10] of various RANS-based EVMs concluded that the commonly used bulk parameters, such as pressure ratio (PR), temperature ratio (TR) and total-to-static efficiency of a centrifugal compressor stage ($2 < PR < 3$), were more accurately predicted with the shear stress transport (SST) model [11] than the $k-\varepsilon$ model. Furthermore, since the $k-\omega$ and SST models are more suitable than the $k-\varepsilon$ model for wall bounded flows, better for predicting the flow separation and also allowing the integration of the velocity to the wall [12], they are the preferred models for simulating a centrifugal compressor.

The SST turbulence model, which performed better for the simulation of the present compressor than other turbulence models [1], has also been modified with a curvature correction by Smirnov and Menter [13]. This model (denoted SST-CC) applies the modification derived by Spalart and Shur [3] to the k and ω equations in the SST model. This model was evaluated using multiple test cases, from simple geometries to a realistic centrifugal compressor (“Radiver” test case) [13]. For the simplified cases with rotational effects, the SST-CC model was proven to be superior to the SST model in predicting the velocity and shear stress profiles at different Rossby numbers as compared to the

experimental or DNS results. In addition, the results from the SST-CC were comparable with those from more complex RSMs. Conversely, the centrifugal compressor case was not analyzed in much detail, comparing the SST and SST-CC models to the experimental data in terms of overall operating characteristics, but not considering the differences in flow field prediction. Therefore, there is a need for a thorough investigation of the SST-CC model for simulations of compressors to evaluate its practicality for the design of rotating, highly-curved compressors.

2.2 Geometry and compressor stage details

The centrifugal compressor stage analyzed in this work is located downstream of a row of axial compressor stages and just prior to the combustor stage. It consists of a tandem-bladed impeller (exducer and inducer) and a fishtail pipe diffuser as shown in Figure 2-1. There are 31 rotating blades and 22 stationary diffuser pipes in total, generating a pressure ratio of roughly 2.5 between the diffuser exits and inducer entrances. There are multiple sources of curvature worth noting in this case, including the streamline curvature from the axial to radial direction (90°), impeller blades that are curved in two directions, and a highly curved series of diffuser pipes. For the impeller blades, the ratio of the boundary layer thickness to the radius of curvature (δ/R_c) is of the order of 0.02, which is classified as a mild curvature according to a review carried out by Patel and Sotiropoulos [6]. The curvature effect is more prominent than the rotation effect in the inducer and *vice versa* for the exducer. The ratio of the curvature to rotation effects or the ratio of inertial forces to Coriolis forces is quantified by Rossby number ($Ro = W/R_c\Omega_m^{rot}$) where W is the magnitude of the relative velocity, R_c is the radius of curvature, and Ω_m^{rot} is the system rotation rate [14]. For the Radiver compressor, $Ro=0.66$ near the rotor trailing edge [15] while for the present compressor, $Ro=1.2$, which means that the curvature effect is dominant everywhere. The Reynolds number based on the blade speed and exducer passage height is approximately 5×10^5 .

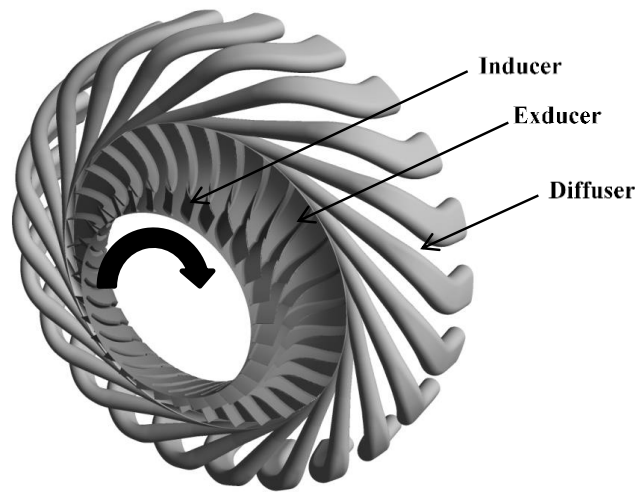


Figure 2-1 Geometry of the compressor stage

2.3 Numerical method

Steady state simulations were performed using the commercial software ANSYS CFX 13 [12], in which a coupled solver and a finite volume method are used. A first-order advection scheme was used for all turbulence quantities and a “high-resolution” advection scheme was used for the momentum and energy equations. The high-resolution scheme is based on the principles of Barth and Jespersen [16] and is of second-order accuracy. Since the compressor is axisymmetric, only one impeller passage and one diffuser pipe, shown in Figure 2-2, were used in the simulations in order to greatly reduce the level of complexity and the required computational time. The figure also illustrates the normalized coordinate system used in this study, which is defined by the streamwise direction, ζ , the spanwise direction, ζ , and the pitchwise direction, θ . A circumferential averaging of the fluxes at the impeller/diffuser interface was carried out using the mixing plane approach, and periodic boundary conditions were used at the impeller blades and the diffuser pipes. In regards to the other boundary conditions, the total pressure and total temperature at the exit of the upstream axial compressor stage were used as the impeller inlet boundary conditions, whilst the static pressure or mass flow rate was used as the outlet boundary condition at the diffuser exit. A static pressure outlet boundary condition was employed in the near-choke operating condition because the mass flow rate does not vary along this region. On the other hand, a mass flow condition was used near compressor stall where the pressure ratio

is relatively constant because the maximum allowable exit static pressure cannot be exceeded.

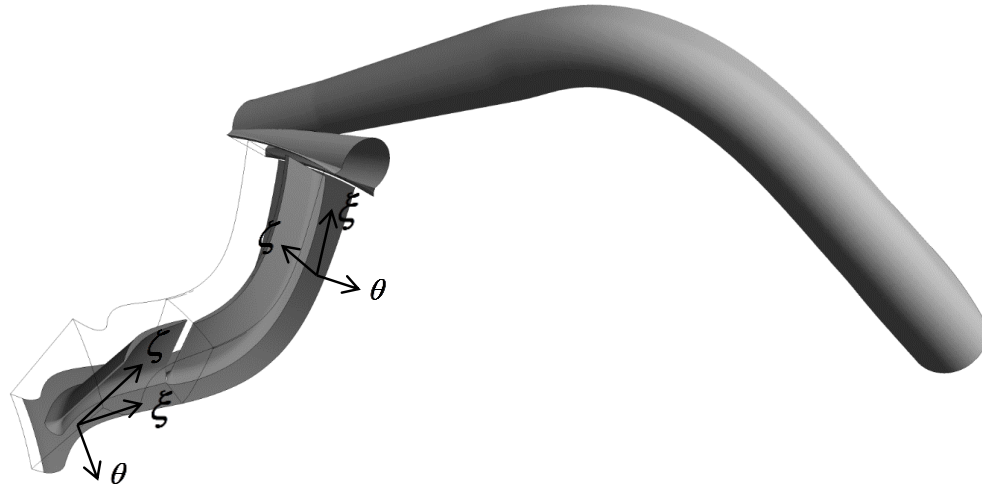


Figure 2-2 Centrifugal compressor computational domain

A hexahedral mesh was used for the impeller passage and a tetrahedral mesh was used for the diffuser passage. The total number of elements was approximately 3.95M, with 1.85M in the impeller and 2.1M in the diffuser pipe. Grid independence for the same computational domain was verified in a previous study [1, 17] using the SST model, and then it was applied for all turbulence models. The same mesh is applied in the present study for the SST-CC model.

A denser prism layer mesh was applied at all wall surfaces, with y^+ values close to 1 to ensure good resolution within the viscous sublayer. Because the RSM-SSG (Speziale, Sarkar, and Gatski Reynolds stress model) uses an ε formulation as opposed to an ω formulation in the SST and SST-CC models, scalable wall functions were used on the same mesh [1], which enforces the y^+ to be greater than or equal to 11.225 for meshes with $y^+ < 11.225$. This allows the same mesh to be used for all models [12].

2.4 Turbulence modelling

In order to evaluate the performance of the SST-CC model, the results from the SST-CC model are compared with those from the SST model as well as the RSM-SSG model from

a previous study [1]. The RSM-SSG turbulence model accounts for any influence of curvature and, consequently, the results from RSM-SSG can complement experimental results in analyzing curvature effects. The previous study [1] indicated that the $k-\varepsilon$ model performs poorly in this case and, thus, will be excluded from the comparison.

The SST model is a combination of the $k-\varepsilon$ and $k-\omega$ models. It uses the $k-\varepsilon$ formulation in the freestream and the $k-\omega$ formulation in the near wall region, in combination with blending functions to seamlessly connect the two models. The transport equations for the SST model [11] are given as follows:

$$\frac{\partial(\rho k)}{\partial t} + \frac{\partial}{\partial x_j}(\rho U_j k) = \frac{\partial}{\partial x_j} \left(\left(\mu + \frac{\mu_t}{\sigma_{k3}} \right) \frac{\partial k}{\partial x_j} \right) + P_k - \beta' \rho k \omega \quad (2-1)$$

$$\begin{aligned} \frac{\partial(\rho \omega)}{\partial t} + \frac{\partial}{\partial x_j}(\rho U_j \omega) &= \frac{\partial}{\partial x_j} \left(\left(\mu + \frac{\mu_t}{\sigma_{\omega 3}} \right) \frac{\partial \omega}{\partial x_j} \right) + (1 - F_1) 2\rho \frac{1}{\sigma_{\omega 2} \omega} \frac{\partial k}{\partial x_j} \frac{\partial \omega}{\partial x_j} \\ &+ \alpha_3 \frac{\omega}{k} P_k - \beta_3 \rho \omega^2 \end{aligned} \quad (2-2)$$

$$P_k = -\rho u_i u_j \frac{\partial U_i}{\partial x_j} = \mu_t \left(\frac{\partial U_i}{\partial x_j} + \frac{\partial U_j}{\partial x_i} \right) \frac{\partial U_i}{\partial x_j} - \frac{2}{3} \frac{\partial U_k}{\partial x_k} \left(3\mu_t \frac{\partial U_k}{\partial x_k} + \rho k \right) \quad (2-3)$$

The coefficients σ_{k3} , $\sigma_{\omega 3}$, α_3 , β_3 are obtained using a blending function F_1 as follows:

$$\phi_3 = F_1 \phi_1 + (1 - F_1) \phi_2 \quad (2-4)$$

$$F_1 = \tanh \left(\min \left[\max \left(\frac{\sqrt{k}}{\beta' \omega y}, \frac{500\mu}{\rho \omega y^2} \right), \frac{4\rho k}{\max \left(2\rho \frac{1}{\sigma_{\omega 2} \omega} \frac{\partial k}{\partial x_j} \frac{\partial \omega}{\partial x_j}, 10^{-10} \right) \sigma_{\omega 2} y^2} \right]^4 \right) \quad (2-5)$$

where y is the minimum distance to a non-slip wall.

The modified SST eddy viscosity is calculated by

$$\mu_t = \frac{\rho a_1 k}{\max(a_1 \omega, S F_2)} \quad (2-6)$$

where F_2 is a second blending function given by

$$F_2 = \tanh \left(\max \left(2 \frac{\sqrt{k}}{\beta' \omega y}, \frac{500 \mu}{\rho \omega y^2} \right)^2 \right) \quad (2-7)$$

The constants and details relating to Equations 2-1 – 2-7 can be found in Table 2-1 [11].

The SST-CC model uses the same transport equations as the SST model, although there is a multiplier in the production term, f_{r1} , making the new production term $f_{r1} P_k$ in Equation 2-1 and $\alpha_3 \omega / k (f_{r1} P_k)$ in Equation 2-2. The formulation for the multiplier [13] is given as follows:

$$f_{r1} = \max \{ \min (f_{rotation}, 1.25), 0.0 \} \quad (2-8)$$

where:

$$f_{rotation} = (1 + c_{r1}) \frac{2r^*}{1 + r^*} [1 - c_{r3} \tan^{-1}(c_{r2} \tilde{r})] - c_{r1} \quad (2-9)$$

$$r^* = \frac{S}{\Omega} \quad (2-10)$$

$$\tilde{r} = 2\Omega_{ik} S_{jk} \left[\frac{DS_{ij}}{Dt} + (\epsilon_{imn} S_{jn} + \epsilon_{jmn} S_{in}) \Omega_m^{rot} \right] \frac{1}{\Omega D^3} \quad (2-11)$$

$$S^2 = 2S_{ij} S_{ij} \quad (2-12)$$

$$\Omega^2 = 2\Omega_{ij} \Omega_{ij} \quad (2-13)$$

$$S_{ij} = \frac{1}{2} \left(\frac{\partial U_i}{\partial x_j} + \frac{\partial U_j}{\partial x_i} \right) \quad (2-14)$$

$$\Omega_{ij} = \frac{1}{2} \left(\frac{\partial U_i}{\partial x_j} - \frac{\partial U_j}{\partial x_i} \right) + 2\epsilon_{mji} \Omega_m^{rot} \quad (2-15)$$

$$D^2 = \max(S^2, 0.09\omega^2) \quad (2-16)$$

The constants c_{r1} , c_{r2} and c_{r3} are equal to 1.0, 2.0 and 1.0, respectively [13]. Note that in Equation 2-8, there is a limiter of 1.25 on the value of f_{r1} . This limiter was put in place to avoid excessive production generation and to ensure numerical stability, and it was based on a number of test cases [13].

The RSM-SSG model solves transport equations for the six individual Reynolds stresses and the turbulence dissipation rate, given by the following equations,

$$\frac{\partial \overline{u_i u_j}}{\partial t} + \frac{\partial}{\partial x_k} (U_k \rho \overline{u_i u_j}) - \frac{\partial}{\partial x_k} \left(\left(\mu + \frac{2}{3} C_s \rho \frac{k^2}{\epsilon} \right) \frac{\partial \overline{u_i u_j}}{\partial x_k} \right) = P_{ij} + \Phi_{ij} - \frac{2}{3} \delta_{ij} \rho \epsilon \quad (2-17)$$

$$\frac{\partial (\rho \epsilon)}{\partial t} + \frac{\partial}{\partial x_j} (\rho U_j \epsilon) = \frac{\partial}{\partial x_j} \left(\left(\mu + \frac{\mu_t}{\sigma_\epsilon} \right) \frac{\partial \epsilon}{\partial x_j} \right) + \frac{\epsilon}{k} (C_{\epsilon 1} P_k - C_{\epsilon 2} \rho \epsilon) \quad (2-18)$$

where P_{ij} is the production term and Φ_{ij} is the pressure-strain correlation term, given by the following equations [18]:

$$P_{ij} = -\overline{\rho u_i u_j} \frac{\partial U_j}{\partial x_k} - \overline{\rho u_j u_k} \frac{\partial U_i}{\partial x_k} \quad (2-19)$$

$$\Phi_{ij} = \Phi_{ij,1} + \Phi_{ij,2} \quad (2-20)$$

$$\Phi_{ij,1} = -\rho\epsilon \left[C_{s1}a_{ij} + C_{s2} \left(a_{ik}a_{kj} - \frac{1}{3}a_{mn}a_{mn}\delta_{ij} \right) \right] \quad (2-21)$$

$$\begin{aligned} \Phi_{ij,2} = & -C_{r1}Pa_{ij} + C_{r2}\rho k S_{ij} - C_{r3}\rho k S_{ij} \sqrt{a_{mn}a_{mn}} \\ & + C_{r4} \left(a_{ik}S_{jk} + a_{jk}S_{ik} - \frac{2}{3}a_{kl}S_{kl}\delta_{ij} \right) \\ & + C_{r5}\rho k (a_{ik}\Omega_{jk} + a_{jk}\Omega_{ik}) \end{aligned} \quad (2-22)$$

where,

$$a_{ij} = \frac{\overline{u_i u_j}}{k} - \frac{2}{3}\delta_{ij} \quad (2-23)$$

The constants for Equations 2-17 - 2-22 can be found in Table 2-1 [18].

Table 2-1 Closure coefficients for the turbulence models

| | | | | | |
|--------------------------------------|---|---|--|--|--|
| SST and SST-CC models | $C_\mu = 0.09$ $\beta' = 0.09$ | $\alpha_1 = 5 / 9$ $\alpha_2 = 0.44$ $a_1 = \sqrt{0.3}$ | $\beta_1 = 0.075$ $\beta_2 = 0.0828$ $c_{r1} = 1.0$ | $\sigma_{k1} = 2.0$ $\sigma_{k2} = 1.0$ $c_{r2} = 2.0$ | $\sigma_{\omega 1} = 2.0$ $\sigma_{\omega 2} = \frac{125}{107}$ $c_{r3} = 1.0$ |
| RSM- SSG model | $C_\mu = 0.1$ $C_s = 0.22$ $C_{r1} = 0.9$ | $C_{\epsilon 1} = 1.45$ $C_{s1} = 1.7$ $C_{r2} = 0.8$ | $C_{\epsilon 2} = 1.83$ $C_{s2} = -1.05$ $C_{r3} = 0.65$ | $\sigma_\epsilon = 1.36$ $C_{r4} = 0.625$ | $C_{r5} = 0.2$ |

2.5 Results and discussion

Two aspects of the results from the simulations are discussed in this section. First, the numerical simulation results using the SST, SST-CC and RSM-SSG models are compared in terms of the stage characteristic curves of total-to-static PR and total-to-static efficiency, as well as the experimental velocity profiles at the impeller-diffuser interface and velocity contours at the diffuser exit. Secondly, the SST-CC model results are investigated in terms

of the production multiplier, f_{r1} , specifically its magnitude at different streamwise sections in the impeller. The detailed analysis of flow field comparisons is carried out at the design point.

2.5.1 Comparison with experimental data

LDV measurements of the flow in the centrifugal compressor stage were performed by Bourgeois *et al.* [1]. These measurements provided profiles and contours of the velocity at the impeller-diffuser interface and at the diffuser exit, which will be used to compare with the numerical results. Several tests were performed to obtain the characteristic curves for the centrifugal stage, including PR and efficiency at 100% design speed.

The comparison of the pressure characteristic for the compressor stage between different models and the experimental data is shown in Figure 2-3. This figure shows the variation in total-to-static stage PR with corrected inlet mass flow rate, with stall being represented by the far left points and choke being represented by the far right points on the pressure ratio curve. From this plot, it can be seen that there are differences in the predicted performance by the SST, SST-CC and RSM-SSG models.

Each of these models performs better over the other models in different regions along the pressure characteristic. The SST model shows the best agreement with the experimental data towards the stall side, whilst the SST-CC model shows better prediction of the choke point. For near stall condition, both models underpredict the PR, 1.9% by the SST and 3.1% by the SST-CC. At the choke condition, the SST-CC model predicts the choke mass flow rate very well, which is only 0.15% lower than the experimental value. The SST model on the other hand, overpredicts the choke mass flow by 0.47%, but this is still within the experimental uncertainty of 1%. Both models underpredict the PR in the region between stall and choke, especially in the region from approximately $\dot{m}_{c1} / \dot{m}_{c1,ref} = 1.01$ to choke. The maximum errors for the PR occur at the corner point of the pressure characteristic where the PR is underpredicted by both the SST and SST-CC models by 3% and 7%, respectively. The PR predicted by the SST model is very close to the experimental values in the region from $\dot{m}_{c1} / \dot{m}_{c1,ref} = 0.94 - 1.01$. The RSM-SSG results reported by Bourgeois

et al. [1] show a good agreement with the experimental data around the design point, although the mass flow rate at the choke region is greatly overpredicted (2.4%) as compared to the SST and SST-CC models and the experimental data. They could not obtain the results in the region near the stall point due to numerical instability of the RSM-SSG model in this compressor operating range.

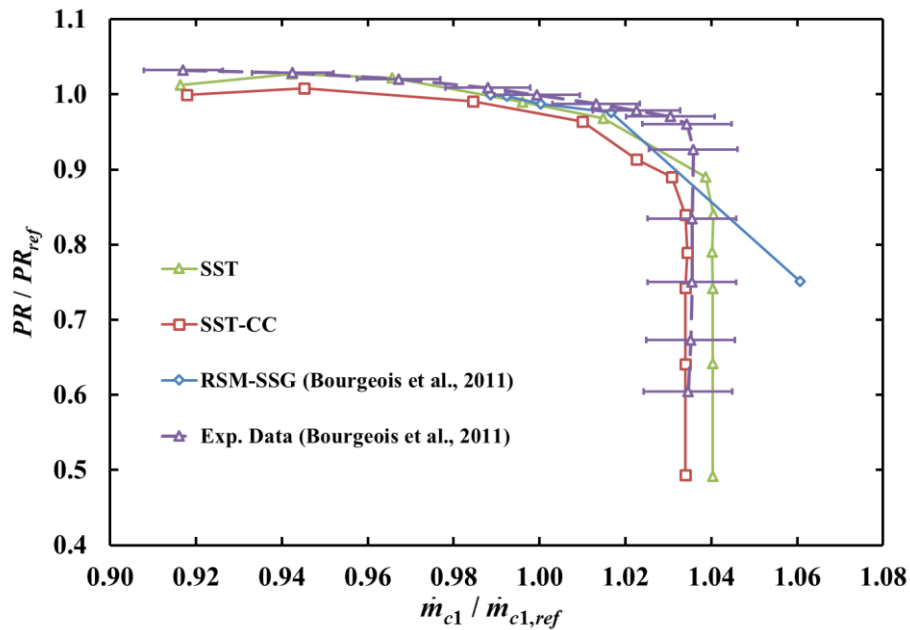


Figure 2-3 Pressure characteristic for the SST, SST-CC, and RSM-SSG models as compared to the experimental data. The bars on the experimental points indicate experimental uncertainty.

The total-to-static efficiency characteristic for the compressor stage are shown in Figure 2-4 for the SST and SST-CC models as well as experimental data and RSM-SSG results extracted from [1]. The efficiency values are calculated using Equation 1-10. The efficiency characteristics show similar trends to the pressure characteristic, although towards the stall side the SST-CC and SST results match the experimental data better than in the pressure ratio case, particularly the SST-CC results. Differences in the efficiency between the experimental data and the SST and SST-CC models at the far stall point are 1.7% and 1.8%, respectively. On the choke side, there is a difference of up to 8% and 9% between experimental results and the SST and SST-CC, respectively, as shown in

Figure 2-4. However at the design point (i.e. where the experimental delta efficiency is zero), the efficiency predicted by the SST is almost identical to that predicted by the experiments. The SST-CC underpredicts the efficiency by about 1.5%.

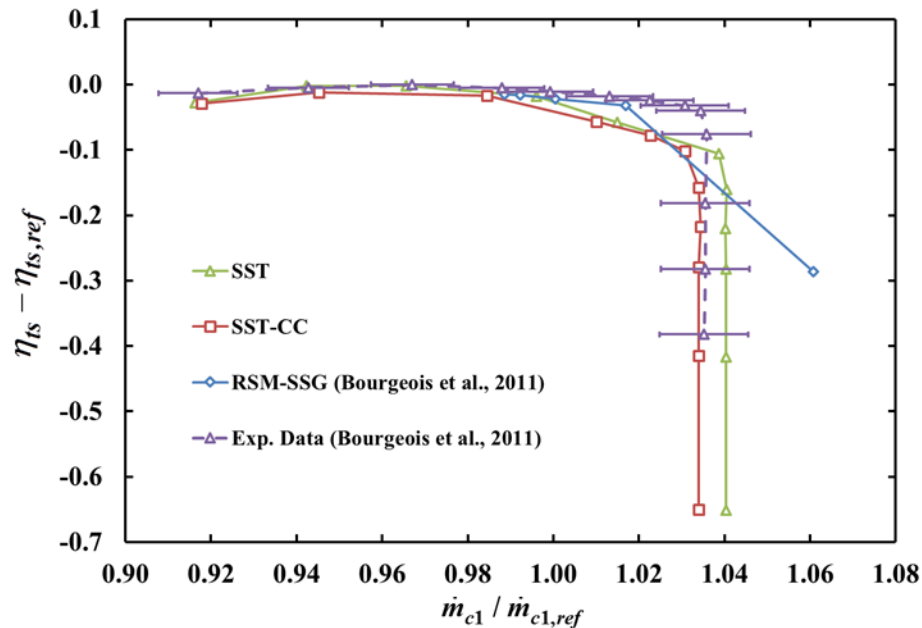


Figure 2-4 Efficiency characteristic for the SST, SST-CC, and RSM-SSG models as compared to the experimental data. The bars on the experimental points indicate experimental uncertainty.

Figure 2-5 and Figure 2-6 show the comparison of the numerical results with the experimental data at the impeller-diffuser interface (the mixing plane) for the circumferential and radial velocities, respectively, normalized by the blade tip speed, U_2 . On the vertical axis, 0 represents the hub and 1 represents the shroud. The uncertainty of the velocity measurements, which is indicated by the error bars, is about 1% of the mean.

At this location, it is clear that the velocity profiles predicted by the SST and SST-CC models are very similar for both the circumferential and radial velocities. The results predicted by both SST and SST-CC show a good agreement to the trend of the experimental results [1], except for the region near the shroud side ($\zeta = 1$), where there are no experimental data available. Both the SST-CC and SST models predict negative radial velocities near the shroud side, whereas the RSM-SSG model [1] predicts a positive

circumferential velocity as shown in Figure 2-6, and both the SST-CC and SST models predict lower circumferential velocities near the shroud side, whereas the RSM-SSG model [1] predicts a higher circumferential velocity as shown in Figure 2-5. Slight differences arise in the radial velocity profiles between the SST and SST-CC models in the near wall region on the shroud side. Table 2-2 lists the root mean square differences (averaged over the profile) between each model and the experimental results for both velocity components. The RSM-SSG model [1] is superior to the other models by around 1.5% for the circumferential velocity and around 2.5% for the radial velocity. Although the RSM-SSG model [1] shows the best overall agreement with the experiments, the other two models predict better trends. The curvature correction in the SST-CC model does not seem to have large effects on the shape of the velocity profile at this location, as compared to the SST model.

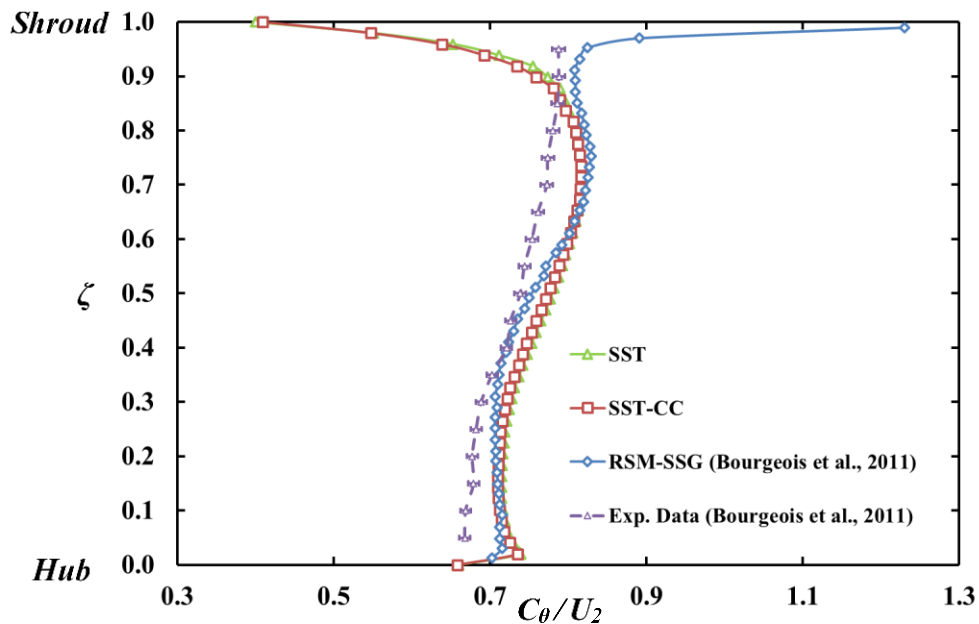


Figure 2-5 Circumferential velocity at the mixing plane, normalized by the blade tip speed. The bars on the experimental points indicate experimental uncertainty.

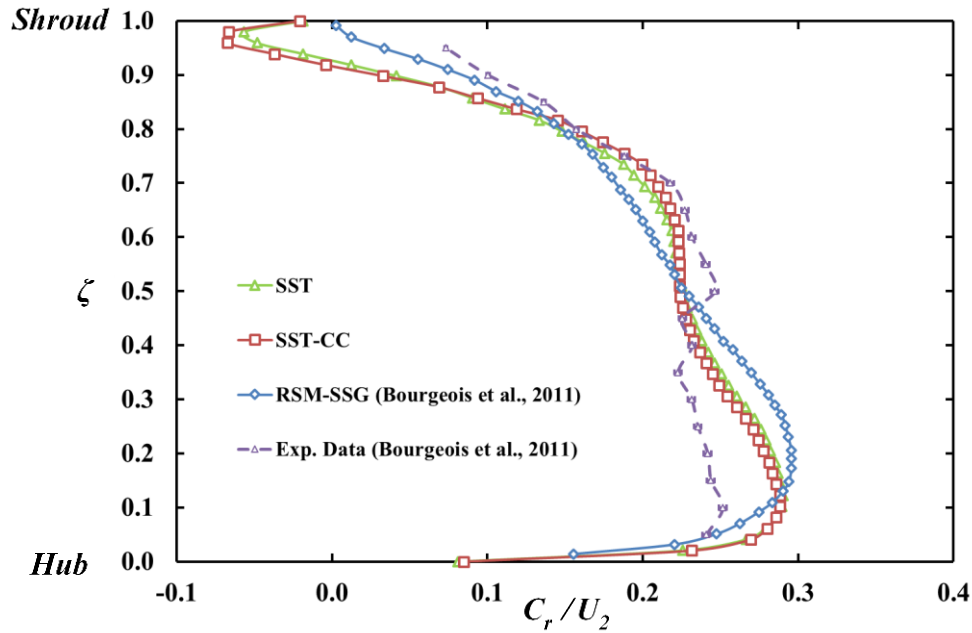


Figure 2-6 Radial velocity at the mixing plane, normalized by the blade tip speed.

The bars on the experimental points indicate experimental uncertainty.

Table 2-2 Differences between the CFD results and experimental data for the tangential and radial velocities at the mixing plane

| | $C_{\theta,SST}$ | $C_{\theta,SST-CC}$ | $C_{\theta,RSM-SSG}$ | $C_{r,SST}$ | $C_{r,SST-CC}$ | $C_{r,RSM-SSG}$ |
|--------------------|------------------|---------------------|----------------------|-------------|----------------|-----------------|
| RMS error | 0.04623 | 0.04608 | 0.03421 | 0.03846 | 0.04051 | 0.03337 |
| RMS error%* | 5.9 | 5.8 | 4.3 | 15.3 | 16.1 | 13.3 |

*The RMS error% is normalized by the maximum value in the experimental velocity profile

Figure 2-7 and Figure 2-8 show the comparison of the contours at the diffuser exit for the axial and circumferential velocities, respectively, from the SST, SST-CC and RSM-SSG models [1], as well as the experimental data. Upstream of its exit, the diffuser pipe has a

bend such that it is concave at the left and lower sides of its cross-section. Overall, the axial velocities predicted by all models agree well with the experimental data. On the left hand side of the diffuser, the SST model predicts a large region of close to zero axial velocity, whereas the SST-CC model does not predict such a large zero velocity region, which is more consistent with the experiments and RSM-SSG [1] results. Towards the centre of the diffuser, the RSM-SSG [1] and SST-CC models underestimate the axial velocity by around 17% of the maximum value. The SST and SST-CC models underpredict the peak velocity in the high-speed region on the right hand side of the diffuser by 10% of the maximum value. On the other hand, the RSM-SSG model [1] overestimates the axial velocity by 10-25% of the maximum value. Overall, all the models perform well in predicting the general shape of the axial velocity field, despite each having different local deficiencies.

The circumferential velocity contours show similar trends to the axial velocity contours in that the SST and SST-CC models each have regions where they perform better than the other. In the high velocity region on the right hand side, the SST model overestimates the high velocity zone by up to 30% of the maximum value, whilst the SST-CC provides a more reasonable circumferential velocity distribution. On the other hand, the low velocity region is better predicted using the SST model, which produces a much smaller negative velocity region, more like the experimental data. Both low and high circumferential velocity regions are overpredicted by the RSM-SSG model [1] by up to 50% of the maximum value. Therefore, it is difficult to conclusively say which of the models is better matched to the experimental data.

2.5.2 Investigation of the production multiplier, f_{r1}

The difference between the SST and SST-CC models occurs in the production term. The SST-CC model includes a production multiplier term, f_{r1} , which either decreases or increases the production depending on the curvature. For example, consider a concave curvature, which enhances the turbulence. This curvature would lead to a multiplier between 1 and 1.25, effectively increasing the magnitude of the production term. On the other hand, a convex curvature suppresses the turbulence, which would result in a multiplier between 0 and 1, in effect decreasing the production term. With this in mind, it

is interesting to look at the effect of this production multiplier in a geometry that is quite complex.

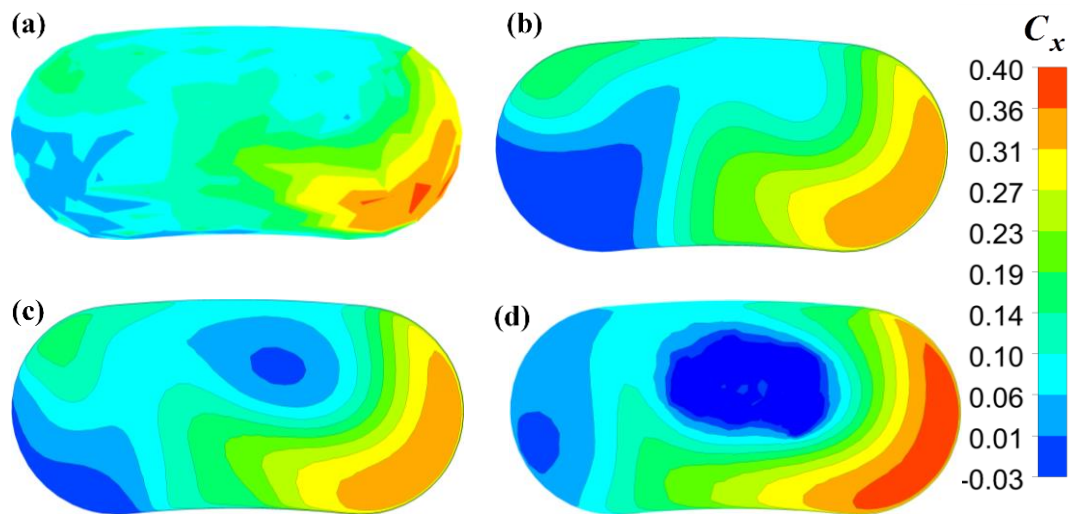


Figure 2-7 Normalized axial velocity contours (C_x) at the diffuser exit; (a) experimental data [1], (b) SST, (c) SST-CC, and (d) RSM-SSG [17]

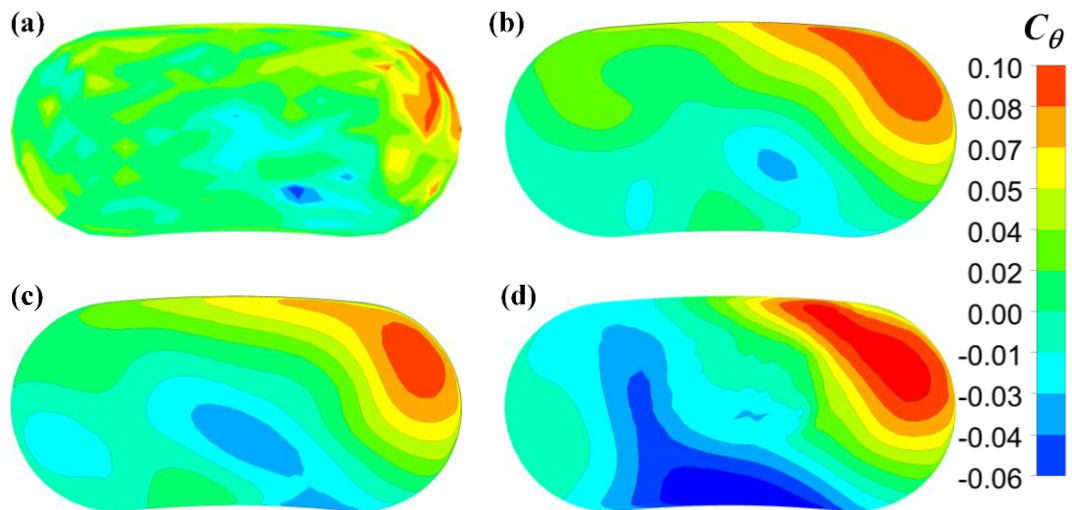


Figure 2-8 Normalized circumferential velocity (C_θ) contours at the diffuser exit; (a) experimental data [1], (b) SST, (c) SST-CC, and (d) RSM-SSG [17]

The contours of f_{rI} are given in Figure 2-9(b-d) at three different streamwise locations shown in Figure 2-9(a), respectively. The locations of $\zeta = 0.21$, 0.65 and 0.96 as shown in Figure 2-9(a) are selected to examine the curvature effects since the radii of curvature are significant at the inducer blade ($\zeta = 0.21$) and the hub and it is maximum at the hub ($\zeta = 0.65$) and shroud ($\zeta = 0.96$). The combined rotation and curvature effects are examined near the exducer trailing edge at ($\zeta = 0.96$). The components of the planes of interest are illustrated in the left column of Figure 2-9(b-d). All the contours show sudden changes in f_{rI} at the core region away from the boundary layer. Careful examination of the values of f_{rI} inside the wall boundary layers shows that f_{rI} is sensitive to the type of the curvature. At ($\zeta = 0.21$), the values of f_{rI} are below 1 near the SS in response to its convexity and above 1 near the concave PS as shown in Figure 2-9(b). The same behaviour is observed in the case of the strong curvature of the hub and shroud at ($\zeta = 0.65$) as shown in Figure 2-9(c). The curvature effects seem to be dominant near the exducer trailing edge at ($\zeta = 0.96$) where the exducer SS is concave and the exducer PS is convex (see Figure 2-9(d)). Turbulence suppression by the convex curvature at the PS overcomes the turbulence enhancement by the rotation effect, thus, the values of f_{rI} are below 1 near the PS boundary layer as shown in Figure 2-9(d). This was noted earlier by the estimated Rossby number, which indicates the dominance of the curvature effect near the exducer trailing edge.

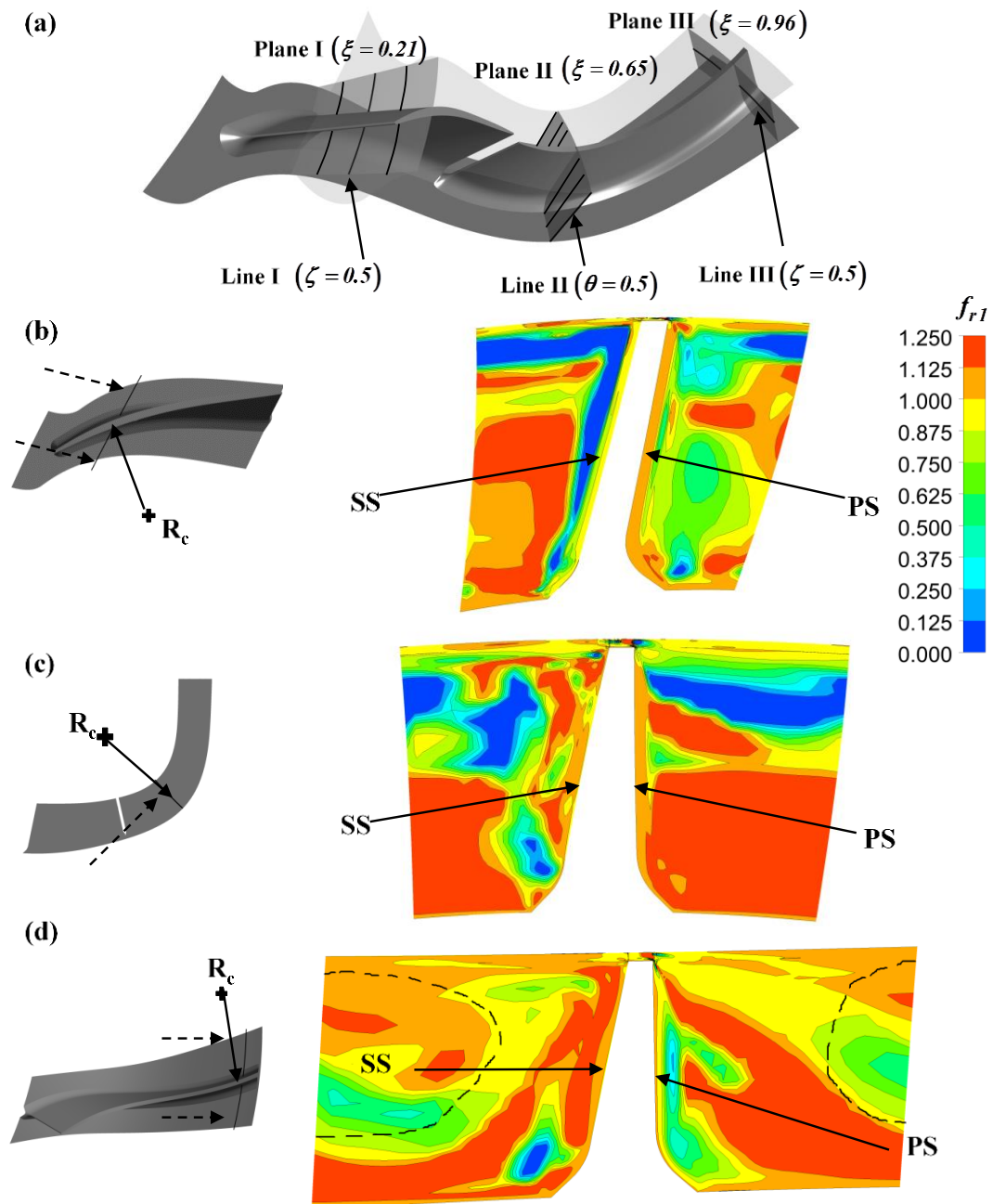


Figure 2-9 Streamwise planes and lines of interest and corresponding f_{r1} contours and radius of curvature component; (a) planes and lines shown on the impeller, (b) curvature of interest and corresponding f_{r1} at $\xi = 0.21$, (c) curvature of interest and corresponding f_{r1} at $\xi = 0.65$, and (d) curvature of interest and corresponding f_{r1} at $\xi = 0.96$

To illustrate the sensitivity of the SST-CC model to the curvature, the profiles of f_{rI} and the corresponding normalized turbulence production predicted by the SST, SST-CC and RSM-SSG models are examined along the three lines shown in Figure 2-9(a) where the curvature effects and the combined rotation/curvature effects are dominant. Since the turbulence production in the RSM-SSG equation is a tensor, the P_k term in the k -equation (Equation 2-1) is used in the calculation of $P_{k,RSM}$, i.e., $P_{k,RSM} = -\overline{\rho u_i u_j} \frac{\partial U_i}{\partial x_j}$. The turbulence

production is normalized by the radius and blade speed at the exducer trailing edge. The left and right ordinates in Figure 2-10 represent the production term and production multiplier respectively. The abrupt changes in f_{rI} are associated with regions of relatively low or near zero turbulence production as shown in Figure 2-10, which indicates that the curvature correction has no effect at these locations. The elevated production values are observed near the walls where f_{rI} varies between 1 and 0.8 near the convex inducer SS and between 1 and 1.1 near the concave inducer PS at $\zeta = 0.21$, $\zeta = 0.5$ as shown in Figure 2-10(a). The same behaviour is observed near the hub and shroud at $\zeta = 0.65$, $\theta = 0.5$ as shown in Figure 2-10(b). The SST-CC model captures the reduction in the turbulence production near the shroud when compared with RSM-SSG results. The f_{rI} parameter gradually goes above 1 near the concave hub and below 1 near the convex shroud. At $\zeta = 0.96$, $\zeta = 0.5$, the exducer SS is concave and the exducer PS is convex (see Figure 2-9(d)). Although the rotation is more significant near the exducer trailing edge, the curvature effect is still dominant as shown by Figure 2-10(c). The turbulence is enhanced by the concave SS instead of the suppression by the rotation effect. The two bumps in the turbulence production curves at $\theta = 0.2 - 0.5$ and $\theta = 0.7 - 0.8$ are due to the strong shear at the interface between the tip leakage vortex and the primary flow as illustrated by the dashed line in Figure 2-9(d). In general, the root mean square of the differences between the results of each the SST models and those of the RSM-SSG model are of the order of 10% of the maximum turbulence production. In terms of the overall trend, the SST-CC model shows a better agreement with the RSM-SSG model away from the walls.

The concave and convex curvatures of the hub and shroud are not the only factors affecting the f_{rI} in this case. According to the formulation of f_{rI} , it is apparent that the magnitude of

f_{r1} is dependent on two variables, r^* and \tilde{r} , given by Equations 2-10 and 2-11 [13]. These quantities are dependent on the strain rate tensor (Equation 2-12), the rotation rate tensor (Equation 2-13), and the rotation rate of the system (Ω_m^{rot}). It is clear from the complexity of the problem at hand, that the curvature is not the only factor affecting the magnitude of f_{r1} . Therefore, the terms r^* and \tilde{r} need to be examined to understand their influence on f_{r1} . Since it is obvious that the regions of significant production are located near the walls, Figure 2-11 shows the contours of r^* and \tilde{r} at $\zeta = 0.21$, $\zeta = 0.65$ and $\zeta = 0.96$. The absolute values of \tilde{r} are far below 0.5 everywhere, which suggests that the rotation effects are negligible, as indicated by Spalart and Shur [3]. It seems that r^* is also sensitive to the rotation as demonstrated by Figure 2-11(a, c), and e, which show that r^* increases away from the PS and decreases away from the SS. It is clear from Equation 2-9 that f_{r1} is proportional to r^* and inversely proportional to \tilde{r} . At $\zeta = 0.21$, the two terms have reversed trends, which enhances the increase and decrease in f_{r1} for the PS and the SS (Figure 2-11(a, b), respectively). This is consistent with the results presented in Figure 2-10(a). At $\zeta = 0.65$, the variation of r^* is significant away from the end walls where the turbulence production is relatively low (Figure 2-11(c)). High values of \tilde{r} are observed near the shroud, which gives smaller f_{r1} values due to the convex curvature (Figure 2-11(d)). At $\zeta = 0.96$, both terms act almost with the same trend, as shown in Figure 2-11(e, f). Comparing with Figure 2-10(c), which shows that the turbulence is suppressed near the convex PS and enhanced near the concave SS, f_{r1} seems to react more to the variation of \tilde{r} rather than r^* , which suggests that \tilde{r} is most likely an indication of the strength of curvature while r^* is an indication of the rotation effects, which are insignificant in the current study.

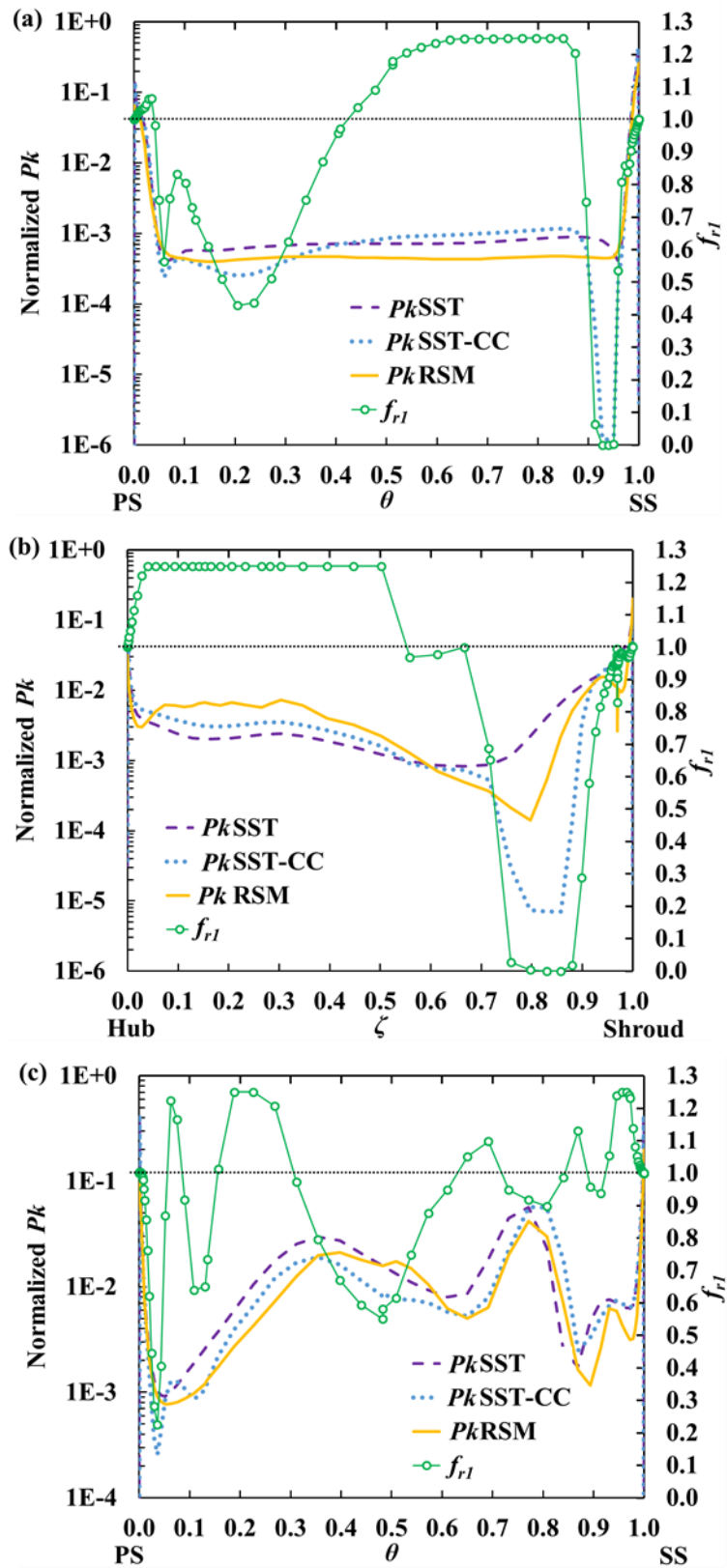


Figure 2-10 Profiles of turbulence production and production multiplier; (a) along the circumferential direction at $\xi = 0.21$ and $\zeta = 0.5$, (b) along the spanwise direction at $\xi = 0.65$, and $\theta = 0.5$ and (c) along circumferential direction at $\xi = 0.96$, and $\theta = 0.5$

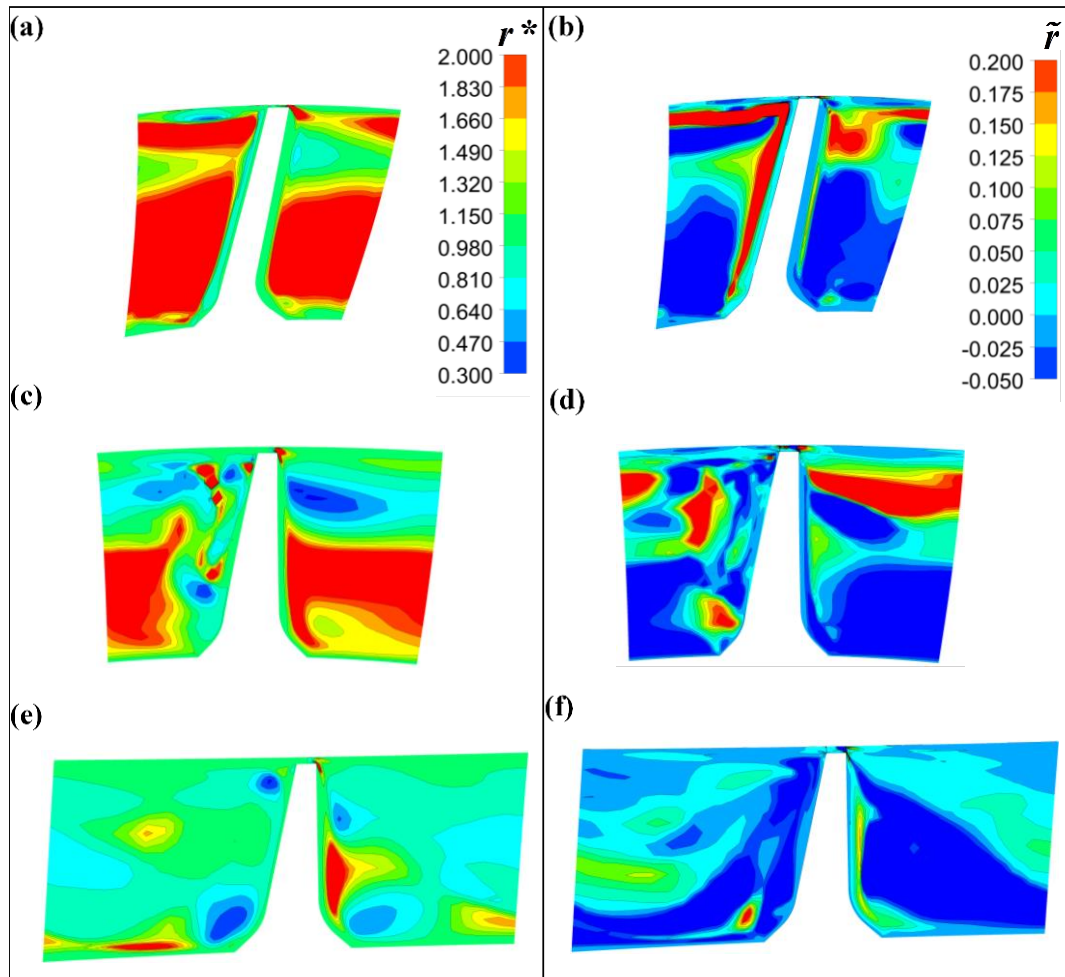


Figure 2-11 Contours of r^* and \tilde{r} at planes; (a, b) $\xi = 0.21$, (c, d) $\xi = 0.65$, and (e, f) $\xi = 0.96$

2.6 Conclusions

A centrifugal stage was simulated using a commercial CFD solver to evaluate the performance of the curvature correction in the SST-CC model. An analysis of the

production multiplier term, f_{r1} , in the SST-CC model was also conducted. From this analysis, the following conclusions can be drawn:

- In terms of the pressure ratio characteristic at 100% design speed, the SST-CC model gives a better prediction compared with the experimental data in the choke region, but the SST model is superior in the stall region.
- Similar trends between the SST-CC and SST models are found in the efficiency characteristic at 100% design speed.
- Minimal differences are found between the SST and SST-CC models in terms of velocity profiles at the mixing plane and some minor differences were found between the models for the velocity contours at the diffuser exit. Both models performed well overall.
- The production multiplier (f_{r1}) shows the desired sensitivity to the curvatures of the blade surfaces of the compressor. The gradual trends in the magnitude of f_{r1} are seen at the regions of high turbulence production, in particular near the walls, while the abnormal behaviour of f_{r1} is observed where production values are insignificant. The sensitivity of the turbulence to the domain rotation is not clear in this case since it is mainly dominated by the curvature effect.

The next chapter describes a method to quantify blockage in compressors which can be applied in both centrifugal and axial stages. This method is investigated in an axial transonic stage using steady and unsteady numerical simulations.

2.7 References

- [1] J. A. Bourgeois, R. J. Martinuzzi, E. Savory, C. Zhang, and D. A. Roberts, “Assessment of turbulence model predictions for an aero-engine centrifugal compressor,” *ASME J. Turbomach.*, vol. 133, no. 1, pp. 1–15, 2011.
- [2] D. C. Wilcox, *Turbulence Modeling for CFD*, 2nd ed. La Cañada, California, USA, DCW Industries, 1998.
- [3] P. R. Spalart and M. Shur, “On the sensitization of turbulence models to rotation and curvature,” *Aerosp. Sci. Technol.*, vol. 1, no. 5, pp. 297–302, 1997.
- [4] W. D. York, D. K. Walters, and J. H. Leylek, “A simple and robust linear eddy-viscosity formulation for curved and rotating flows,” *Int. J. Numer. Methods Heat Fluid Flow*, vol. 19, no. 6, pp. 745–776, 2009.
- [5] B. Lakshminarayana, “Turbulence modeling for complex shear flows,” *AIAA J.*, vol. 24, no. 12, pp. 1900–1917, 1986.
- [6] V. Patel and F. Sotiropoulos, “Longitudinal curvature effects in turbulent boundary layers,” *Prog. Aerosp. Sci.*, vol. 33, no. 1–2, pp. 1–70, 1997.
- [7] D. C. Wilcox and T. L. Chambers, “Streamline curvature effects on turbulent boundary layers,” *AIAA J.*, vol. 15, no. 4, pp. 574–580, 1977.
- [8] J. Piquet, *Turbulent Flows: Models and Physics*. Germany: Springer-Verlag, 1999.
- [9] J. P. Johnston, “Effects of system rotation on turbulence structure: A review relevant to turbomachinery flows,” *Int. J. Rotating Mach.*, vol. 4, no. 2, pp. 97–112, 1998.
- [10] D. A. Roberts and R. Steed, “A comparison of steady state centrifugal stage CFD analysis to experimental rig data,” in *ANSYS User’s Conference, Pittsburgh*, 2004.
- [11] F. R. Menter, “Two-equation eddy-viscosity turbulence models for engineering applications,” *AIAA J.*, vol. 32, no. 8, pp. 1598–1605, 1994.

- [12] Ansys Inc., *Ansys CFX-Solver Theory Guide. ANSYS CFX Release 13.0*. Ansys Inc., Canonsburg, PA, 2010.
- [13] P. Smirnov and F. Menter, “Sensitization of the SST turbulence model to rotation and curvature by applying the Spalart-Shur correction term,” *ASME J. Turbomach.*, vol. 131, no. 4, pp. 1–8, 2009.
- [14] J. Moore, J. G. Moore, and M. W. Johnson, *On Three-Dimensional Flow in Centrifugal Impellers*. London, UK, HM Stationery Office, 1977.
- [15] G. Dufour, J.-B. Cazalbou, X. Carbonneau, and P. Chassaing, “Assessing rotation/curvature corrections to eddy-viscosity models in the calculations of centrifugal-compressor flows,” *J. Fluids Eng.*, vol. 130, no. 9, pp. 1–10, 2008.
- [16] T. J. Barth and D. C. Jespersen, “The design and application of upwind schemes on unstructured meshes,” in *Proc. 27th Aerospace Sciences Meeting*, Reno, Nevada, USA, 1989.
- [17] J. A. Bourgeois, “Numerical mixing plane studies with validation for aero-engine centrifugal compressor design,” MEng thesis, University of Western Ontario, London, Ontario, Canada, 2008.
- [18] C. Speziale, S. Sarkar, and T. Gatski, “Modelling the pressure-strain correlation of turbulence: an invariant dynamical systems approach,” *J. Fluid Mech.*, vol. 227, pp. 245–272, 1991.

Chapter 3

3 Numerical investigation of blockage development in an aeroengine transonic axial compressor stage

This chapter discusses a method to quantify flow blockage in compressors. Steady and unsteady numerical simulations are carried out in a transonic axial stage using the commercial code ANSYS CFX. The variation of the rotor tip blockage with the rotor loading is examined and compared with previous numerical and experimental studies on different compressor stages. The discrepancies between steady and unsteady simulations are discussed. Section 3.1 presents a survey of different methods used in the literature to quantify flow blockage in compressors. Section 3.2 shows the geometry of the compressor stage used as well as the implemented numerical models. Section 3.3 describes the spatial and temporal independence of the numerical model. Section 3.4 illustrates the global performance of the compressor using steady and unsteady simulations. Section 3.5 describes the methodology used to quantify blockage. Section 3.6 gives a comparison between the current blockage predictions and previous experimental and numerical studies. Section 3.7 shows blockage development in the stage at both high-efficiency and near-stall operating points. Finally, the local and global discrepancies between the steady and transient simulations are discussed in Sections 3.8 and 3.9, and the conclusions are given in Section 3.10.

3.1 Introduction

Axial transonic compressors are core components in modern aeroengines due to their high pressure ratio per stage compared to axial subsonic compressors. The operating range of the whole engine is highly dependent upon the performance and stability of the compressor. When the engine runs at reduced mass flow rates or speeds, there is a risk that the compressor will experience stall and surge. Therefore, understanding the stall physics is of great importance. At the preliminary design stage, Computational Fluid Dynamics (CFD) can be used as a fast and economic tool that provides detailed information on the flow field without the limitations associated with complex experimental setups.

Blockage is a velocity deficit that reduces the effective flow area. Compressor stall initiation is linked to the growth of the low velocity regions, particularly near the tip region [1, 2]. It is crucial to understand the sources of blockage losses in the compressor stage to optimize the design of axial compressors. The classical stall hypothesis, proposed by Emmons *et al.* [3], linked spike stall to the blockage growth caused by the separation of the suction side boundary layer; leading to high flow incidence angle. In transonic compressors, the blockage growth may be due to the shroud boundary layer separation downstream of the shock [4]. On the other hand, Chen *et al.* [5] did not observe any boundary layer separation induced by the shock while operating near stall in a transonic rotor. They linked the spike stall to the vortex breakdown created by the shock/tip leakage vortex (TLV) interaction. The low momentum region created by the tip vortex breakdown has been observed in both subsonic and transonic compressors [6, 7]. In transonic compressors operating at lower speeds, a secondary vortex along the blade suction surface may be another source of blockage [2]. Although these blockage regions may exist in the same compressor, the link between stall and the growth of a specific level of blockage is not yet clear. The objective of this study is to identify and understand the mechanisms of blockage growth that may lead to stall in an axial transonic compressor stage.

The quantification of blockage has been examined by many researchers; with Khalid [8] being the first to develop a method based on the 2-D boundary layer displacement thickness in which a main flow component was used. This component was derived from the radial circumferential angle profile at the mid-pitch which was then applied uniformly across the pitchwise direction. He stated that the main flow component was the most appropriate choice by showing that it satisfied a constant bulk velocity at a given mass flow rate regardless of the distribution of the defect and core regions. The blockage related to the endwalls was expressed as a function of a loading parameter. Khalsa [9] used the same approach to predict blockage but derived different blockage and loading parameters which depend on the chord and tip flow mass flux. Khalsa [9] argued that the blockage parameter should be dependent on the chordwise position rather than being only dependent on the blade spacing as stated by Khalid [8]. In a later study, Khalid *et al.* [10] used the parameters by Khalsa [9] to validate Navier-Stokes, passage-averaged, zero-equation CFD predictions

against the experimental observations from a rotating rig and a stationary cascade in a wind tunnel. The passage-average approach [11] is a steady-state method in which the relative motion of rotor and stator blades is accounted for by the deterministic stresses (similar to the Reynolds stresses in turbulence). Suder [12, 13] used the axial velocity component in his analysis despite its failure to achieve a constant bulk velocity at the same mass flow rate with different tip clearance gaps as shown by Khalid [8]. However, Suder showed good agreement with Khalid's results in terms of blockage variation with loading parameter. For centrifugal compressors, Khalfallah and Ghenaiet [14] used a meridional velocity component which is the magnitude of the streamwise and spanwise velocity component. In the present work, a new main flow component, based on the velocity angles in the streamwise, circumferential and spanwise directions, will be derived to be applicable to all types of compressors. The blockage will be calculated using both steady and unsteady RANS approaches and compared with previous computational and experimental work.

3.2 Geometry and numerical method

The compressor stage analyzed in this work is the first stage of an aeroengine multistage transonic compressor. The stage consists of 18 inlet guide vanes (IGV), 14 rotor blades (R) and 25 stator blades (S). The compressor rotor runs at 30,000 RPM and with Mach number of 1.6 at its tip. It has a low aspect ratio of 0.97 (ratio between the blade height at its inlet and blade chord), hub to tip ratio of 0.5 and tip clearance to chord ratio of 0.3%. The Reynolds number at the rotor tip is 1.2×10^6 . Steady and unsteady Reynolds-Averaged Navier-Stokes (RANS and URANS) simulations have been performed using ANSYS CFX 16.0 [15], which is a finite volume, coupled, pressure-based; multigrid solver [16]. The Rhie-Chow interpolation scheme [17] is used for pressure-velocity coupling. For all transport equations, a high-resolution advection scheme [18] that uses a non-linear blending function for each node is applied. Turbulence is accounted for using the shear stress transport model (SST) [19] since it is more suitable than the $k-\varepsilon$ model for wall-bounded flows and better for predicting the flow separation under adverse pressure gradients. Moreover, it allows the integration of the velocity inside the viscous sublayer [15]. It switches between the $k-\omega$ model near the wall and the $k-\varepsilon$ model away from the

wall through a blending function. The transport equations for the SST model are given in Section 2.3 of Chapter 2.

At the preliminary engineering design stage, it is more practical to simulate a single blade passage with periodic boundaries instead of the full wheel. The computational model is shown in Figure 3-1. Two stator blade passages are simulated in order to reduce the pitch ratio at the rotor/stator interface to be used for the unsteady simulations. A large intake is mounted upstream of the inlet guide vanes and a variable area nozzle is mounted downstream of the stator to avoid interactions between the blade rows and the effects of the boundary conditions at the inlet and outlet [20]. It has been shown that including a variable area nozzle at the compressor exit improves the stability of the simulations near stall [20]. The total pressure and temperature are imposed at the inlet while a constant static pressure is imposed at the outlet. Different operating points are obtained by changing the exit area of the nozzle. All blades, hubs and casings are set as no-slip adiabatic walls.

For the steady simulations, the mixing plane approach (MP) is applied at the IGV/rotor and rotor/stator interfaces [21]. A circumferential averaging of the flow quantities is performed at the interface while meridional profiles are conserved between the stationary and rotary components. For the unsteady simulations, two approaches have been applied. The profile transformation (PT) [22] is used at the inlet guide vane-rotor (IGV-R) interface and time transformation (TT) [23] for the rotor-stator (R-S) interface. For the profile transformation method, an instantaneous periodicity is applied at the periodic boundaries and the fluxes are scaled at the IGV-R interface to account for the pitch change. The time transformation method provides an improvement over the profile transformation by transforming the equations in time such that the instantaneous periodicity is applied without any approximation [24]. Since this method is limited to a certain range of pitch ratios, two stator blades were modeled to reduce the deviation from unity pitch ratio. For the TT method, the periodic boundary conditions for any variable at the rotor and stator boundaries are given by

$$\phi_{per1,R} \left(x, \theta, r, t - \frac{(\Delta\theta_{P_R} - \Delta\theta_{P_S})r\theta}{U_R \Delta\theta_{P_R}} \right) = \phi_{per2,R} \left(x, \theta + \Delta\theta_{P_R}, r, t - \frac{(\Delta\theta_{P_R} - \Delta\theta_{P_S})r\theta}{U_R \Delta\theta_{P_R}} \right) \quad (3-1)$$

$$\phi_{per1,S} \left(x, \theta, r, t - \frac{(\Delta\theta_{P_R} - \Delta\theta_{P_S})r\theta}{U_R \Delta\theta_{P_S}} \right) = \phi_{per2,S} \left(x, \theta + \Delta\theta_{P_S}, r, t - \frac{(\Delta\theta_{P_R} - \Delta\theta_{P_S})r\theta}{U_R \Delta\theta_{P_S}} \right) \quad (3-2)$$

where ϕ is any resolved variable. The governing equations (mass, momentum, energy and turbulence) are solved in the transformed time and then transformed back to the physical time before post processing the results.

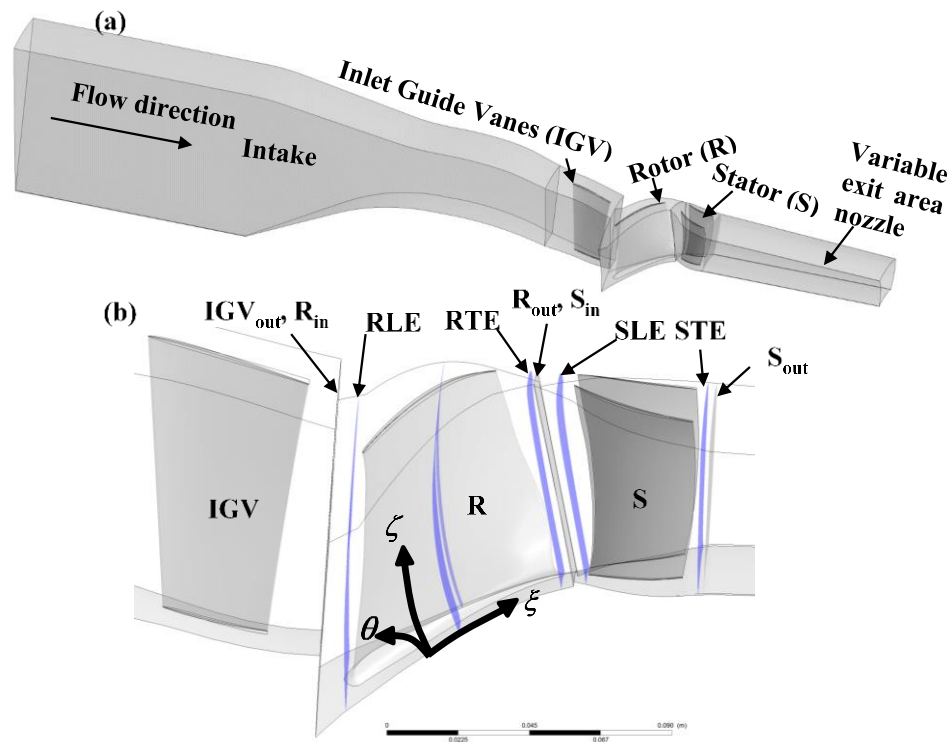


Figure 3-1 The computational domain of the axial compressor stage; (a) intake section, inlet guide vane (IGV), rotor (R), stator (S) and variable exit nozzle, (b) a close-up view of the main components showing the inlet and outlet planes for each component and the leading and trailing edge planes (RLE, RTE, SLE and STE). The streamwise, circumferential and spanwise directions are represented by ξ , θ and ζ , respectively.

In the following sections, unless mentioned, the time-averaged TT simulations are used for comparisons with the MP simulations. Since the unsteady simulations become quasi-steady (periodic with time) when the solution is converged, all the transient statistics are based on the last converged rotor blade pass period.

3.3 Grid and time independence study

The details of the grid resolution are listed in Table 3-1 for coarse, medium and fine meshes. Each grid refinement stage is carried out by doubling the node count in each direction. The O-J grid is used for the rotor and stator for a better mesh quality in the case of high stagger angles. ANSYS Turbogrid 16.0 is used for the mesh generation. The average value of y^+ is maintained below 2 for the blades and 5 for the hubs and shrouds. Kroll *et al.* [25] have shown that $y^+ < 5$ is sufficient for predictions of separation points and skin friction on transonic airfoils.

Table 3-1 Mesh data for each component

| Component Density | Intake | IGV | R | S | Nozzle |
|------------------------------------|----------------|----------------|----------------|----------------|----------------|
| Coarse | 143,450 | 182,707 | 364,569 | 306,236 | 70,602 |
| Medium | 533,286 | 1.51 M | 2.54 M | 1.32 M | 500,094 |
| Fine | 3.56 M | 11.3 M | 18.7M | 8.3 M | 1.69 M |

The grid independence tests are carried out at two operating points; a high and a low mass flow rate. Figure 3-2 depicts the circumferentially-averaged spanwise profiles of the total pressure normalized by the inlet values, as well as the velocity angle and turbulent kinetic energy (TKE) at the rotor and stator trailing edges for the low mass flow rate point. The TKE is normalized by the blade tip velocity squared. The profiles for the high mass flow point are not shown since the discrepancies in the results between the medium and fine grids are insignificant at high mass flow rates compared with those at low flow rates. The

root-mean-square (RMS) of the differences between each pair of grid levels normalized by the fine mesh mean profiles (except for the velocity angle) are listed in Table 3-2. The greatest deviations between the results are observed in the velocity angle and TKE at the low mass flow point. The medium to fine refinement results in maximum differences of 2 degrees in the velocity angle and 12 % of the fine mesh mean profile in the TKE at 3 % and 12% of the stator span, respectively. In general, the agreements between the medium and fine grids are far better than those between the coarse and medium grids. For this reason, the medium mesh is used throughout the present study.

For the sake of comparison, the mass flow at an intermediate point between the peak efficiency and peak pressure ratio is imposed for the three simulations at the compressor outlet boundary. The inlet boundary conditions remain the same for all operating points and cases studied. One hundred time steps per rotor blade pass are used for the TT simulations which is found to be adequate when compared with 200 time steps. Figure 3-3 shows the instantaneous static pressure at a point located at the leading edge of the tip section for the rotor (a) and stator (b). The abscissa is normalized by the blade passing period. The RMS changes between each time step level are less than 1% of the mean profile at 200 time steps as shown in Table 3-3. The 100 time steps simulation shows a better agreement with the 200 times steps and, therefore, the 100 time steps case has been chosen for this study.

The unsteady simulation for the highest efficiency operating point took about one week to converge using 60 processors. This corresponds to one rotor revolution. For lower mass flow simulations, the solution converged after two to three revolutions. The run was initialized using a mixing plane steady solution. Ten inner loop iterations per time step were used to achieve root mean square residuals of the order of 10^{-6} for all equations.

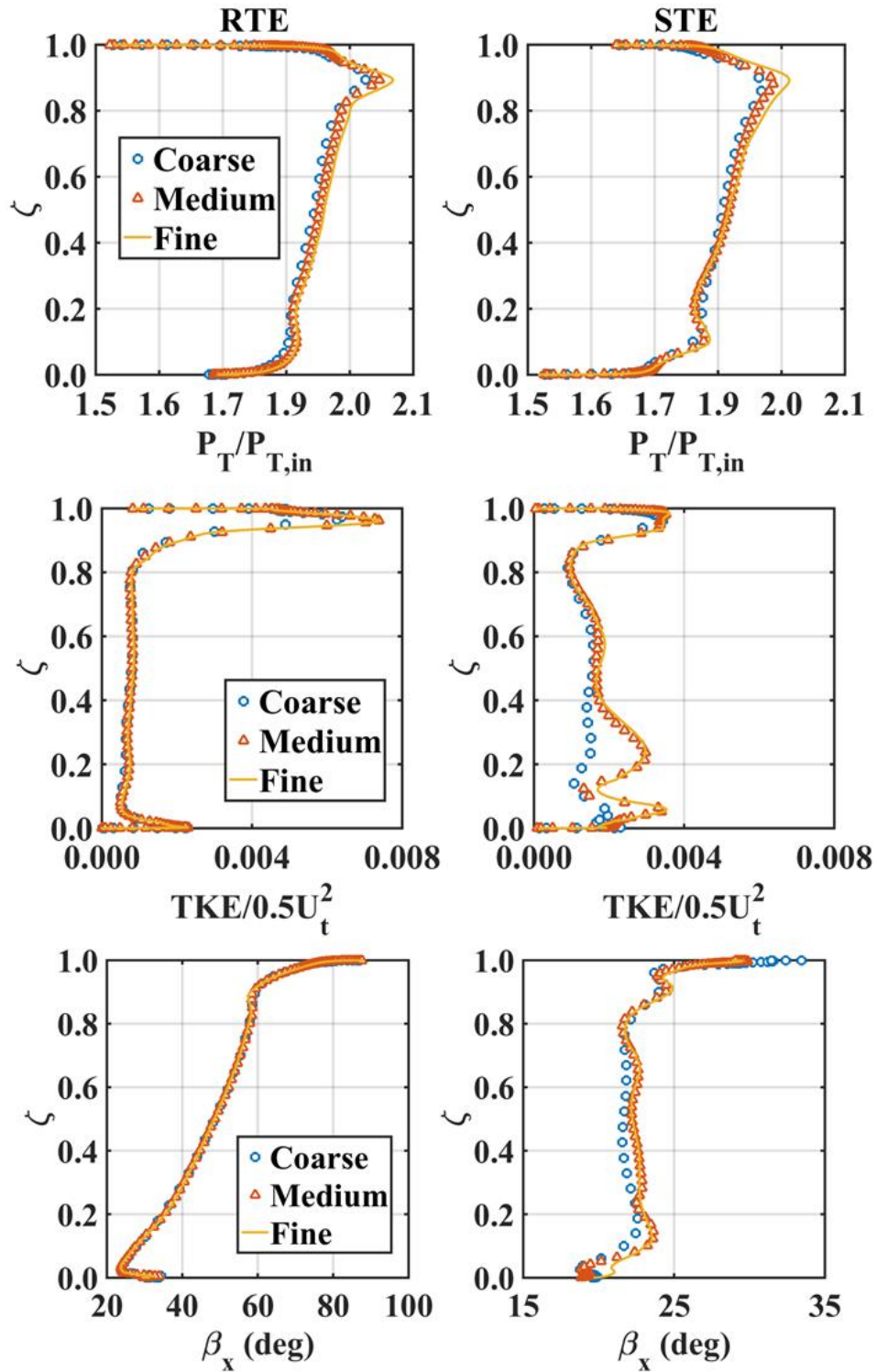


Figure 3-2 Grid independence test at the rotor and stator trailing edges (RTE and STE) for a low mass flow point

Table 3-2 Grid independence results. The values are based on the RMS differences normalized by the fine mesh mean profiles, except for the flow angle.

| Variable | Mesh change | | Mesh change | |
|-----------------------|---------------------------------|-------------------------------|--------------------------------|------------------------------|
| | Coarse-Medium High mass flow | Medium-Fine High mass flow | Coarse-Medium Low mass flow | Medium-Fine Low mass flow |
| Pressure ratio | 0.52 % | 0.52 % | 0.70 % | 0.54 % |
| Efficiency | 1.07 % | 0.34 % | 0.75 % | 0.18 % |
| Total pressure RTE | 0.49 % | 0.16 % | 0.84 % | 0.61 % |
| Total pressure STE | 0.79 % | 0.46 % | 0.89 % | 0.77 % |
| Total temperature RTE | 0.14 % | 0.24 % | 0.22 % | 0.15 % |
| Total temperature STE | 0.12 % | 0.06 % | 0.12 % | 0.11 % |
| Flow angle RTE | 0.59 deg | 0.44 deg | 0.62 deg | 0.34 deg |
| Flow angle STE | 1.37 deg | 0.57 deg | 0.96 deg | 0.83 deg |
| TKE RTE | 5.84 % | 2.69 % | 10.34 % | 3.27 % |
| TKE STE | 15.88 % | 2.88 % | 21.28 % | 4.31 % |

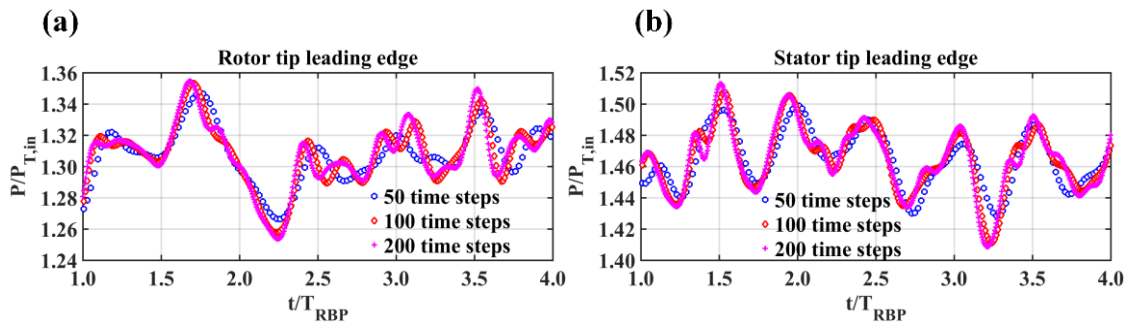


Figure 3-3 Time independence test showing the static pressure normalized by the total pressure at the inlet versus the time normalized by the rotor blade pass time (T_{RBP}) at (a) rotor tip leading edge and (b) stator leading edge tip

Table 3-3 RMS of the change in time step resolution. The values are normalized by their mean profiles at 200 ts.

| Point location | Rotor tip leading edge | | | Stator tip leading edge | | |
|------------------|------------------------|--------|---------|-------------------------|--------|---------|
| | 50-100 | 50-200 | 100-200 | 50-100 | 50-200 | 100-200 |
| Time step change | | | | | | |
| % RMS change | 0.68 % | 0.79 % | 0.42 % | 0.59 % | 0.76 % | 0.39 % |

3.4 Performance characteristics of the compressor stage

The pressure ratio and isentropic efficiency are plotted versus the normalized mass flow rate for both steady state with the MP and unsteady with the TT in Figure 3-4. All the reference values, which are used for the normalization, are obtained from the high efficiency point predicted by the TT simulation. It is well-known that choking takes place when the compressor mass flow rate is insensitive to the reduction of the static back pressure. This is obvious for the last two points at the right hand side of the plot where the compressor operates at its maximum flow rate. Researchers have often been concerned with reduced mass flow operating conditions on the left hand side of the characteristic curve since the compressor may experience the serious phenomena of stall and surge [3–7]. Massive separations and system vibrations resulting from stall may shorten the lifetime of a compressor and, therefore, it is crucial to understand the physics and mechanisms of stall in order to develop effective control systems. The mixing plane solution overpredicts the total pressure ratio by around 3%. The discrepancies between the steady and unsteady predictions in terms of the global performance will be discussed in Section 3.9. Two operating points are considered in the flow blockage analysis: a high efficiency point (HE), where the compressor should operate normally, and the peak pressure ratio point (PPR), where compressor stall might be triggered, as illustrated in Figure 3-4. Each operating point associated with a steady or unsteady map is followed by MP or TT, respectively. The operating points MP1 to MP4 and TT1 to TT4 will be used in Section 3.6.

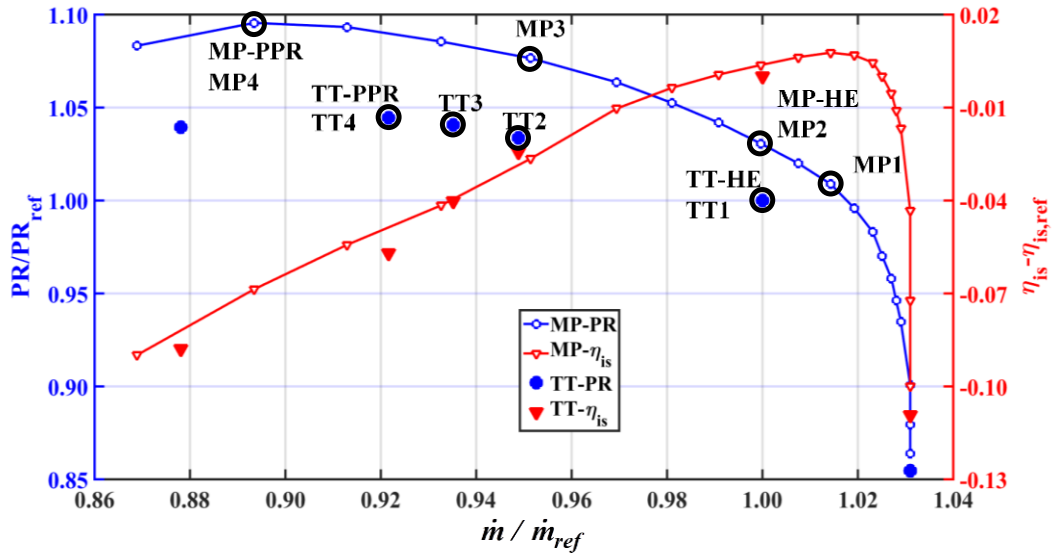


Figure 3-4 Performance characteristic for the normalized pressure ratio (PR/PR_{ref}) and isentropic efficiency ($\eta_{is} - \eta_{is,ref}$) vs. the normalized mass flow rate (\dot{m} / \dot{m}_{ref}).

The abbreviations MP, TT, HE and PPR stand for mixing plane, time transformation, high efficiency and peak pressure ratio. The marked operating points are used in Section 3.6

3.5 Quantification of blockage

The total blockage at each streamwise location, $B(\xi)$, is the reduction in the effective flow area, which is given by [13]

$$B(\xi) = 1 - \frac{\text{Effective area}}{\text{Geometric area}} = 1 - \frac{A - \int \delta^*(\zeta) d\zeta}{A} = \frac{\int \delta^*(\zeta) d\zeta}{A} \quad (3-3)$$

where A is the total flow area of the streamwise plane where the blockage is calculated and $\delta^*(\zeta)$ is assumed to be the integration of the main flow mass flux deficit (ρu_m deficit) along the circumferential direction, θ , at a given normalized spanwise location, ζ [13]. The spanwise coordinate is used instead of the radial coordinate to accommodate both axial and radial compressors. Analogous to the displacement thickness of boundary layer theory,

$\delta^*(\zeta)$ is obtained at each constant normalized spanwise and streamwise location, (ζ, ξ) , using the following equation

$$\delta^*(\zeta) = \int_{\theta_{min}(\zeta)}^{\theta_{max}(\zeta)} \left(1 - \frac{(\rho u_m)}{(\rho u_m)_{inviscid}} \right) \zeta d\theta \quad (3-4)$$

The circumferential blockage, $B(\xi, \zeta)$, at each spanwise position is calculated by simply dividing the displacement thickness by the corresponding arc length

$$B(\xi, \zeta) = \frac{\delta^*(\zeta)}{\zeta (\theta_{max}(\zeta) - \theta_{min}(\zeta))} \quad (3-5)$$

The main flow velocity is obtained by projecting the relative flow velocity vector onto the main flow vector. The main flow vector is predicted by introducing the effect of dominant flow angles in all directions (i.e., streamwise, spanwise and circumferential angles) instead of only the circumferential component as in [8]. For a given streamwise plane, the angles for the three directions are obtained at each node and a linear surface-weighted fit is implemented. The fit weighting reduces the influence of the regions of both high relative velocity magnitude and large angles. Figure 1-8(a) of Chapter 1 shows an example for generating the streamwise main flow angle as a function of θ and ζ at a given streamwise plane. It is noted that the spanwise flow angle shows the smallest spatial variations compared to the other flow angles.

For each span location, the combined effect of blade boundary layers and any vortices or wakes will be included in the integration. To obtain the inviscid main flow mass flux, a defect region is calculated using spanwise and circumferential gradients of the main flow mass flux.

$$Defect\ Region = \sqrt{\left(\frac{\partial(\rho u_m)}{\partial \zeta}\right)^2 + \left(\frac{1}{\zeta} \frac{\partial(\rho u_m)}{\partial \theta}\right)^2} \geq Cutoff \quad (3-6)$$

$$Cutoff = COF \left(\frac{\overline{\rho u_m}}{D}\right)^m_{Streamwise\ plane}$$

where *Cutoff* is proportional to the main flow mass flux at the streamwise plane of interest [14]. The predicted displacement thickness is not sensitive to the cutoff value since the gradients are much stronger in the defect region [8, 13]. The value of cutoff coefficient (*COF*) is taken as 3 since values between 1 and 4 have been shown to have no significant effect on the blockage calculations [8, 13, 14]. The mass-weighted average, $\left(\frac{\overline{\rho u_m}}{D}\right)^m$, is calculated at the streamwise plane of interest. Figure 1-8(b) of Chapter 1 shows the defect region at a streamwise plane located at 50% of the blade tip chord. The small regions of low gradients located inside the defect region are associated with low flux regions. Therefore, they are combined with the defect region by locally setting a flux cutoff value based on the maximum flux at the plane. The inviscid main flow mass flux field $(\rho u_m)_{inviscid}$ has the same value as the local flux field (ρu_m) in the core region (i.e. the region outside the defect zone) which gives zero local blockage at these points. On the other hand, the inviscid flux field within the defect region is extrapolated from the local flux field at the core region using a thin plate spline as shown in Figure 1-8(c) of Chapter 1.

3.6 Comparison with previous work

A parametric method was developed by Khalid [8], Khalsa [9] and Khalid *et al.* [10] to link a normalized tip leakage blockage expression with a loading parameter. This section presents a comparison between the current results and data from previous studies [8–10]. Figure 3-5 shows the variation of the normalized blockage against the loading parameter and a comparison between the present data and the CFD results of Khalid [8] for different

stator and rotor geometries. The normalized blockage is calculated by the following equation,

$$\text{BLK}_{\text{Khalid 1995}} = \frac{A_b \cos \beta_e}{\tau s / \sin \beta_{vm}} \quad (3-7)$$

where A_b is the blockage area due to the tip leakage flow, β_e is the circumferentially-averaged main flow angle measured from the streamwise direction, τ is the tip clearance gap, s is the blade spacing, and β_{vm} is the vector mean flow angle with respect to the axial direction. The loading parameter is calculated by the following equation,

$$\text{LdP}_{\text{Khalid 1995}} = \frac{\overline{\Delta P}^a - \overline{\Delta P_T}^a}{Q_{\text{Freestream}}} \quad (3-8)$$

where $\overline{\Delta P}^a$, $\overline{\Delta P_T}^a$ are the differences between the area-weighted average $(\overline{\quad})^a$ of the static and relative total pressure, respectively, across the leakage defect region and the freestream value. The freestream dynamic head, $Q_{\text{Freestream}}$, is area-averaged over a plane extending radially 10τ away from the casing boundary layer. In the present study, the parameters are obtained at four streamwise locations, 25%, 50%, 75% and 100% of the rotor chord at its tip. Four operating points are selected from the steady (MP) and unsteady (TT) performance maps. The selected operating points are arranged in a descending order according to the compressor mass flow rate as illustrated in the performance characteristic (see Figure 3-4). The trend of the current data shows a good agreement with the CFD data from Khalid [8], particularly the steady simulations. Since the operating range has been extended by introducing the nozzle, higher blockage values are obtained at off-design points. The unsteady simulation shows higher tip leakage blockage than that of the steady simulation at the same loading parameter. A maximum blockage parameter discrepancy of 100% is observed at the last stable point by the unsteady simulation (TT4) at 25% of the rotor chord. The general trend depicts an asymptotic behavior at loading parameter values between 0.7 and 0.8. It is noteworthy that Khalid's simulations were not time accurate since

a local time stepping was used and, therefore, the present MP simulations agree better with his data.

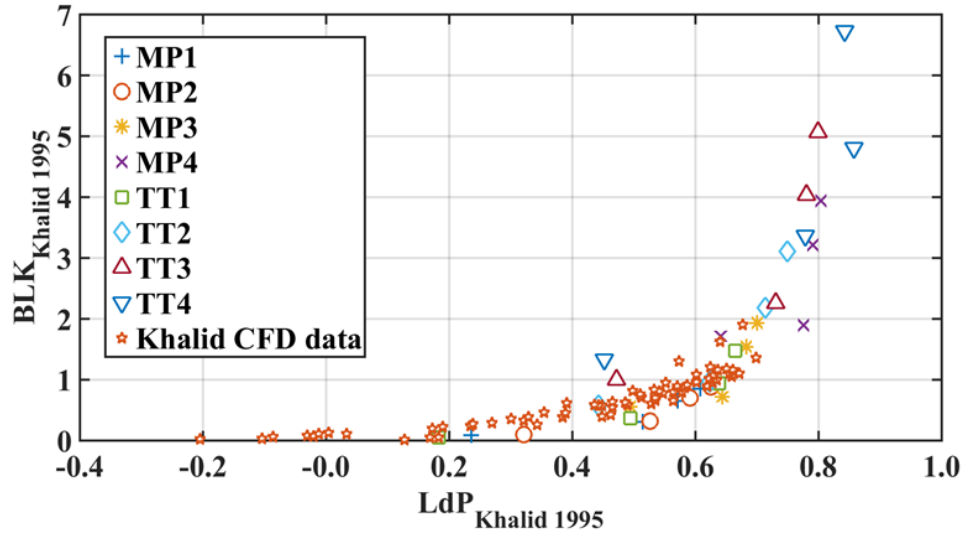


Figure 3-5 Variation of blockage parameter vs. loading parameter and comparison with Khalid [8]. The operating points are illustrated in Figure 3-4.

Another form of the loading and blockage parameters is used to compare with the experimental data of Khalsa [9] and Khaled *et al.* [10]. Khalsa argued that Khalid's blockage loading parameter [8], which eliminates the dependence on the chord length, is an inaccurate representation of blockage. The normalized blockage in this case is calculated as follows:

$$\text{Blockage parameter } \text{BLK}_{\text{Khalsa 1995}} = \frac{A_b \cos \beta_e}{\tau c} \quad (3-9)$$

where c is the rotor chord at its tip. The loading parameter is calculated by

$$\text{LdP}_{\text{Khalsa 1995}} = \left[\left(\frac{P_{\text{Defect,TLV}}^a - P_{\text{Local}}}{P_{\text{T,FreeStream}} - P_{\text{Local}}} \right) - \left(\frac{P_{\text{T,Defect,TLV}}^a - P_{\text{T,FreeStream}}}{P_{\text{T,FreeStream}} - P_{\text{Local}}} \right) \right]^m \quad (3-10)$$

where, $\overline{P_{Defect,TLV}^a}$, $\overline{P_{T,Defect,TLV}^a}$ are the area-weighted average of static and total pressures over the defect area due to the tip leakage at the streamwise plane of interest. The freestream total pressure $P_{T,Freesream}$ is area-averaged over a plane extending radially 10τ away from the casing boundary layer. P_{Local} is the local static pressure at a point located at the suction surface. The local loading parameter is mass-averaged $\left(\overline{(\cdot)^m}\right)$ over the tip clearance gap extending from the leading edge to the location of interest.

Figure 3-6 shows a comparison between the current blockage-loading data and the experimental data of Khalsa [9] and Khaled *et al.* [10] both carried out with both a wind tunnel and a rotating rig. The range of their measurement uncertainties (95% confidence in the velocity measurements) is shown by the shaded area within which most of the present CFD data lie. Again, the TT4 point shows a 100% blockage deviation from the experiments at 25% of the rotor chord which suggests that the data are not well collapsed as the compressor runs near stall. It is noteworthy that the experimental data were taken at the trailing edge of both test rigs which limits the data range. On the other hand, the present CFD data are taken at four streamwise positions for each operating point.

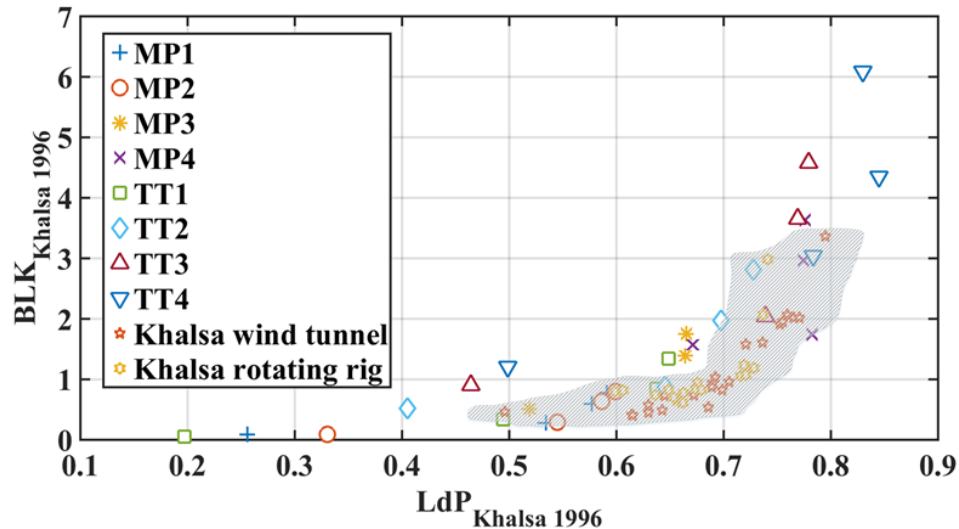


Figure 3-6 Variation of blockage parameter vs. loading parameter and comparison with Khalsa [9] and Khalid *et al.* [10]. The shaded area represents the region of experimental uncertainty of the measurements.

3.7 Blockage development in the stage

To quantify the flow blockage along the compressor stage, a number of streamwise planes are considered to calculate the distribution of the radial blockage. The data are collected for 11 planes at the rotor passage and 10 planes at the stator passage and then the contours are generated as shown in Figure 3-7. The data are shown for the two operating points obtained from steady and unsteady simulations, MP-HE, MP-PPR, TT-HE, and TT-PPR (See Figure 3-4). Although both steady and unsteady simulations for the high efficiency case have the same flow rate, the unsteady simulation shows a slight increase of the local blockage at the rotor tip region when compared to the steady results as shown in Figure 3-7(a, c). This explains the higher blockage parameter for the unsteady simulations at a given loading parameter seen in Figure 3-5. For the peak pressure ratio point (PPR), both simulations exhibit a significant growth of the blockage due to the tip leakage flow as shown in Figure 3-7(b, d). Again, the TT simulations show higher tip flow blockage than the MP simulations. The blockage trough located underneath the tip leakage influence zone is caused by the shock-induced suction-surface boundary layer separation. The separated region caused by the passage shock is shown in Figure 3-8 at 75% span for MP-PPR and TT-PPR. At the stator passage, a significant growth of the low velocity region is observed near the hub up to mid-span due to breakdown of the hub leakage vortex, resulting in a radial flow which is considered a strong cross flow in this case. The MP simulation predicts higher stator blockage because the peak pressure ratio operating point is achieved at a lower flow rate than that of the TT simulations.

The total blockage distribution along the stage using the MP and TT simulations are in good agreement at the HE point (within 1%) as shown in Figure 3-9. However, due to the rotor tip leakage blockage, the TT simulation predicts a higher total blockage than the MP simulation. As expected from the contours, the total blockage at the stator is higher for the MP simulations. It is noted that the stator blockage grows in a linear fashion unlike that of the rotor which grows in a piecewise linear trend. For the PPR point, the TT-PPR shows higher total blockage by 2.5% at the rotor outlet and lower blockage by 12% at the stator outlet when compared to the MP-PPR. The effect of the upstream inlet guide vanes has

contributed to the increase in the rotor tip blockage and the rotor wake has decreased the breakdown of the stator hub leakage vortex.

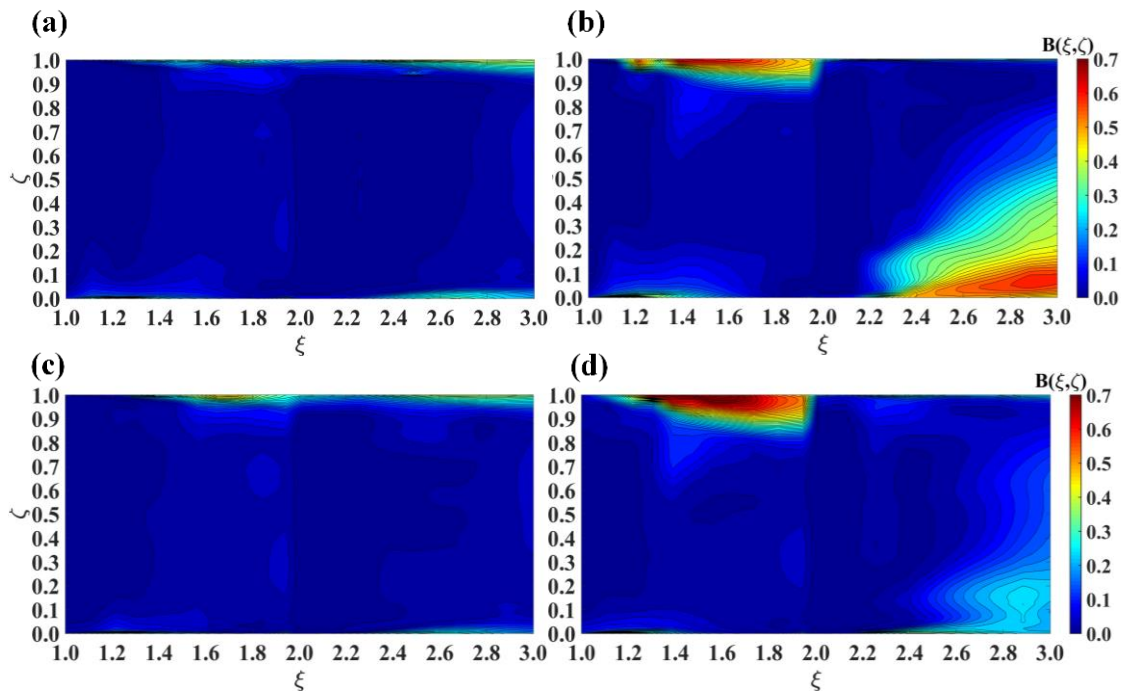


Figure 3-7 Contours of the circumferential blockage at different normalized streamwise and spanwise locations for; (a) MP-HE, (b) MP-PPR, (c) TT-HE, (d) TT-PPR

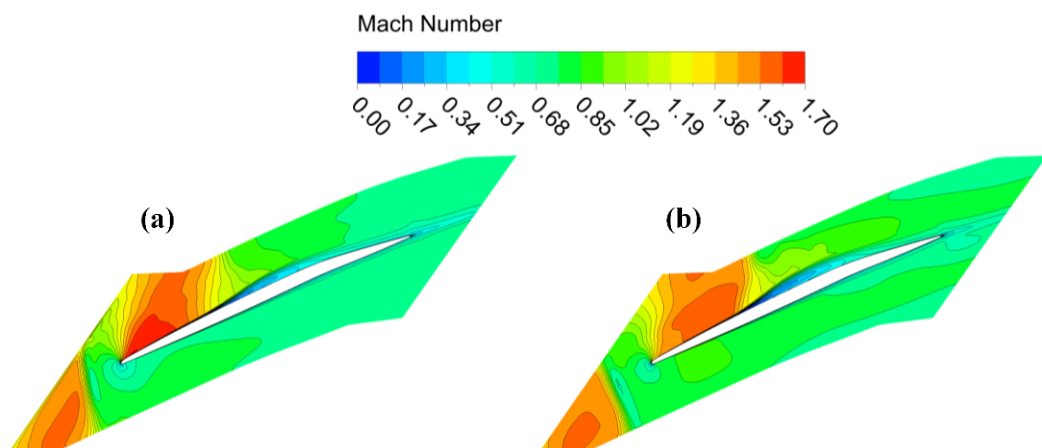


Figure 3-8 Contours of Mach number at 75% span for; (a) MP-PPR and (b) TT-PPR

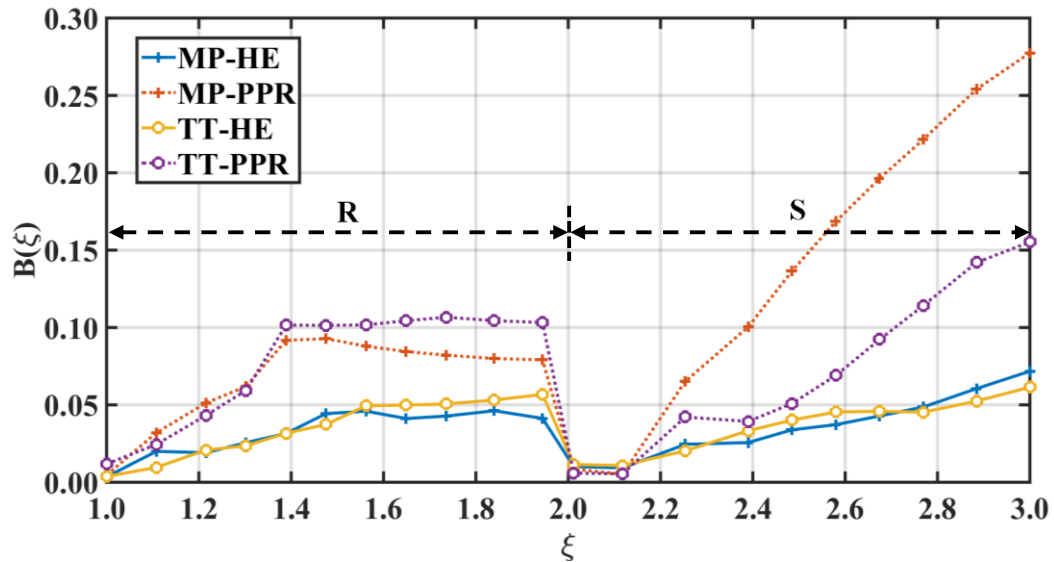


Figure 3-9 Total blockage development along the stage

3.8 The unsteadiness of the flow in the stage

Compressors experience high levels of unsteadiness, particularly at the tip region, when they operate at near stall conditions [26]. The rotor blade suction surface (R-SS) exhibits a large perturbation of the pressure, up to 20% of the rotor inlet, pressure around the tip region at the PPR point. The influence of this region extends from the shroud to 20% of the span inward. The tip flow interacts with the wall and the suction surface boundary layers resulting in their separation. The rotor wake also has an impact on the pressure fluctuations on the stator suction surface (S-SS). The contours for standard deviation of the unsteady pressure on the blades and walls at the HE and PPR points are shown in Figure A-1 of Appendix A. To investigate the unsteadiness within the blade passage, the entropy, which represents the losses, and the velocity, which represents the vector flow field are shown in terms of their standard deviation values. The variables are normalized by the mass average at the rotor inlet. Figure A-2 of Appendix A shows the regions of high entropy perturbation. As expected, most of the unsteady flow behavior at off-design conditions is linked to the tip flows at both the rotor and stator passages. The level of unsteadiness is higher in the stator due to the migration of the rotor wake inside the stator passage. The same trend is observed with the velocity magnitude, as shown in Figure A-3

of Appendix A (S-outlet, PPR). The stator hub leakage flow significantly contributes to the losses in the stator when the compressor operates near the peak pressure ratio.

The effect of the unsteadiness on blockage is examined by selecting four time steps which correspond to four rotor positions within the blade pass period. These time steps are chosen where the area average of the velocity near the rotor and stator walls shows the highest and lowest values. The rotor position $0.45T_{RBP}$ and $0.70T_{RBP}$ correspond to low and high average velocity near the rotor tip while $0.09T_{RBP}$ and $0.77T_{RBP}$ correspond to high and low velocities near the stator hub, respectively. The rotor position is shown at each time step. The variation of the blockage parameter with the loading parameter at four streamwise locations is shown in Figure 3-10 for the TT-PPR point. The maximum blockage fluctuations are observed at the rotor trailing edge which gives 20% of the mean value. The streamwise blockage at each time step is shown in Figure 3-11. The peak variations of the blockage occur at the rotor trailing edge due to the downward shift of the TLV. The maximum change in rotor TE blockage is 2.5% while the stator blockage fluctuates within 1.5% along the passage.

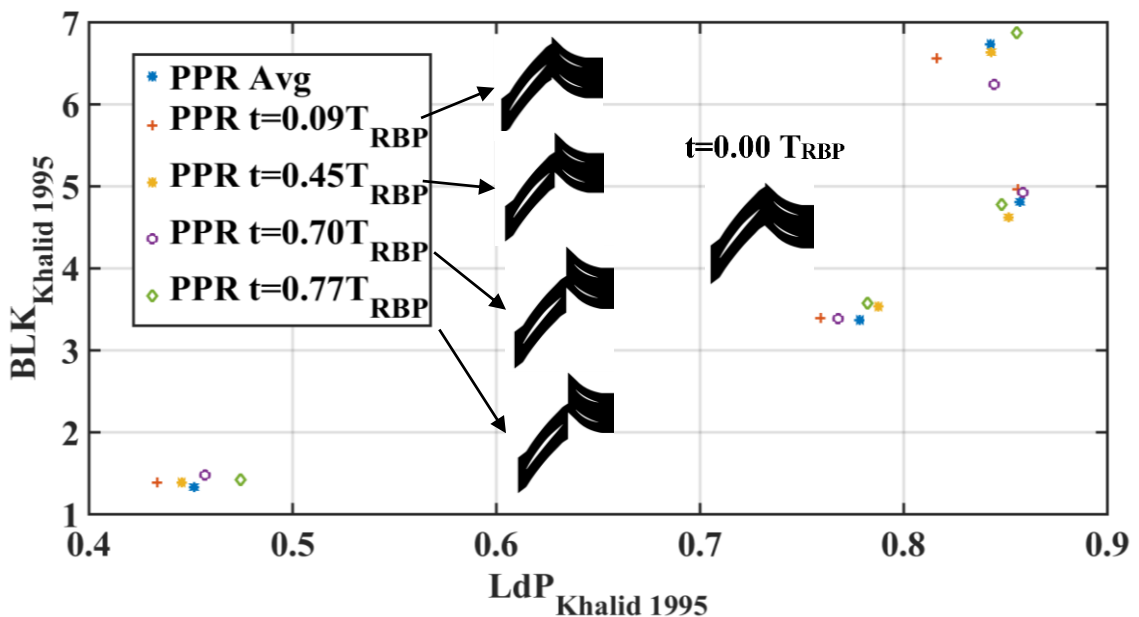


Figure 3-10 Variation of the blockage parameter against Khalid's loading parameter at TT-PPR at different time steps

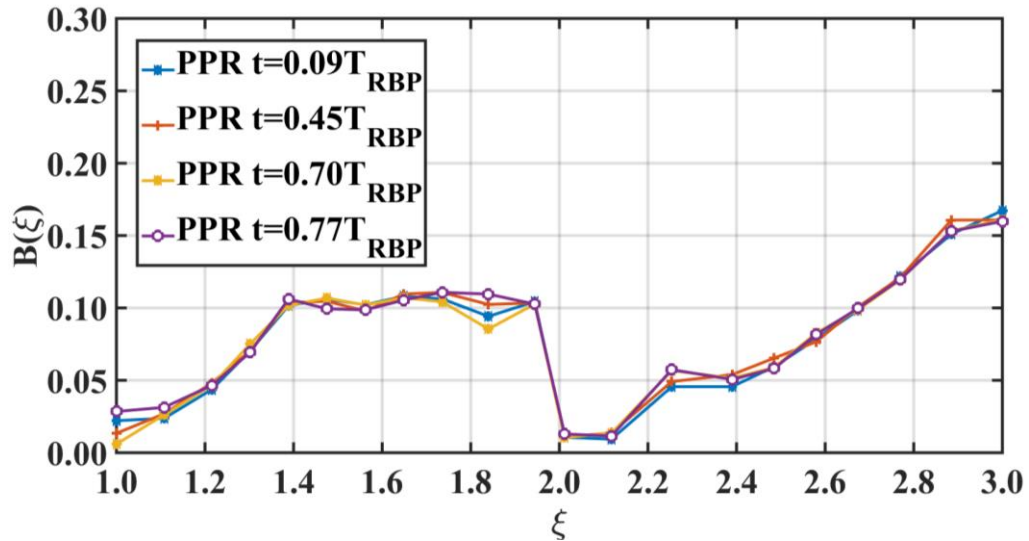


Figure 3-11 Variation of total blockage along the streamwise position at TT-PPR at different rotor positions

3.9 The global performance with respect to the interface type

The performance map in Figure 3-4 shows that the pressure ratio predicted by the TT simulation is lower than that predicted by MP simulation at the HE point by about 2.7%. To investigate the reason for this difference, the mass-averaged total pressure is plotted against the streamwise location in Figure 3-12. The streamwise scale starts at the IGV inlet and ends at the stator exit with an interval of 1 for each component. The deviation between the simulations begins as the flow enters the rotor blade and increases gradually until the rotor outlet where it gives the 2.7% difference in the performance map. The difference is then transferred approximately in a uniform fashion to the stator passage. To examine the contribution of the averaged pressure at a given spanwise location, the circumferentially-averaged total pressure profile is plotted against the normalized span in Figure 3-13. The rotor inlet profiles agree well, as expected, while the deviation is clear at the rotor inlet at all spanwise locations with a maximum difference of 3.8%. The deviation between predictions at the stator passage is almost the same along the stator passage.

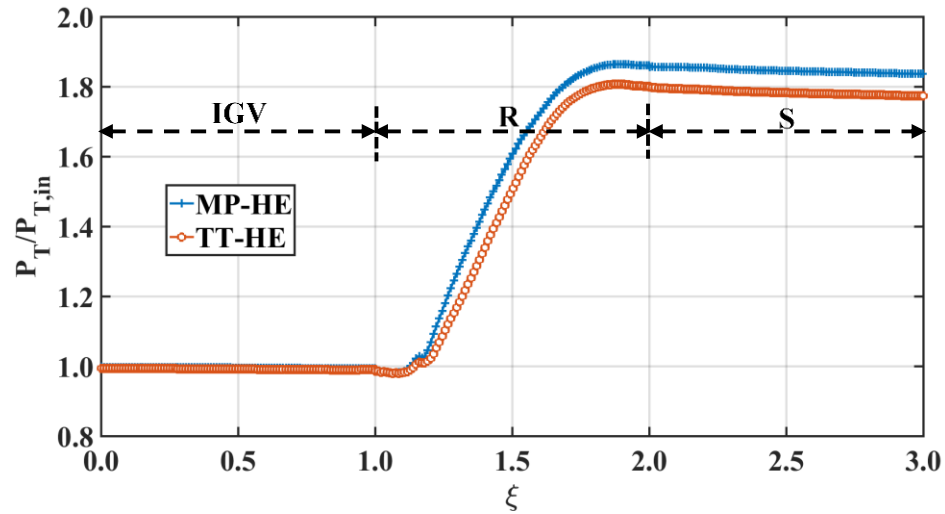


Figure 3-12 Streamwise profile of the total pressure at HE

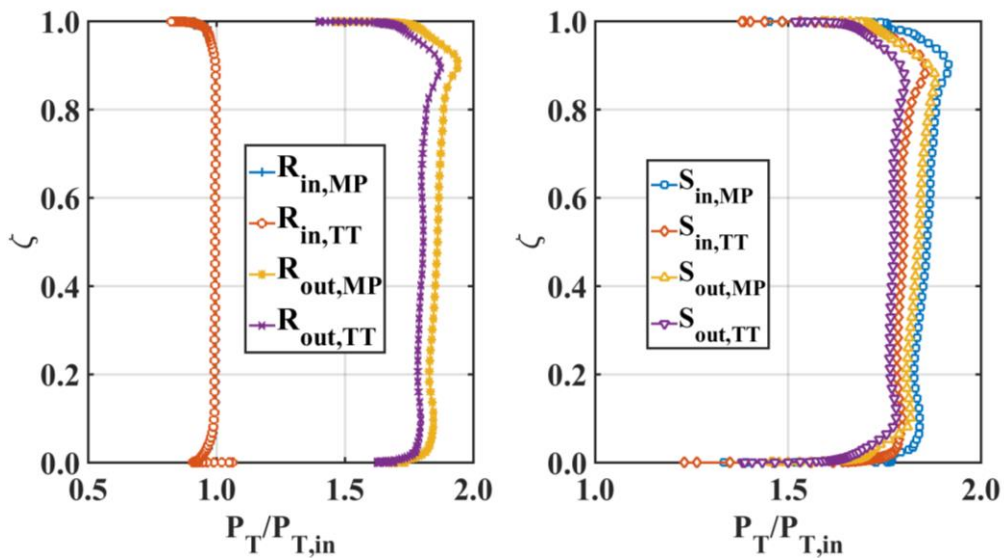


Figure 3-13 Spanwise profile of the circumferential average of the total pressure at HE

The effect of the inlet and outlet total pressure distribution on the rotor flow field is investigated using steady solutions for the isolated rotor with four different combinations of the boundary values, calculated by the MP and TT solutions at the HE point. All the results are calculated at the same mass flow rate and the static pressure profile from the full simulations is imposed at the outlet. The total pressure profiles for the four simulations

indicate the sensitivity of the solution to the inlet profile rather than the outlet profile, as shown in Figure 3-14. The regions of high total pressure at the inlet plane indicate the influence of the passage shock wave. The MP solution mixes out the effect of the shock waves. The rescaling of the IGV wakes, associated with the profile transformation in the TT solution, might contribute to the drop in the total pressure. To show if the rotor inlet has more influence than the rotor exit field, the total pressure ratio is plotted for the four cases in Figure 3-15. Considering the TT boundaries as the reference case, the MP solution leads to 3.5% increase in the total pressure. The MP boundary condition has more influence on the solution when imposed at the rotor inlet. This is obvious by the 2.8% and 0.7% increase in the pressure ratio when imposing $MP_{in}-TT_{out}$ and $TT_{in}-MP_{out}$, respectively.

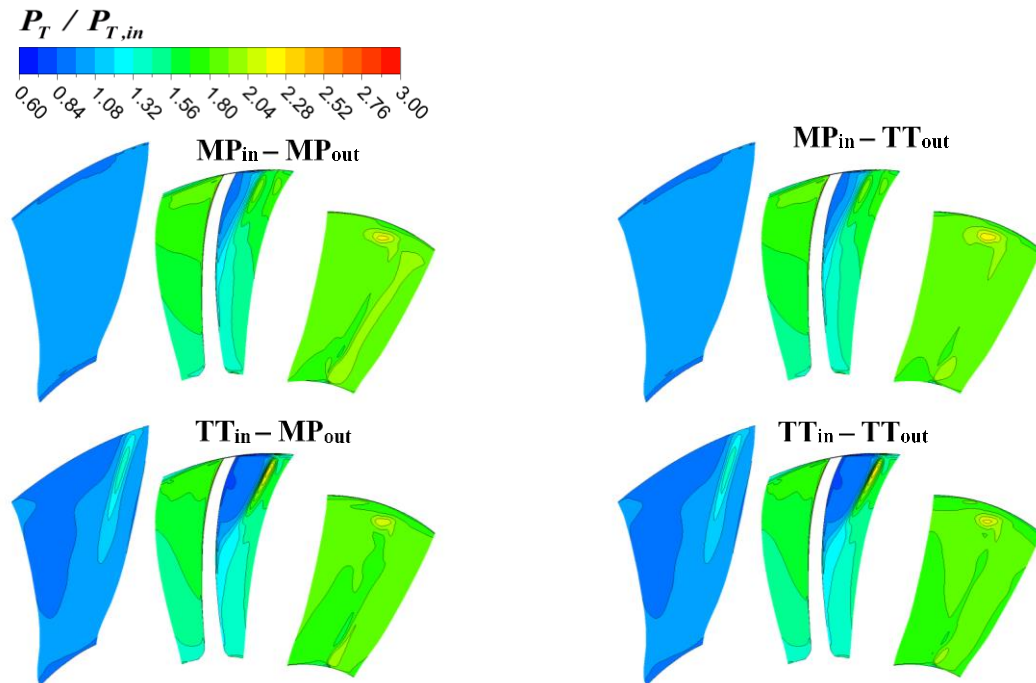


Figure 3-14 Total pressure contours for the isolated rotor steady simulations at the rotor inlet, mid-streamwise location and outlet

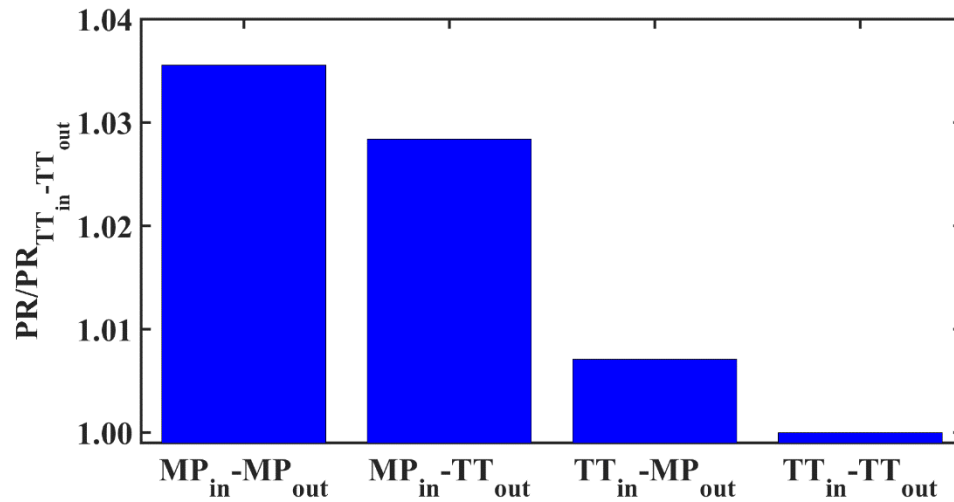


Figure 3-15 Total pressure ratio for each isolated rotor simulation with respect to the TT_{in}-TT_{out} case

3.10 Conclusions

Blockage development in an aeroengine transonic axial compressor stage has been investigated using the CFD commercial software ANSYS CFX. Boundary layer theory has been adopted to quantify the distribution of the blockage in the spanwise direction. A main flow velocity component has been generated based on a linear surface fit of the inviscid flow mass flux at the plane of interest. This method is applicable for all types of compressors since it accounts for all velocity components. Steady and unsteady RANS simulations using the time transformation approach have been used to quantify local and global flow blockage along the rotor and stator passages of the present compressor.

The variation of the rotor tip leakage blockage parameter with the loading parameter has shown a similar trend to those from previous experimental and numerical modelling. The distribution of the local circumferential blockage along the stage has given a good insight to the possible stall initiation mechanisms. The steady simulation results at the peak pressure ratio point indicate that the blockage is significant near the rotor tip and the stator hub due to the rotor tip and stator hub leakage flows, respectively. The high levels of circumferential and total blockage at the stator suggest that stall might initiate in the stator of the compressor stage examined here. The blockage calculated from the time-averaged

simulations at the peak pressure ratio point has shown an increase of total blockage by 2.5% at the rotor outlet and a decrease by 12% at the stator outlet when compared to the steady simulations. The effect of the upstream inlet guide vanes has contributed to the increase in the rotor tip blockage and the rotor wake has decreased the breakdown of the stator hub leakage vortex. For the high efficiency operating point, both steady and unsteady time-averaged simulations have shown close blockage values along the stage.

Although both steady and unsteady time-averaged results have shown the same blockage trends at the high efficiency operating point, some differences have been observed in terms of the pressure ratio. The regions of unsteadiness are mainly located at the rotor tip and at the stator tip and hub where the leakage vortices prevail. Despite predicting identical averaged total pressure at the rotor inlet, the steady solution shows higher pressure ratio by 3% when compared with the unsteady predictions at the high efficiency operating point. The rotor inlet total pressure distribution has the dominant influence on the total pressure rise distribution along the stage. For the profile transformation approach implemented at the rotor-IGV interface, the rescaling of the rotor wake leads to more pitchwise variations in the pressure profile. On the other hand, the mixing plane approach mixes out the effect of the upstream wakes and the shock wave, resulting in a more uniform total pressure distribution and, hence, more pressure rise along the stage.

The next chapter investigates the influence of the axial gap between the rotor and stator on the global performance and local flow field of the same axial stage using the time transformation method.

3.11 References

- [1] J. J. Adamczyk, M. L. Celestina, and E. M. Greitzer, “The role of tip clearance in high-speed fan stall,” *ASME J. Turbomach.*, vol. 115, no. 1, pp. 28–38, 1993.
- [2] K. L. Suder and M. L. Celestina, “Experimental and computational investigation of the tip clearance flow in a transonic axial compressor rotor,” *ASME J. Turbomach.*, vol. 118, no. 2, pp. 218–229, 1996.
- [3] H. W. Emmons, C. F. Pearson, and H. P. Grant, “Compressor surge and stall propagation,” *Trans. ASME*, vol. 77, no. 1, pp. 455–469, 1955.
- [4] C. Hah, D. Rabe, and A. Wadia, “Role of tip-leakage vortices and passage shock in stall inception in a swept transonic compressor rotor,” in *Proc. ASME Turbo Expo*, Vienna, Austria, 2004.
- [5] J.-P. Chen, M. D. Hathaway, and G. P. Herrick, “Prestart behavior of a transonic axial compressor stage via time-accurate numerical simulation,” *ASME J. Turbomach.*, vol. 130, no. 4, pp. 1–12, 2008.
- [6] M. Furukawa, M. Inoue, K. Saiki, and K. Yamada, “The role of tip leakage vortex breakdown in compressor rotor aerodynamics,” *ASME J. Turbomach.*, vol. 121, no. 3, pp. 469–480, 1999.
- [7] K. Yamada, K. Funazaki, and H. Sasaki, “Numerical investigation of relation between unsteady behavior of tip leakage vortex and rotating disturbance in a transonic axial compressor rotor,” in *Proc. ASME Turbo Expo*, Berlin, Germany, 2008.
- [8] S. Khalid, “The effects of tip clearance on axial compressor pressure rise,” Ph.D. dissertation, Department of Mechanical Engineering, Massachusetts Institute of Technology, USA, 1995.
- [9] A. S. Khalsa, “Endwall blockage in axial compressors,” Ph.D. dissertation,

Department of Mechanical Engineering, Massachusetts Institute of Technology, USA, 1996.

- [10] S. A. Khalid, A. S. Khalsa, I. A. Waitz, C. S. Tan, E. M. Greitzer, N. A. Cumpsty, J. J. Adamczyk, and F. E. Marble, "Endwall blockage in axial compressors," *ASME J. Turbomach.*, vol. 121, no. 3, pp. 499–509, 1999.
- [11] J. J. Adamczyk, "Model equation for simulating flows in multistage turbomachines," in *ASME Paper No. 85-GT-226*, 1985.
- [12] K. L. Suder, "Blockage development in a transonic, axial compressor rotor," *ASME J. Turbomach.*, vol. 120, no. 3, pp. 465–476, 1998.
- [13] K. L. Suder, "Experimental investigation of the flow in a transonic , axial flow compressor with respect to the development of blockage and loss," Ph.D. dissertation, Department of Mechanical and Aerospace Engineering, Case Western Reserve University, USA, 1996.
- [14] S. Khalfallah and A. Ghenaiet, "Analyses of radial compressor stability improvement by casing treatment," *Proc. IMechE Part A J Power Energy*, vol. 226, no. 7, pp. 807–821, 2012.
- [15] *Ansys CFX-Solver Theory Guide. ANSYS CFX Release 16.0.* Ansys Inc., Canonsburg, PA, 2015.
- [16] M. Raw, "Robustness of coupled algebraic multigrid for the Navier-Stokes equations," in *Proc. AIAA 34th Aerospace Sciences Meeting and Exhibit*, Reno, Nevada, USA, 1996.
- [17] C. Rhie and W. Chow, "Numerical study of the turbulent flow past an airfoil with trailing edge separation," *AIAA J.*, vol. 21, no. 11, pp. 1525–1532, 1983.
- [18] T. J. Barth and D. C. Jespersen, "The design and application of upwind schemes on unstructured meshes," in *Proc. 27th Aerospace Sciences Meeting*, Reno, Nevada,

USA, 1989.

- [19] F. R. Menter, “Two-equation eddy-viscosity turbulence models for engineering applications,” *AIAA J.*, vol. 32, no. 8, pp. 1598–1605, 1994.
- [20] M. Vahdati, A. I. Sayma, C. Freeman, and M. Imregun, “On the use of atmospheric boundary conditions for axial-flow compressor stall simulations,” *ASME J. Turbomach.*, vol. 127, no. 2, pp. 349–351, 2005.
- [21] J. D. Denton, “The calculation of three dimensional viscous flow through multistage turbomachines,” *ASME J. Turbomach.*, vol. 114, no. 1, pp. 18–26, 1992.
- [22] P. Galpin, R. Broberg, and B. Hutchinson, “Three-dimensional Navier-Stokes predictions of steady state rotor/stator interaction with pitch change,” in *Proc. 3rd Ann. Conference of the CFD Society of Canada*, Banff, Canada, 1995.
- [23] M. B. Giles, “Calculation of unsteady wake/rotor interaction,” *AIAA J. Propuls. Power*, vol. 4, no. 4, pp. 356–362, 1988.
- [24] L. Zori, P. Galpin, R. Campregher, and J. C. Morales, “Time transformation simulation of 1.5 stage transonic compressor,” in *Proc. ASME Turbo Expo*, Montreal, Canada, 2015.
- [25] N. Kroll, D. Schwamborn, K. Becker, H. Rieger, and F. Thiele, *MEGADESIGN and MegaOpt – German Initiatives for Aerodynamic Simulation and Optimization in Aircraft Design*, Vol. 107. Springer, 2007.
- [26] D. Lee, P. D. Orkwis, F.-L. Tsung, W. Magnuszewski, C. Noll, and G. S. McNulty, “Tip flow unsteadiness and blade row interactions for a low-speed compressor rotor,” *AIAA J. Propuls. Power*, vol. 29, no. 6, pp. 1346–1356, 2013.

Chapter 4

4 Numerical simulation of the influence of rotor-stator axial gap on the unsteady 3D flow field in a single stage axial compressor

This chapter examines the effect of rotor-stator axial gap on the global and local performance of an axial transonic stage using 3D unsteady numerical simulations. The predicted global and local performance with respect to the normalized axial gap is compared with the previous literature results. A simple 2D wake model is used to investigate the mechanisms of the rotor wake decay with respect to three different rotor-stator gaps. Section 4.1 reviews a survey of the previous studies on the effect of the rotor-stator axial gap on the compressor performance. Section 4.2 discusses the numerical approaches used to simulate the air flow in the compressor. The following sections discuss the influence of the rotor-stator gap on different parameters. Finally, conclusions are presented.

4.1 Introduction

The recent trends in aeroengine design aim at compact, high-efficiency and high pressure ratio turbo compressors [1]. One of the important design parameters is the axial gap between the rotary and stationary components in a compressor stage. The rotor-stator (R-S) axial gap is a trade-off between the unsteadiness and global performance. A smaller axial gap can lead to a higher pressure ratio at the expense of high vibration and noise levels due to high flow field perturbations [2, 3]. The flow in a compressor stage is inherently unsteady due to the interaction between the propagating rotor wake and the downstream stator. This effect is enhanced or suppressed by controlling the R-S axial gap. In literature, the R-S axial gap (λ) can be normalized by the upstream rotor chord (C_R), the upstream rotor axial chord (C_{RX}) or the downstream stator axial chord (C_{SX}).

Several experimental and computational studies have been carried out to examine the influence of the rotary-stationary components gap on the global performance of high and low-speed compressor stages. Smith [4] carried out experimental tests on a low-speed

multistage compressor and found an efficiency increase of 1.5% - 2% and a pressure ratio increase of 4% - 6.6% as λ / C_R decreased from 0.37 to 0.08, depending on the operating point. Numerical investigations by Du *et al.* [5] have shown a significant increase in the static pressure ratio, by 85% near choke and 38% near stall, when λ / C_R was reduced from 0.17 to 0.05. A reduction of λ / C_R from 0.375 to 0.250 resulted in an increase in the efficiency by 0.7% in a two-stage low-speed axial compressor with a bowed stator [6]. On the other hand, a variation of the isentropic efficiency of 3% with no trend with respect to different axial gaps at different operating conditions was observed in a low speed 1.5 stage compressor, i.e., inlet guide vanes, rotor and stator [7].

For high-speed and transonic compressors, similar trends to the low-speed compressors have been found. A previous 3D numerical study [8] has used the second law efficiency analysis to investigate the axial gap effects. The isentropic efficiency is simply the ratio of the isentropic work to the actual work. The second law efficiency is the ratio of the net exergy to the actual work. The exergy at a state is the minimum available energy required to compress the air from the surrounding (ambient) state to the target state. The irreversibility is the difference between the actual work and net exergy. It has been shown that a reduction in the axial gap by 67% led to an increase in the second law efficiency of 0.2%-0.5%, depending on the operating condition [8]. However, it has been shown that a mid-gap ratio of $\lambda / C_R = 0.4$ gives the best efficiency among different gap ratios varying between 0.2 and 1, which means there is no obvious trend in the global performance with respect to different axial gaps in transonic compressors [2]. This seemingly random trend was observed earlier in an experimental and numerical investigation on a high-speed 1.5 stage by Saren *et al.* [9]. They showed that the circumferential indexing between the inlet guide vanes and the stator (clocking) plays an important role in the efficiency, together with the axial gap. Most of the clocking positions gave higher efficiency variations with the tight gap ($\lambda / C_{RX} = 0.23$). The clocking effects on the stage pressure ratio become more intense for a smaller gap [9].

There have been several studies of the unsteady rotor flow field with respect to different axial gaps [2, 5, 8, 9]. Saren *et al.* [9] observed an increase in the pressure fluctuations on the rotor suction surface as λ / C_{RX} was reduced from 0.66 to 0.23. The harmonics of the rotor suction surface pressure showed a different behaviour. The first and third pressure harmonics increased and the second harmonic decreased when the gap was smaller. Li and He [2] found from a numerical study that, for a mid-axial gap of $\lambda / C_R = 0.5$, a transonic compressor rotor experienced a peak vibration which is considered an unsafe condition. The rotor blade tangential force fluctuations are higher for the smallest gap ($\lambda / C_R = 0.3$) from a no flutter simulation. The irreversibility in the rotor was not sensitive to the variation of λ except at near stall at the rotor tip where the irreversibility was reduced by 3.5% as λ / C_R was reduced by 67% [8]. The rotor time-averaged lift increased by 20% when λ / C_R was reduced from 17% to 7%, due to the enhancement of the flow circulation in the rotor and stator leading edge vortices [5]. A small gap of $\lambda / C_R = 0.047$ might lead to a rotor suction surface separation [10].

The upstream component wake governs the flow pattern in this region. It has been indicated that the upstream rotor wake deficit is stronger [10] and it decays faster with a smaller axial gap size [10–12]. This can be more apparent at reduced mass flow rates [11]. The energy losses are negligible in the gap compared with the upstream and downstream components [8, 12]. The fluctuations of the unsteady pressure difference across the wake increased by 100-250 % at 20% of the span as the gap was reduced by 50%. The oscillations of the flow angle, as well as the entropy at the rotor trailing edge, also increased, by 4-10 degrees and 5%, respectively [13]. The increased fluctuations of the rotor exit flow angle with smaller gaps was also observed in [10]. The circumferential oscillations of the flow field were more significant than the axial variations within the gap region [14].

The influence of the axial gap on the stator flow field has been studied intensively since the unsteadiness and losses are more significant in the downstream component. The level of the pressure and force fluctuations on the stator blade increases when the R-S gap is smaller [10–12, 15], particularly at reduced mass flows and for the compressors with a low

rotor-stator blade count ratio. It has been shown that the time-averaged pressure distribution is not sensitive to the variation of λ , but the first harmonic of the unsteady pressure has shown higher values when $\lambda / C_{SX} = 0.3$ [12]. This can help to stabilize the flow at the stator trailing edge which can prevent the suction side boundary layer separation. The unsteadiness has been attributed to the increase in the incidence angle associated with a smaller gap, as well as high vorticity and recirculation at the stator passage. There has been no general trend of the stator flow angle with respect to the axial gap. Layachi and Bolcs [7] showed that a gap of $\lambda / C_{SX} = 0.14$ gave the highest incidence among the other smaller and larger axial gaps studied, due to the impingement of the IGV wake on the stator. That a higher incidence with a smaller gap might help to reduce the separation on the stator pressure surface was also indicated by other researchers [6, 8]. The change in the incidence angle due to the axial gap variation caused considerable variation in the stator wake position (20 - 28% of the stator pitch at stall) [7].

The aerodynamic forces on the stator blade play an important role in the investigation of its vibration levels. It has been found that a very small axial gap led to high levels of tangential and axial force fluctuations [10, 12, 15]. The general trends showed a high first force harmonic (or unsteady forces) at the smallest gap and a sudden drop (by 50 - 70%) when the gap increases. The trends have shown asymptotic behavior for larger spaces ($\lambda / C_R > 0.4$). The magnitude of the axial force was smaller than that of the tangential force and not sensitive to the axial space variation [15].

This trend in the magnitude of the forces was also observed for energy losses with respect to the axial gap [12]. Smaller gap resulted in higher losses [12], although a higher total pressure was obtained at the stator exit in another study [9]. Although the large space showed higher flow blockage at the stator exit of a transonic single stage compressor [8], the smallest space used in [7] gave the highest blockage in a stalled low speed 1.5 stage compressor. The blockage was reduced as the gap increased from $\lambda / C_{SX} = 0.092$ to 0.140 and then increased to an intermediate value as the gap increased above 0.14 [7]. A reduction of the axial gap by 67% led to an irreversibility reduction in the stator of 13.5% at choke

and 9% at the design point [8]. The stator vibration increased by 30 - 40% when reducing λ / C_R from 0.640 to 0.047.

The decay of the upstream rotor wake is affected by the axial gap. It has been shown that the wake decay in axial compressors can be attributed to viscous mixing and reversible stretching [16]. The irreversible viscous mixing wake decay occurs due to mixing between the wake velocity deficit and the freestream velocity. The reversible wake decay stretching occurs due to the diffusion of the wake flow as it travels through the stator passage. Van Zante *et al.* [16] showed that the presence of the stator passage reduced the viscous mixing of the wake by increasing the reversible stretching. They suggested that if the axial gap was reduced, the viscous mixing within the gap should be reduced since the rest of the wake decay would be carried out by reversible stretching through the stator passage. They claimed that the performance improvement due to reversible wake decay was observed by Smith [4]. Dregel and Tan [17] have shown an efficiency gain by 1% and total pressure ratio increase by 4% when reducing λ / C_R from 0.40 to 0.05 in a low speed compressor stage. This efficiency gain was only due to rotor wake mixing loss. Hill *et al.* [18] developed a simplified 2D incompressible model to calculate the decay and width of a turbulent wake in adverse pressure gradients. This model was tested by Van Zante [19] in a transonic axial compressor stage and it gave fairly good agreements with the experiments (within 10% of wake decay) at 75% span. It was found that 62% of the wake decay point the stator passage was due to the reversible stretching (wake recovery). In the absence of the stator, all of the wake decay is attributed to the viscous mixing.

From the previous experimental and numerical studies, it is evident that there is no clear trend in the effect of the rotor-stator gap on the aerodynamics and performance of axial compressors. The objective of the present work is to investigate the influence of the R-S gap of a 1.5 stage transonic axial compressor on: (1) the global performance; (2) the local losses; (3) the unsteady forces on the stator blade; and (4) the rotor wake decay due to viscous mixing and reversible stretching. The unsteady local flow field, including energy losses and forces on the blades, will be examined in detail using Unsteady Reynolds-Averaged Navier-Stokes (URANS) simulations and the time transformation (TT) approach

for the rotor-stator interface to reduce the computational cost. The rotor wake decay is examined with respect to three cases with different axial gaps and a case without the stator passage. The effect of the wake decay, wake recovery due to stretching and other sources of losses (i.e. blade, hub and shroud boundary layers) on the compressor performance is also investigated. The commercial CFD software ANSYS CFX is used for this purpose.

4.2 Numerical procedure

The compressor stage used in this work is the first stage of an aeroengine multistage transonic compressor. The stage consists of 18 inlet guide vanes (IGV), 14 rotor blades (R) and 25 stator blades (S). The details of the geometrical parameters and the operating conditions are given in Section 3.2 of Chapter 3. ANSYS CFX 16.0 [20] is used to perform the steady and unsteady Reynolds-Averaged Navier-Stokes (RANS and URANS) simulations. CFX is a finite volume, coupled, pressure-based, multigrid solver [21]. The Rhie-Chow interpolation scheme [22] is used for the pressure-velocity coupling. For all transport equations, a high-resolution advection scheme [23] that uses a non-linear blending function for each node is applied. Turbulence is accounted for using the shear stress transport model (SST) [24] since it is more suitable than the $k-\varepsilon$ model for wall-bounded flows and give better predictions for the flow separation under adverse pressure gradients. Moreover, it allows the integration of the velocity inside the viscous sublayer [20]. It switches between the $k-\omega$ model near the wall and the $k-\varepsilon$ model away from the wall through a blending function. More details on the model equations and constants can be found in Section 2.4 of Chapter 2.

The computational model used in this study is shown in Figure 4-1. Two stator blade passages are simulated in order to reduce the pitch ratio at the rotor-stator interface to be used for the unsteady simulations. A large intake is mounted upstream of the inlet guide vanes and a variable area nozzle is mounted downstream of the stator to avoid interactions between the blade rows and the effects of the boundary conditions at the inlet and outlet on the simulation results [25]. For the steady simulations, a uniform total pressure and temperature are imposed at the inlet while a constant static pressure is imposed at the outlet. Different operating conditions are obtained by using different nozzle areas. For the

unsteady cases, a constant mass flow rate is imposed at the outlet of the nozzle for comparison between different axial gap settings at two operating points. All blades, hubs and casings are set as no-slip adiabatic walls. The steady simulations are used to initialize the unsteady simulations at a high efficiency point (HE) and a reduced mass flow point or peak pressure ratio point (PPR).

For the steady simulations, the mixing plane approach (MP) is applied at the IGV-rotor and rotor-stator interfaces [26]. A circumferential averaging of the flow quantities is performed at the interface while meridional profiles are conserved between the stationary and rotary components. For the unsteady simulations, two approaches have been applied. The profile transformation (PT) [27] is used at the inlet guide vane-rotor (IGV-R) interface and time transformation (TT) [28] for the R-S interface. For the profile transformation method, an instantaneous periodicity is applied at the periodic boundaries and the fluxes are scaled at the IGV-R interface to account for the pitch change. The time transformation method provides an improvement over the profile transformation by transforming the equations in time such that the instantaneous periodicity is applied without any approximation [29]. For the TT method, two stator blades are modeled to reduce the pitch ratio from 1.8 to 1.1 as recommended by Giles [28].

The grid and time independence studies have been carried out for the medium R-S gap in Section 3.3 of Chapter 3. The differences between the mesh used in the study and the finest mesh are less than 1% in terms of the mean flow quantities and less than 5% in terms of the turbulence quantities. The time step size used shows a discrepancy of less than 0.5% in static pressure when reduced by a factor of 2. The three axial spacing configurations used in the study are shown in Figure 4-1. The spacing is normalized by the rotor hub chord since the closest axial distance between the rotor and the stator is located at the hub section. The values of the R-S gaps are $(\lambda / C_R)_{Hub} = 4.8\%$, 9.6% and 19% . Since the spacing varies along the spanwise direction, the gaps are referred to as small, medium and large, respectively. The medium axial gap corresponds to the baseline design while the small and large gaps are obtained by reducing and increasing the medium gap by a factor of 2, respectively. The details of the node count for each configuration are listed in

Table 4-1. The distribution of the nodes across the interface is kept as consistent as possible in all directions to avoid numerical errors due to interpolation. The number of time steps per rotor blade pass period is 100 and 10 inner loop iterations per time step were used to achieve RMS residuals of the order of 10^{-6} for all equations. In the following sections, the effect of the R-S gap on the global and local performance of the axial stage is examined.

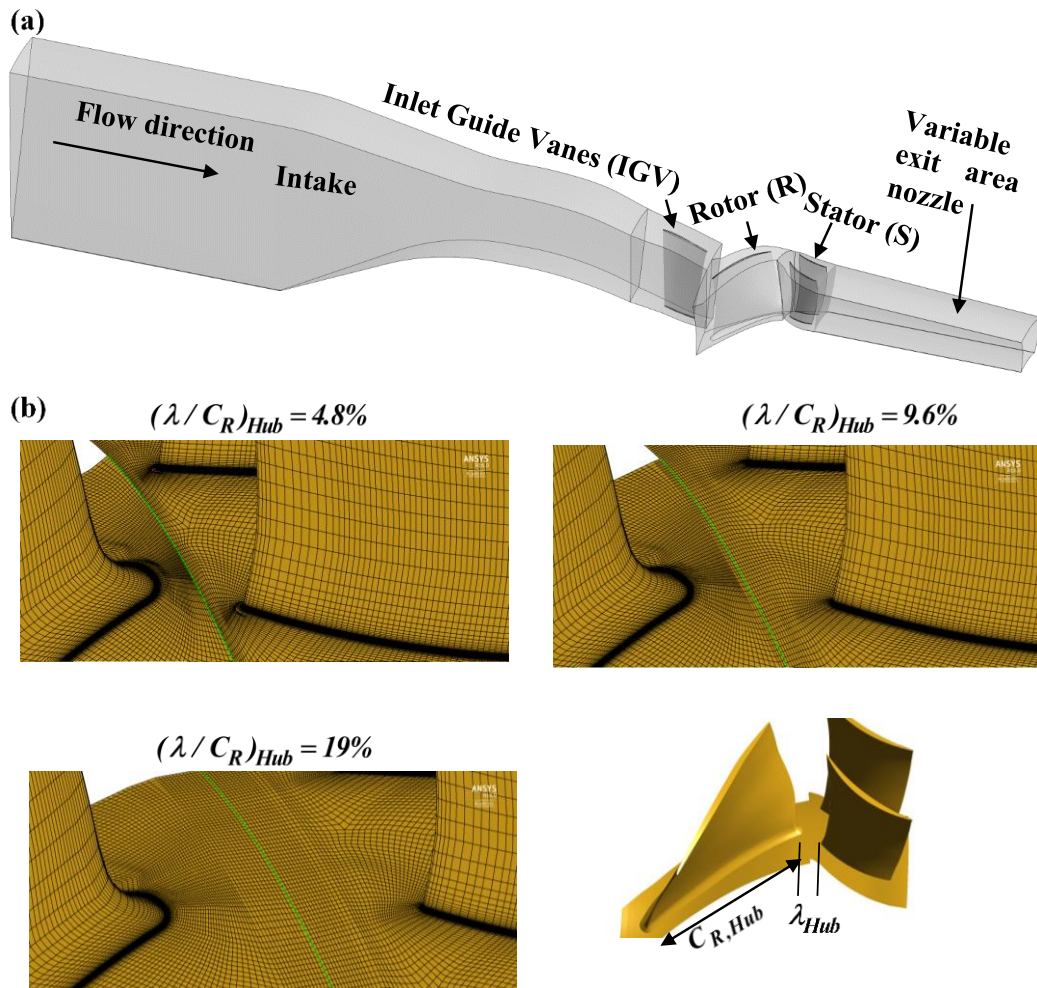


Figure 4-1 The computational domain of the axial compressor stage; (a) intake section, inlet guide vane (IGV), rotor (R), stator (S) and variable exit nozzle, (b) a close-up view of the mesh at the hub section for the three R-S axial gaps used. The axial spacing is normalized by the rotor chord at the hub section. The highlighted line represents the location of the rotor-stator interface.

Table 4-1 Mesh data for each component for different R-S spacing configurations

| Component R-S gap | Intake | IGV | R | S | Nozzle |
|------------------------------------|---------------|------------|----------|----------|---------------|
| Small | 533,286 | 1.51 M | 2.51 M | 1.26 M | 500,094 |
| Medium | 533,286 | 1.51 M | 2.54 M | 1.30 M | 500,094 |
| Large | 533,286 | 1.51 M | 2.62 M | 1.34 M | 500,094 |

4.3 Effect of the axial gap on the global and local performance

The normalized total pressure ratio (PR) and the total-to-total efficiency (η_{tt}) are plotted against the normalized mass flow rate from both steady and unsteady simulations at different R-S gaps in Figure 4-2. The steady simulations show no significant differences at different R-S gaps in both η_{tt} and PR due to the mixing of the wake implemented in the MP approach across the rotor-stator interface. The time-averaged PR and η_{tt} are shown at two selected points, a high efficiency point (HE) and a peak pressure ratio point (PPR). The mass flow rate is normalized by the mass flow rate corresponding to the HE point for the medium R-S gap. The discrepancies between the TT and MP predictions are attributed to the local differences in the local flow field at the IGV-R interface as previously discussed in Section 3.9 of Chapter 3. At the HE point, the medium gap shows the highest efficiency with an improvement by 0.2% over the small gap and 0.3% over the large gap. However, at the PPR point, the large gap shows the highest efficiency with an improvement by up to 1.6%. A higher PR is obtained with the larger gap at both operating points.

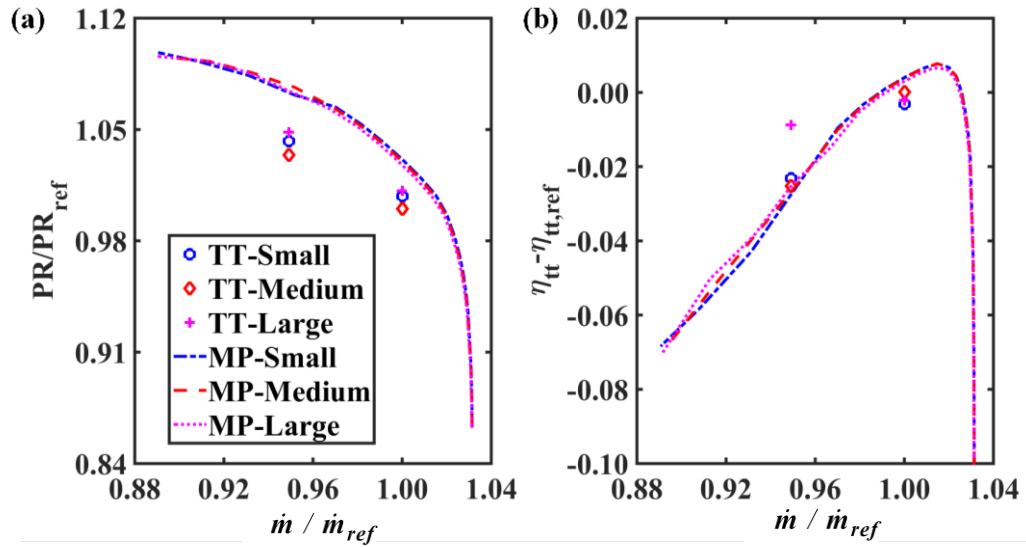


Figure 4-2 Global performance of the compressor; (a) total pressure ratio and (b) total-to-total efficiency from steady (MP) and unsteady (TT) simulations

The variation of the efficiency with the axial gap is shown in Figure 4-3 for the CFD predictions of the global and local efficiency (at each spanwise section) as well as the predictions from the previous literature [2, 4, 6, 7]. For the CFD global efficiency, the axial gap is based on the midspan. At the HE point, a good agreement in efficiency trends is observed between the present CFD predictions and numerical simulations on a transonic stage by Li and He [2]. Most of the efficiency benefit for the medium gap at the HE point is achieved at $\zeta = 0.75$. At the PPR point, the largest gap has the highest efficiency at all spanwise sections except for the near hub section ($\zeta = 0.01$). There is no trend observed in Layachi and Bolcs experimental work on a low-speed stage [7]. Both low speed stages tested experimentally by Smith [4] and Lu *et al.* [6] have shown similar trends in terms of efficiency penalties with larger axial gaps at all operating points. This suggests that the performance of the low speed compressors is significantly improved by the reduction of the axial gap. However, for the high-speed compressors, the size of the axial gap is more critical and dependent on the operating condition.

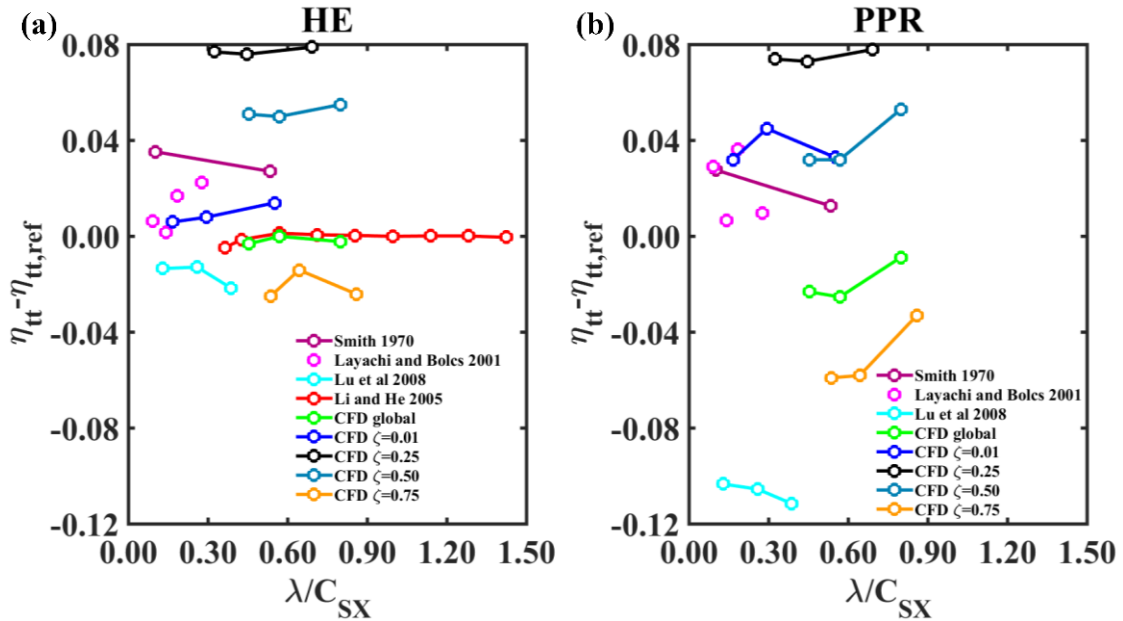


Figure 4-3 The variation of the total efficiency with axial gap from the literature and present CFD work at (a) the HE point and (b) PPR point

The total pressure loss coefficient is another measure of the performance of the compressor. It is the ratio of the total pressure drop along a path and the dynamic pressure at the inlet of the path. The total pressure loss coefficient, ω_l , is given as follows:

$$\omega_l = \frac{\overline{P_{T,in}}^m - \overline{P_{T,ex}}^m}{\overline{P_{T,in}}^m - \overline{P_{in}}^a} \quad (4-1)$$

where P_T and P are the total and static pressure, respectively. The operators, $(\overline{\quad})^m$ and $(\overline{\quad})^a$ are the mass and area-weighted averages of the quantity at the plane of interest. The global loss coefficient is calculated along the gap, the stator passage, and the gap and stator passage combined. The inlet (reference) pressure is taken at the rotor trailing edge (RTE) when calculating for the gap, and gap and stator combined while it is taken at the stator leading edge (SLE) when calculating for the stator. Figure 4-4 shows the total loss coefficient for the three regions at the HE and PPR points. The losses in the gap show insignificant increase as the gap increases at the HE point. However, at the PPR point, the

medium gap has the highest gap loss coefficient as shown in Figure 4-4(a, b). For the stator passage, the largest gap has slightly less losses than the other gaps by up to 6% at the HE point. The differences become more significant as the mass flow rate is reduced as shown in Figure 4-4(c, d). The losses associated with the large gap are less than those associated with the medium and small gaps by 22% and 27%, respectively. This trend was also observed by Yu and Lakshminarayana [12]. For the combined gap-stator losses at the HE point, the medium gap shows slightly higher losses as shown in Figure 4-4(e). For the PPR point (Figure 4-4(f)), the largest gap has less losses, by up to 19%, which explains the higher PR in shown Figure 4-2(a).

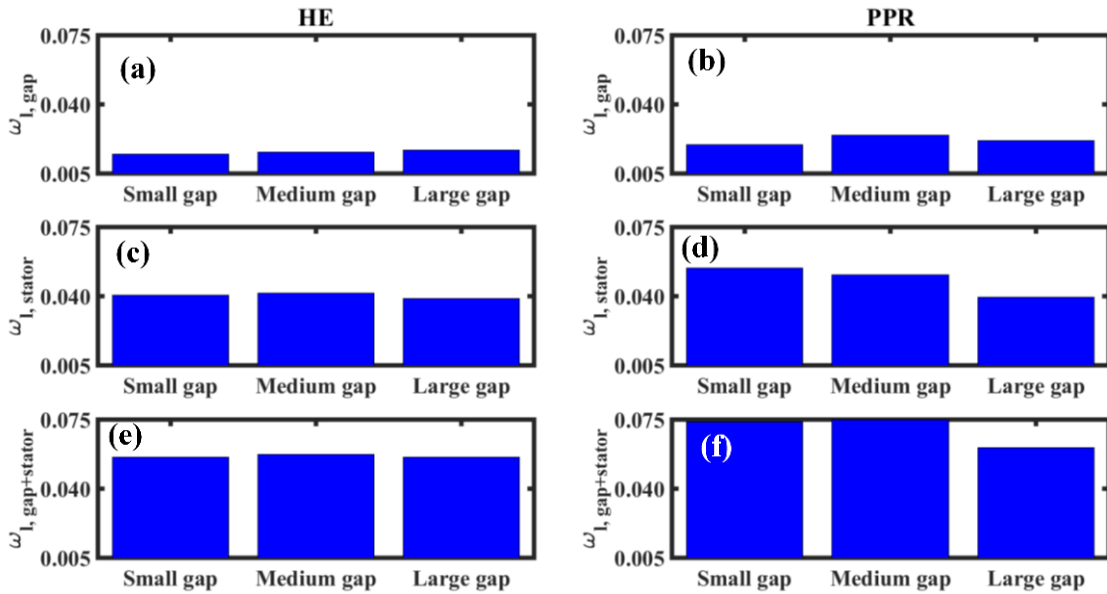


Figure 4-4 Global total pressure loss coefficient for (a,b) the gap, (c,d) the stator and (e,f) the gap and stator combined. The left and right column figures are calculated at the HE and PPR points, respectively.

The local losses at each spanwise section are calculated by taking the length average of the pressures at each streamwise location. The local total pressure loss coefficient is calculated by,

$$\omega_l(x) = \frac{\overline{P_{T,in}}^l - \overline{P_T(x)}^l}{\overline{P_{T,in}}^l - \overline{P_{in}}^l} \quad (4-2)$$

where the operator, $(\bar{\quad})^l$ is the length average of the quantity at the line. The inlet (reference) positions are considered in the same manner as for Equation 4-1. The time-averaged loss coefficients for the gap, the stator, and the gap and stator combined are shown in Figure 4-5 at the midspan section ($\zeta = 0.5$). The loss coefficients at other sections ($\zeta = 0.01, 0.25, 0.75, 0.99$) are shown in Figure A-4 to Figure A-7 of Appendix A. It is clear that the largest gap has the lowest total pressure loss coefficient among different gaps. Within the gap, when the flow reaches the SLE, the pressure loss coefficients are almost the same for all gaps as shown in Figure 4-5(a, b). The progression of the losses is faster for smaller gaps due to the increased mixing between the low velocity wake flow and the high velocity freestream flow. The smallest gap continues to exhibit more loss through the stator passage for the PPR condition as shown in Figure 4-5(d). The effect of the axial gap is insignificant at the midspan for the HE point. The largest gap has the smallest loss at the stator trailing edge (STE) at the lower 50% span and highest losses at the upper 50% span at the HE point.

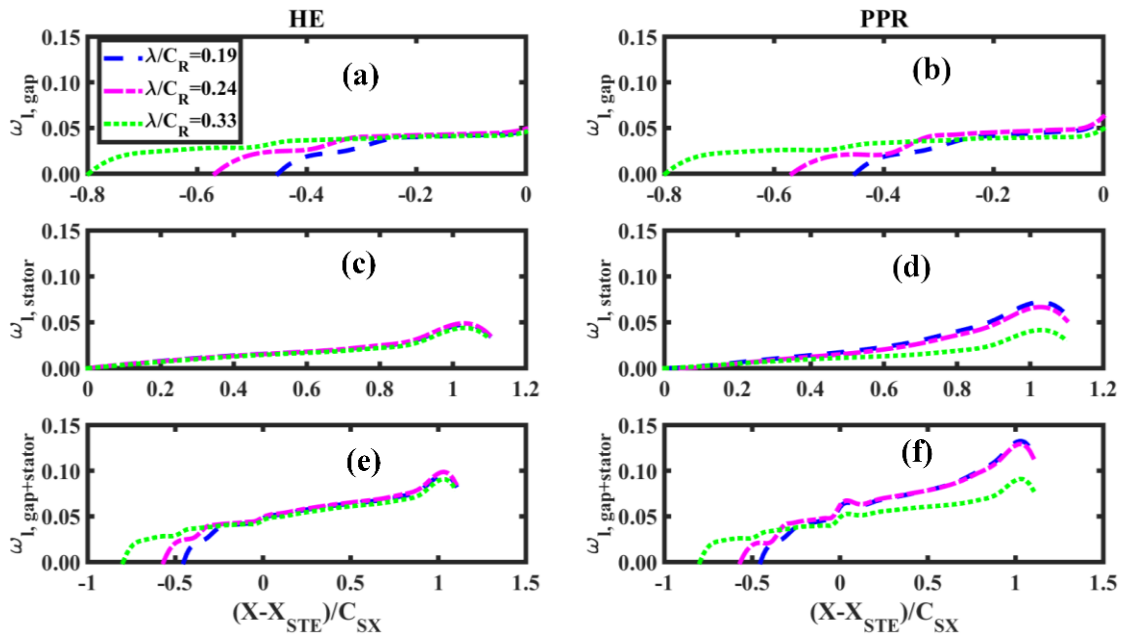


Figure 4-5 Total pressure loss coefficient at 50% spanwise section for (a,b) the gap, (c,d) the stator and (e,f) the gap and stator combined. The left and right column figures are calculated at the HE and PPR points, respectively.

The total pressure loss coefficient at the STE is plotted against the axial gap at different sections for the HE point in Figure 4-6. The CFD predictions are obtained at $\zeta = 0.25, 0.50$ and 0.75 and compared with 2D simulations from Yu and Lakshminarayana on a low speed compressor at the midspan section [12]. The same trend of the pressure loss reduction for the larger gap is observed when comparing the results from the literature and present study at $\zeta = 0.25$ and 0.50 . Yu and Lakshminarayana showed that reducing λ/C_{SX} from 0.8 to 0.3 increased the pressure loss by 7% while the current study shows an increase in the losses by 5.5% when λ/C_{SX} is reduced from 0.8 to 0.45 . However, at $\zeta = 0.75$, the pressure loss coefficient increases with the gap which explains the local efficiency penalty for the largest gap in Figure 4-3(a).

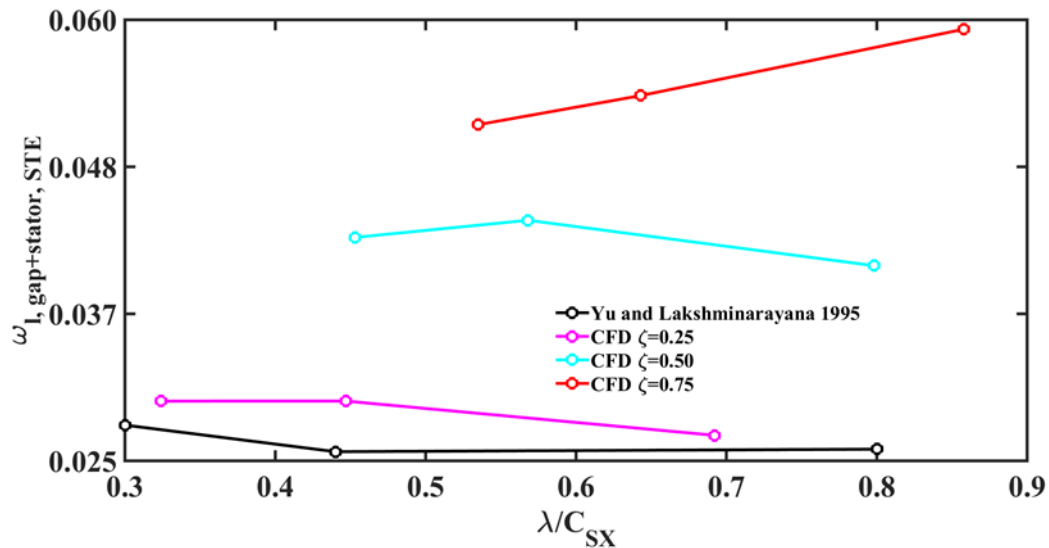


Figure 4-6 The variation of the total pressure loss coefficients at the STE with R-S axial gap. The results are obtained from the present CFD predictions at $\zeta = 0.25, 0.50$ and 0.75 as well as Yu and Lakshminarayana [12].

4.4 Effect on the stator forces

The aerodynamic forces on blades have an important impact on the lifespan of the blades. The effect of the axial gap on the unsteady streamwise (F_{ξ}) and tangential (F_{θ}) forces on the stator blade is examined both globally and locally at 5 spanwise locations, 1%, 25%, 50%, 75% and 99%. The time-averaged forces are not very sensitive to the gap, as shown in Figure A-8 of Appendix A. The forces for the medium gap are slightly smaller than those for the other gaps at the HE point. The same trend is observed for the local forces at each spanwise section, as shown in Figure A-11 of Appendix A. For each group of bars, each bar represents the force at a spanwise section. From left to right, the span increases from 1% to 99%. The time-averaged forces increase with span due to the higher static pressure coefficient. The first and second harmonics of the force represent the unsteady effects due to wakes and pressure fluctuations. For the HE point at the midspan, the decay of the wake is responsible for the reduction of the forces on the stator, as shown in Figure 4-7(a, c). The higher forces near the hub (1% span) for the large gap is due to the higher flow incidence angle which results in the increase in the pressure on the stator pressure surface. The flow in the tip region (99% span) is dominated by the tip leakage vortex. The strength of the vortex is higher for the large gap which leads to higher unsteady forces on the blade. For the PPR point, the upper span region (75%-99%) shows significant variations of forces with respect to the axial gap as depicted in Figure 4-7(b, d). The large gap has 4 times less force than the other gaps. The suction surface separation bubble near the STE for the smaller gaps grows, such that it forms a focus on the suction surface as shown in Figure 4-8(a, b). The spiral vortex formed by this focus increases the unsteadiness of the forces at this region which explains the high levels of the first harmonic of force components. The second harmonic of the forces has no significant trend as shown in Figure A-10 and Figure A-12 of Appendix A.

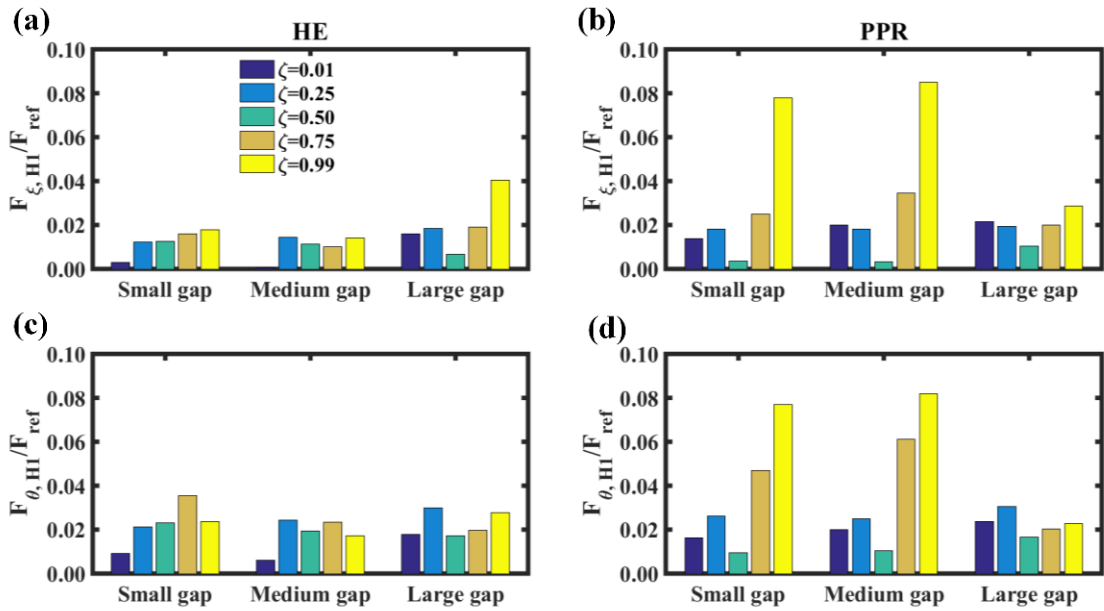


Figure 4-7 The first Fourier harmonic of the streamwise component (a,b) and tangential component (c,d) of the forces on the stator blade at spanwise locations of 1%, 25%, 50%, 75% and 99%. The left and right column figures are calculated at the HE and PPR points, respectively.

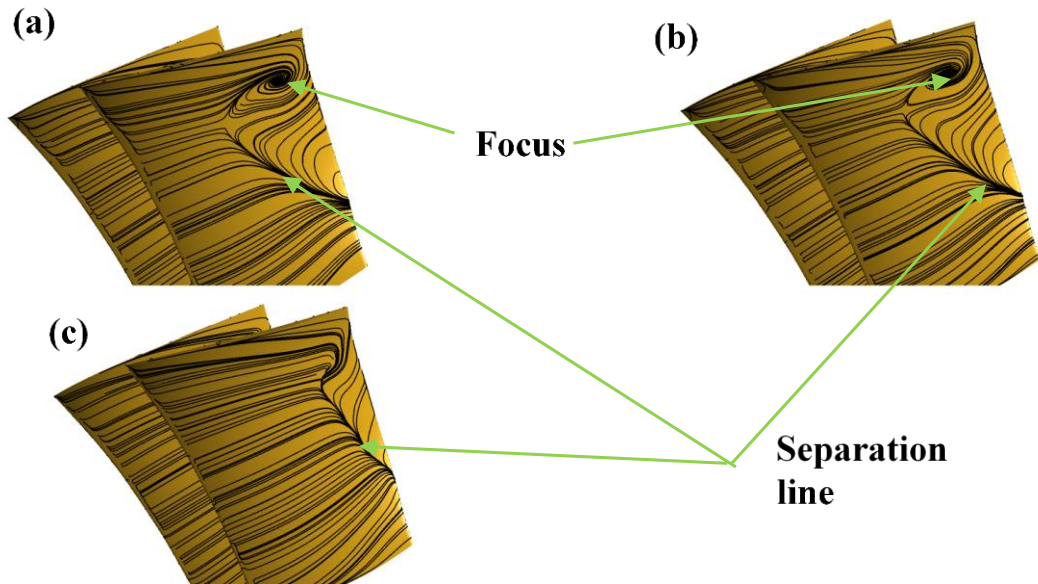


Figure 4-8 Surface streamlines of the average velocity on the stator blade suction surface for (a) small gap, (b) medium gap and (c) large gap at the PPR point

The results from the literature [10, 12] and present CFD predictions for the first harmonic of the stator forces are shown in Figure 4-9 for different λ/C_{SX} values. The forces are normalized by arbitrary values to rescale the plot. The CFD predictions show a similar trend to that predicted in the literature at $\zeta = 0.5$. This is due to the fact that the numerical results by Yu and Lakshminarayana [12] are based on the midspan section. The current compressor shows a reduction in the stator first harmonic forces by up to 47% while the literature shows a reduction by 26% when λ/C_{SX} is increased from 0.45 to 0.80. The sensitivity of the forces is more significant in the current compressor due to its relatively high speed.

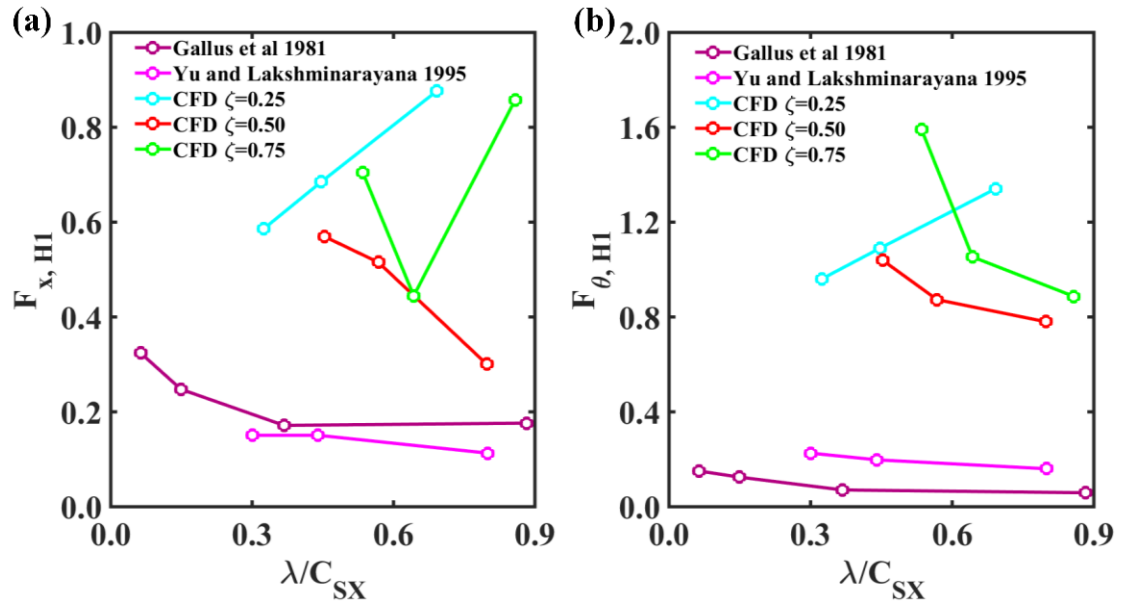


Figure 4-9 The variation of the first Fourier harmonics of the (a) axial and (b) tangential forces on the stator blade with R-S axial gap. The results are obtained from the CFD predictions at $\zeta = 0.25, 0.50$ and 0.75 , Gallus *et al.* [10] and Yu and Lakshminarayana [12].

4.5 Effect on rotor wake decay

Rotor wakes are one of the sources of energy loss in compressors. The rotor wake mixing is responsible for 33% of the total loss in a cascade as stated by Denton [30]. The velocity deficit due to the mixing of the upstream suction and pressure surfaces boundary layers

mixes with the main (freestream) velocity causing a mixing loss. However, as the wake undergoes a diffusion process or adverse pressure gradients, the velocity deficit is recovered as illustrated in Figure 4-10. If a simple 2D flow over an obstacle is considered, as shown in Figure 4-10(a), the downstream momentum deficit mixes with the freestream momentum. The freestream momentum is purely due to viscous mixing. However, for the wake flows in a diffuser, the wake decay involves viscous mixing as well as reversible stretching as shown in Figure 4-10(b). This mechanism is referred to as wake recovery [31]. Hill *et al.* [18] developed a 2D incompressible model to predict the decay of a wake propagating in a flow with adverse pressure gradients. The model only includes the freestream velocity and momentum thickness at an initial location. This model gave a fairly good agreement with the laser anemometer measurements in a transonic compressor stage by Van Zante *et al.* [16]. The details of the derivation are given in [16, 18]. The relative wake depth is given by

$$\frac{D_W}{D_{W,in}} = \left(\frac{U_{in}}{U} \right)^2 \left[1 + \frac{8\pi^2}{\pi^2 - 4} \int_{x_{in}}^x \frac{\mu_t D_{W,in}^2}{\rho U (\delta^{**})^2} \left(\frac{U_{in}}{U} \right)^4 dx \right]^{-0.5} \quad (4-3)$$

where D_W is the wake depth which is given by

$$D_W = \frac{U - U_{min}}{U} \quad (4-4)$$

where U is the freestream velocity and U_{min} is the minimum wake velocity as shown in Figure 4-11. The freestream velocity is assumed to be the mean of the edge velocities, U_{e1} and U_{e2} . The wake exhibits relatively higher entropy values when compared to the freestream flow. The static entropy profile is used to determine the wake edges by selecting the points of relatively low values at the edges of the wake. The subscript *in* stands for the inlet condition, which can be located at the stator leading edge or the rotor trailing edge. To include the effect of compressibility, the equation is modified such that the velocity U is replaced by the relative momentum flux ρW , where W is the velocity in the rotor relative

frame. Although, in previous studies, the eddy viscosity to momentum thickness ratio,

$\frac{\mu_t}{\rho U \delta^{**}}$, was assumed to be constant with a value of 0.044 [16, 18], the variation of this

ratio in the x direction is considered in the present study. The freestream velocity profile

$\frac{U_{in}}{U}$ is estimated by assuming the following linear relation [16],

$$\frac{U_{in}}{U_{ex}} = \frac{L_{w,in}}{L_{w,ex}} \quad (4-5)$$

where $L_{w,in}$ and $L_{w,ex}$ are the wake lengths at the inlet and outlet of the domain of interest.

The second term in Equation 4-3 is integrated from the inlet along the axial direction to the point where the wake depth is needed.

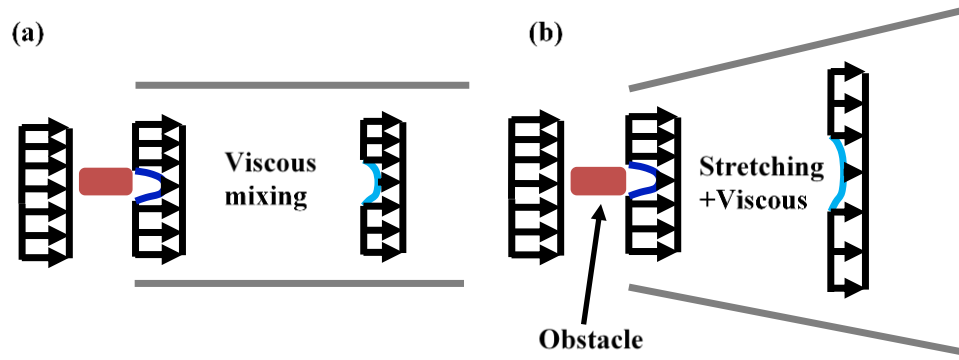


Figure 4-10 Illustration of wake decay mechanisms due to (a) viscous mixing and (b) viscous mixing and stretching

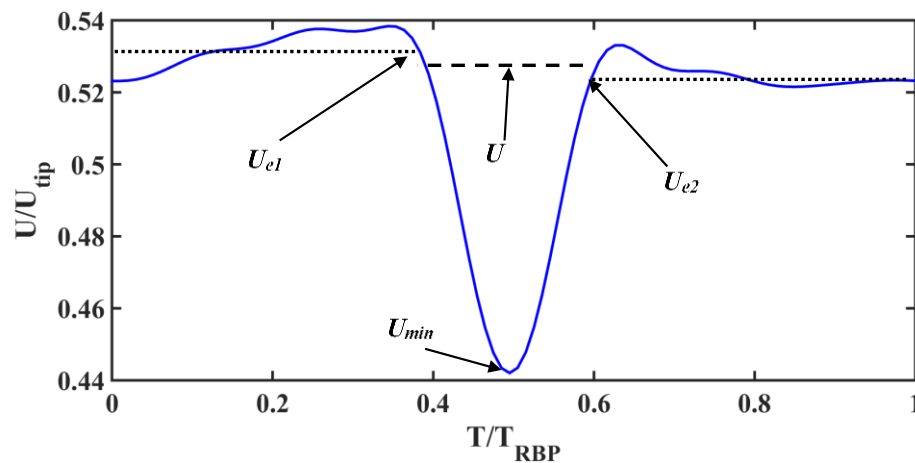


Figure 4-11 The wake profile at a midpitch line against normalized time. The time is normalized by the rotor blade passing period and the velocity is normalized by the rotor tip speed.

The relative wake depth is plotted along the midpitch line of the stator in Figure 4-12 for different axial gap configurations and for a case without the stator. The CFD predictions of the wake decay show a fairly good agreement with the experimental results by Van Zante *et al.* on NASA Rotor 35 and Stator 37 [16] and the decay model given by Equation 4-3. For the HE point, all axial gap configurations show the same trend of wake decay. The discrepancies between the CFD predictions, experiments and model are within 10% of the wake decay. For the PPR point, the small axial gap configuration shows slightly higher wake decay than the large gap by approximately 5% for both the CFD predictions and decay model by Equation 4-3. The wake decay model overestimates the decay by up to 15% possibly due to the errors associated with the wake length determination. The rate of the wake depth reduction is higher for all stator cases than the case without the stator (case N CFD). The same trend was observed by Yu and Lakshminaryana [12]. They showed there was no difference in the wake decay with different axial R-S gaps and a slower decay with the no stator case. Since the wake decay in the no stator case is only due to the viscous mixing, the presence of the downstream stator is responsible for the stretching mechanism of the wake decay.

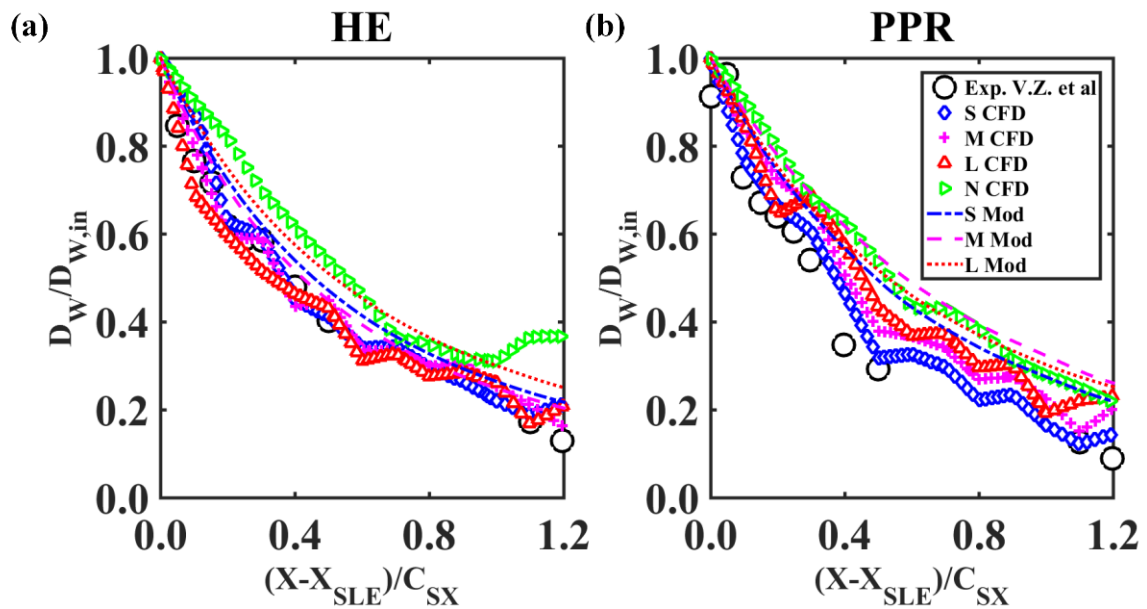


Figure 4-12 The wake decay along the midpitch of the stator passage at (a) HE and (b) PPR. The CFD data are plotted for small (S), medium (M), large (L) axial gaps and without the stator (N). The experimental data are obtained from [16] for a NASA 37 stator and the model (Mod) plots are obtained from Equation 4-3.

Figure 4-13 shows the contribution of the viscous mixing and reversible stretching to the wake decay. The viscous mixing part is calculated by setting the freestream velocity ratio equal to 1 in Equation 4-3 while the stretching part is obtained by setting the eddy viscosity equal to zero. For the HE point, the model shows a stronger total decay with the small R-S gap. Most of the decay is due to the reversible stretching for all axial gaps. The ratio of the viscous mixing to stretching contribution is almost the same for both axial gaps at HE point. However for the PPR point, the small gap configuration shows a higher viscous decay than that of the large gap by 10% at the stator trailing edge. The initial wake depth, $D_{W, in}$, is deeper for the small gap which leads to a higher viscous effects as shown in Equation 4-3. To examine the wake decay within the axial gap, the CFD predictions of the wake decay are also depicted in Figure 4-14 using the RTE as the initial location for all axial gaps, along with the case without the stator. As expected, the wake decay is faster as the stator moves closer to the rotor. The high levels of unsteadiness due to rotor wake-stator interactions enhance the rotor wake decay.

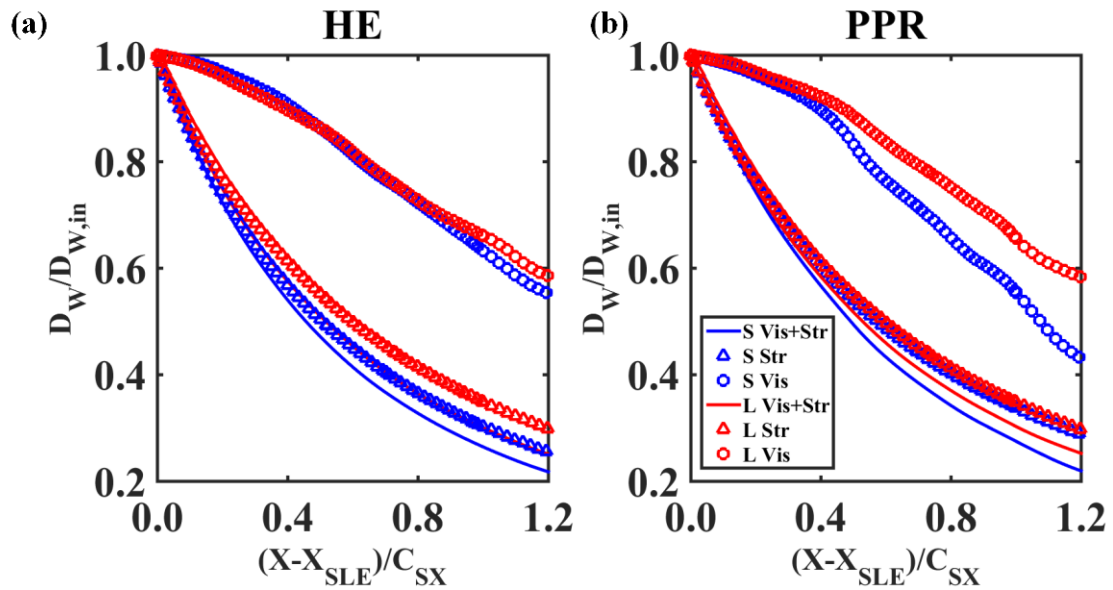


Figure 4-13 Wake decay model predictions due to total decay (lines), inviscid stretching (triangular markers) and viscous mixing (circular markers) for small and large axial gaps at (a) HE and (b) PPR

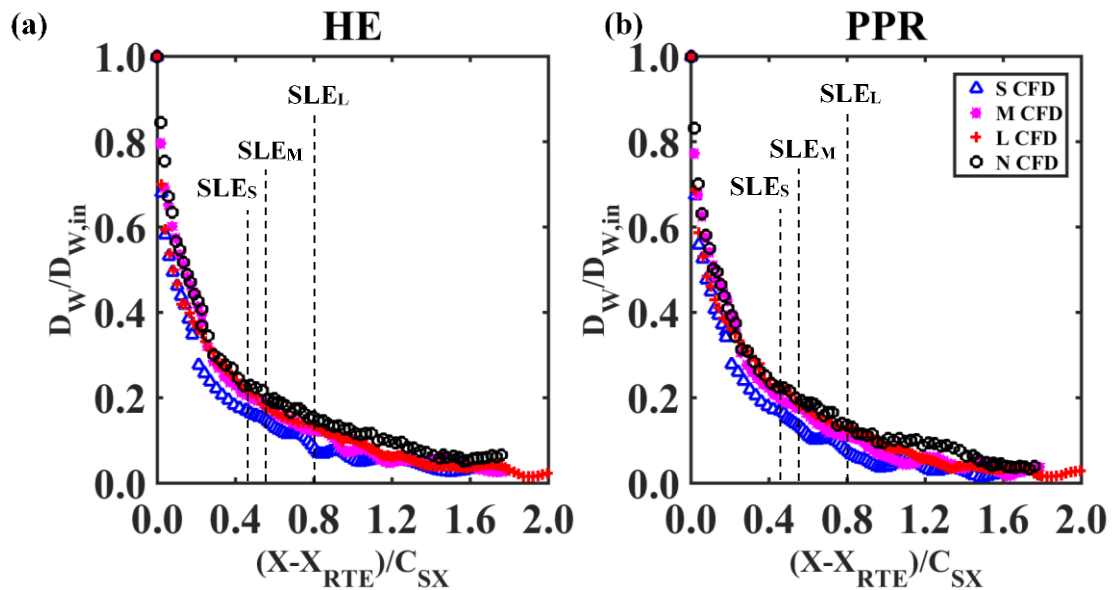


Figure 4-14 Wake decay CFD predictions using the rotor trailing edge profile as the initial condition at (a) HE and (b) PPR. The locations of the stator trailing edge are illustrated for each axial gap configuration.

4.6 Recovery of the rotor wake

The wake recovery is defined as the contribution of inviscid stretching to the decay of the wake [19, 31]. Van Zante [19] used a time and space decomposition for the energy equation to derive the disturbance kinetic energy which measures the rate of the wake recovery or the reduction in mixing loss. In this study, the URANS equations is used to solve the transport equations, therefore, the mixing loss reduction is obtained at the stator midpitch by taking the time-average of the viscous dissipation of energy. By neglecting the thermal conduction term, the 1D time-averaged energy equation can be written as follows:

$$\rho u \frac{\partial (u^2 / 2)}{\partial x} + u \frac{\partial P}{\partial x} = u \frac{\partial \tau}{\partial x} \quad (4-6)$$

where u is the velocity in the x direction and $u \frac{\partial \tau}{\partial x}$ is the viscous dissipation of energy.

Integrating both sides with respect to x yields,

$$\Delta(uP_T) = \Delta\varphi_{vs} \quad (4-7)$$

where P_T is the total pressure and φ_{vs} is the shear work due to viscous dissipation. To consider the 3D flow nature, the absolute velocity magnitude is used instead of u . The rate of mixing reduction at the stator midpitch is a measure of the reversible wake recovery. The recovery, R , is given by the difference between the inlet and local dissipation loss as follows:

$$R = \frac{\varphi_{vs,in} - \varphi_{vs}(x)}{\varphi_{vs,in}} \quad (4-8)$$

where $\varphi_{vs,in}$ is the viscous dissipation at the inlet plane (RTE) and $\varphi_{vs}(x)$ is the viscous dissipation at any axial location. Figure 4-15 shows the wake recovery from the rotor inlet to the stator exit. It is obvious that the case without the stator has an increase in the viscous dissipation which gives negative recovery values. For the HE point, the small spacing gives the highest recovery with a difference of 3% at the STE. The wake decay within the gap

has no reversible contribution which gives a reduction in the recovery. For the PPR point, the recovery at the STE is higher than that of HE point by about 3% for all the cases. A maximum recovery of 30% is obtained by the small R-S gap at the PPR point. Although the reversible recovery is higher for the PPR compared with the HE, the wake decay model shows the opposite in Figure 4-13 which suggests that the decay model overestimates the viscous decay for reduced mass flow operating points. Overall, the benefits of reducing the R-S gap in terms of wake recovery are negligible compared with other sources of losses such as the stator boundary layer separation.

To examine the sources of losses in the stator passage, the midspan section is considered to exclude the hub and shroud boundary layer effects. Figure 4-16 shows the total, wake and secondary losses at the stator midspan for both HE and PPR points. The total losses are calculated from total pressure loss coefficient (Equation 4-2). The wake losses are the pressure loss along the midpitch line. The secondary losses are the ratio of the crossflow kinetic energy to the freestream flow kinetic energy. The crossflow is the velocity component normal to the freestream direction. The secondary losses are negligible (up to 3% of the total losses) compared with the other sources. For the HE point, the wake losses behaviour along the stator confirms that the small gap has a better wake recovery than the large gap at the stator trailing edge. The wake losses for both gap configurations are between 10-11% of the total losses. For the PPR point, the wake losses for the small gap increase to 18% of the total losses compared with only 1% for the large gap. This confirms the higher values of viscous mixing associated with the small gap configuration as predicted by the model. The losses due to the stator blade boundary layers can be estimated by obtaining the difference between the total and wake losses. For the HE point, the sensitivity of the boundary layer losses to the axial gap variation is insignificant. However for the PPR point, reducing the axial gap leads to higher boundary layer losses by 42%.

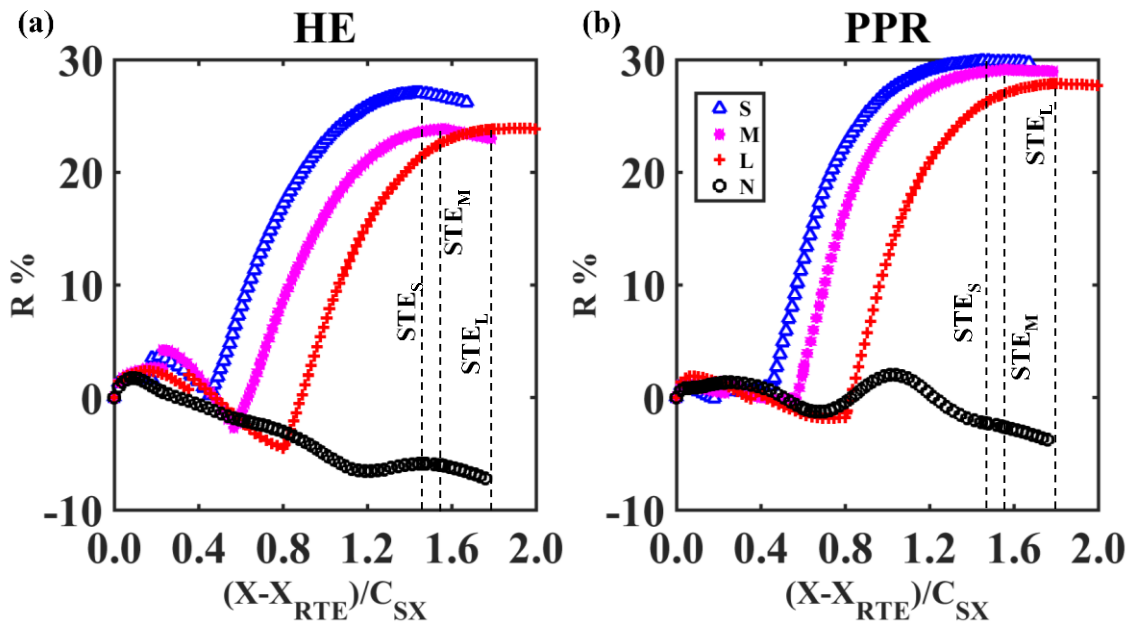


Figure 4-15 Reversible wake recovery across the gap and the stator passage for small (S), medium (M), large (L) and no stator (N) at (a) HE and (b) PPR points

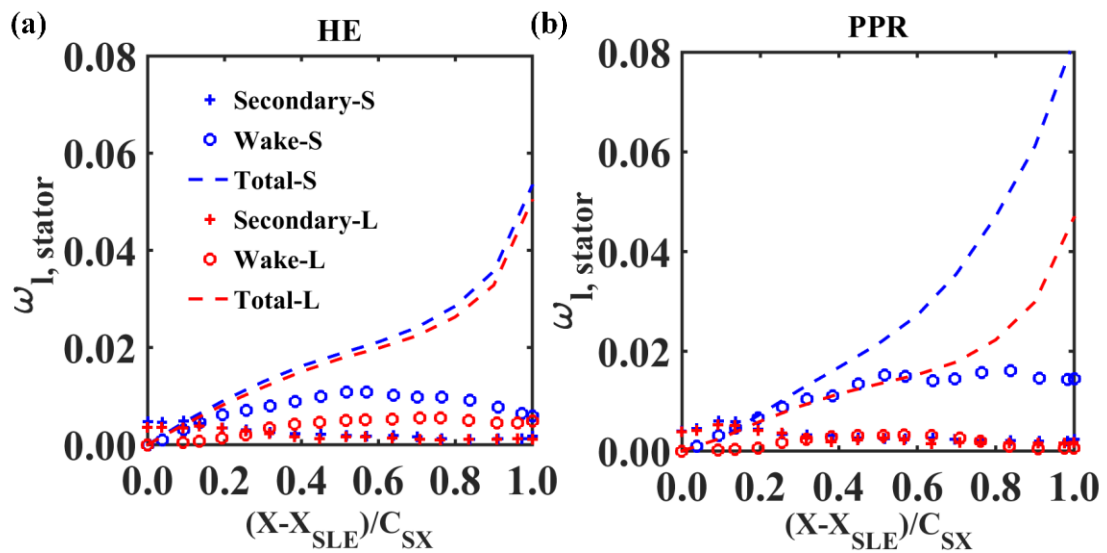


Figure 4-16 Sources of losses in the stator passage at the midspan section for (a) HE and (b) PPR points

4.7 Conclusions

The effect of the axial gap between the rotor and stator of a transonic compressor is examined using 3D unsteady numerical simulations in terms of global and local performance. The previous experimental and numerical predictions of the efficiency show different trends. At the high efficiency point (HE), the medium gap ($\lambda/C_{SX} = 0.57$) gives the best efficiency which agrees with a previous numerical study on a different transonic stage. For the peak pressure ratio point (PPR), the largest gap exhibits the best efficiency. An efficiency penalty of 1.6% is observed when the gap is reduced by 40%. Most of the total pressure losses in the small gap configuration are located in the stator passage due to the separation of the suction surface boundary layer. A 5.5% increase in the total pressure loss coefficient is observed when λ/C_{SX} is reduced from 0.8 to 0.45. The local unsteady forces on the stator blade increase by a factor of 4 near the tip as the rotor-stator gap is reduced due to the large separation bubbles at the PPR point. However at the HE point, the largest gap gives the highest unsteady stator forces. The differences in the time-averaged forces with respect to the axial gap are insignificant. At the midspan section, the first harmonics of the stator forces show a reduction by 47% as λ/C_{SX} is increased from 0.45 to 0.80. The rotor wake decay has a good agreement with a 2D simple model as well as experimental observations in a different transonic stage. The 2D wake decay model is used to examine the effect of axial gap on the rotor wake decay due to viscous mixing and reversible stretching. Although the wake decay model shows that the viscous contribution is higher for the small gap configuration at the reduced mass flow point, the recovery calculations based on the viscous dissipation show the opposite. This can be attributed to the deeper wake at the inlet of the stator in the case of the smallest gap which increases the magnitude of the viscous term in the model. A case without the downstream stator shows that the total rotor wake decay is slower than for the other cases. The regions free of blades, such as the R-S gap and downstream the rotor for no stator case, involve only wake decay due to the viscous mixing. For the smallest axial gap case, the efficiency gain from the reversible wake decay is insignificant when compared with the boundary layer losses.

4.8 References

- [1] R. Biollo and E. Benini, “Recent advances in transonic axial compressor aerodynamics,” *Prog. Aerosp. Sci.*, vol. 56, no. 1, pp. 1–18, 2013.
- [2] H. D. Li and L. He, “Toward intra-row gap optimization for one and half stage transonic compressor,” *ASME J. Turbomach.*, vol. 127, no. 3, pp. 589–598, 2005.
- [3] H. Dawson and J. D. Voce, “The effect of axial spacing on compressor tone noise,” in *Proc. 5e Congr Int d’Acoustique*, Liège, Belgium, 1965.
- [4] L. H. Smith, “Casing boundary layers in multistage axial-flow compressors,” in *Flow Research on Blading*, L. S. Dzung, ed., Elsevier, Amsterdam, The Netherlands, 1970.
- [5] L. Du, X. Sun, and V. Yang, “Generation of vortex lift through reduction of rotor/stator gap in turbomachinery,” *AIAA J. Propuls. Power*, vol. 32, no. 2, pp. 472–485, 2015.
- [6] H. Lu, F. Chen, J. Wan, and Z. Wang, “Flow field improvement by bowed stator stages in a compressor with different axial gaps under near stall condition,” *Chinese J. Aeronaut.*, vol. 21, no. 3, pp. 215–222, 2008.
- [7] M. Y. Layachi and A. Bolcs, “Effect of the axial spacing between rotor and stator with regard to the indexing in an axial compressor,” in *Proc. ASME Turbo Expo*, New Orleans, Louisiana, USA, 2001.
- [8] W. Li, Y. Sun, Y.-X. Ren, S. Fu, and A. R. Wadia, “The influence of rotor-stator spacing on the loss in one-stage transonic compressor,” in *Proc. ASME Turbo Expo*, Orlando, Florida, USA, 2009.
- [9] V. E. Saren, N. M. Savin, D. J. Dorney, and D. L. Sondak, “Experimental and numerical investigation of airfoil clocking and inter-blade-row gap effects on axial compressor performance,” in *Proc. 34th AIAA/ASME/SAE/ASEE Joint Propulsion*

Conference and Exhibit, Moscow, Russia, 1998.

- [10] H. E. Gallus, H. Grollius, and J. Lambertz, "The influence of blade number ratio and blade row spacing on axial-flow compressor stator blade dynamic load and stage sound pressure level," *ASME J. Eng. Power*, vol. 104, no. 3, pp. 633–641, 1982.
- [11] S. Fleeter, R. L. Jay, and W. A. Bennett, "Wake induced time-variant aerodynamics including rotor-stator axial spacing effects," *ASME J. Fluids Eng.*, vol. 103, no. 1, pp. 59–66, 1981.
- [12] W.-S. Yu and B. Lakshminarayana, "Numerical simulation of the effects of rotor-stator spacing and wake / blade count ratio on turbomachinery unsteady flows," *ASME J. Turbomach.*, vol. 117, no. 4, pp. 639–646, 1995.
- [13] B. Zhao, C. Yang, S. Chen, M. Qi, and M. Zhou, "Unsteady flow variability driven by rotor-stator interaction at rotor exit," *Chinese J. Aeronaut.*, vol. 25, no. 6, pp. 871–878, 2012.
- [14] T. Shang, A. H. Epstein, M. B. Giles, and A. K. Sehra, "Blade row interaction effects on compressor measurements," *AIAA J. Propuls. Power*, vol. 9, no. 4, pp. 569–578, 1993.
- [15] Z. Wang, J. Hu, Y. Wang, and Y. Zhao, "Effect of upstream rotor on aerodynamic force of downstream stator blades," *Trans. Nanjing Univ. Aeronaut. Astronaut.*, vol. 23, no. 2, pp. 94–101, 2006.
- [16] D. E. Van Zante, J. J. Adamczyk, A. J. Strazisar, and T. H. Okiishi, "Wake recovery performance benefit in a high-speed axial compressor," *ASME J. Turbomach.*, vol. 124, no. 2, pp. 275–284, 2002.
- [17] P. Dregel and C. S. Tan, "Impact of rotor wakes on steady-state axial compressor performance," in *Proc. ASME 1996 International Gas Turbine and Aeroengine Congress and Exhibition*, Birmingham, UK, 1996.

- [18] P. G. Hill, U. W. Schaub, and Y. Sendo, "Turbulent wakes in pressure gradients," *ASME J. Appl. Mech.*, pp. 518–524, 1963.
- [19] D. E. Van Zante, "Study of a wake recovery mechanism in a high-speed axial compressor stage," Ph.D. dissertation, Department of Mechanical Engineering, Iowa State University, USA, 1997.
- [20] *Ansys CFX-Solver Theory Guide. ANSYS CFX Release 16.0.* Ansys Inc., Canonsburg, PA, 2015.
- [21] M. Raw, "Robustness of coupled algebraic multigrid for the Navier-Stokes equations," in *Proc. AIAA 34th Aerospace Sciences Meeting and Exhibit*, Reno, Nevada, USA, 1996.
- [22] C. Rhie and W. Chow, "Numerical study of the turbulent flow past an airfoil with trailing edge separation," *AIAA J.*, vol. 21, no. 11, pp. 1525–1532, 1983.
- [23] T. J. Barth and D. C. Jespersen, "The design and application of upwind schemes on unstructured meshes," in *Proc. 27th Aerospace Sciences Meeting*, Reno, Nevada, USA, 1989.
- [24] F. R. Menter, "Two-equation eddy-viscosity turbulence models for engineering applications," *AIAA J.*, vol. 32, no. 8, pp. 1598–1605, 1994.
- [25] M. Vahdati, A. I. Sayma, C. Freeman, and M. Imregun, "On the use of atmospheric boundary conditions for axial-flow compressor stall simulations," *ASME J. Turbomach.*, vol. 127, no. 2, pp. 349–351, 2005.
- [26] J. D. Denton, "The calculation of three dimensional viscous flow through multistage turbomachines," *ASME J. Turbomach.*, vol. 114, no. 1, pp. 18–26, 1992.
- [27] P. Galpin, R. Broberg, and B. Hutchinson, "Three-dimensional Navier Stokes predictions of steady state rotor/stator interaction with pitch change," in *Proc. 3rd Ann. Conference of the CFD Society of Canada*, Banff, Canada, 1995.

- [28] M. B. Giles, "Calculation of unsteady wake/rotor interaction," *AIAA J. Propuls. Power*, vol. 4, no. 4, pp. 356–362, 1988.
- [29] L. Zori, P. Galpin, R. Campregher, and J. C. Morales, "Time transformation simulation of 1.5 stage transonic compressor," in *Proc. ASME Turbo Expo*, Montreal, Canada, 2015.
- [30] J. D. Denton, "Loss mechanisms in turbomachines," *ASME J. Turbomach.*, vol. 115, no. 4, pp. 621–656, 1993.
- [31] L. H. Smith, "Wake ingestion propulsion benefit," *AIAA J. Propuls. Power*, vol. 9, no. 1, pp. 74–82, 1993.

Chapter 5

5 Conclusions and recommendations for future work

In this chapter, the conclusions of the thesis are discussed, followed by the recommendations for future work.

5.1 Conclusions

A commercial Computational Fluid Dynamics (CFD) solver was used to investigate the air flow in both a centrifugal and an axial transonic compressor stage of a turboprop aeroengine. Chapter 2 involved numerical investigation of the air flow in a centrifugal stage. A curvature and rotation correction of the shear stress transport (SST-CC) turbulence model was examined for the first time in a centrifugal stage. The model predictions were compared with those from the SST as well as the Speziale, Sarkar, and Gatski Reynolds stress model (RSM-SSG) and experimental data. The SST-CC showed better agreement in the pressure ratio with the experiments than the SST at high mass flow operating conditions (near choke). However, at low mass flow operating conditions (near stall), the SST showed better agreement with experiments than SST-CC. For the local flow field, both SST and SST-CC showed small differences in the velocity profiles at the interface between the impeller and the diffuser (mixing plane). Overall, both SST and SST-CC showed better agreement with experimental observations than the RSM-SSG. The turbulence production multiplier (f_{rl}) was tested at the sections of highest curvature and rotation effects. The SST-CC model improved the sensitivity of the turbulence production term to high levels of local curvature and rotation. This was examined by comparing with the RSM-SSG predictions. The abnormal variations in the f_{rl} term away from the compressor walls had insignificant effects since the turbulence production magnitudes were relatively low. The centrifugal compressor used in this study was dominated by curvature effects compared with rotation effects.

Chapter 3 discussed a new method developed to quantify the flow blockage in the axial transonic stage. This method generated a main flow direction based on a linear surface fit of velocity angles in all directions for the core flow region at a constant streamwise plane.

Therefore, this approach could be applied for axial and centrifugal stages. Both RANS and URANS solutions were used to predict the variation of a normalized blockage parameter with a loading parameter at the rotor tip. Both steady and unsteady predictions showed good agreement with the previous studies at different mass flow rate operating conditions. The highest levels of local flow blockage were found at the rotor tip and stator hub when the Peak Pressure Ratio (PPR) is reached which suggested that compressor stall might be initiated near the stator hub or near the rotor tip. By comparing the RANS and URANS predictions in terms of the total blockage at the PPR point, the URANS solutions gave higher total blockage, by 2.5%, at the rotor outlet plane and lower blockage, by 12%, at the stator outlet. The URANS simulations included the effect of the inlet guide vanes (IGV) wake on the rotor flow field which explained the increased rotor tip blockage when compared with the RANS predictions. The rotor wake migration considered in the URANS reduced the breakdown of the stator hub vortex, resulting in reduced stator blockage when compared with the RANS solution. For the High Efficiency point (HE), both RANS and URANS blockage predictions matched within 1%. On the other hand, RANS predicted a higher pressure ratio than URANS, by 3%, at the HE point. Although the values of the mass-averaged total pressure at the rotor inlet were identical for RANS and URANS, the difference in the local flow field at the rotor inlet were the main reason for the discrepancy in the total pressure ratio. The mixing plane approach used in RANS mixed out the effect of the upstream wake which led to a more uniform total pressure distribution and a higher pressure rise (i.e. by 3%).

Chapter 4 examined the effect of the axial gap between the rotor and stator of the transonic axial stage (R-S gap) on the local and global performance of the stage using URANS with the time transformation (TT) approach. In previous studies, it was claimed that reducing the axial gap between components improved the efficiency of the stage. However, in other studies, it was shown that a smaller axial gap led to higher losses and unsteady forces on the stator blade. Numerical investigations were carried out to clearly understand the influence of the axial gap between the rotor and stator on the global and local losses and unsteady forces on the stator blade. At the reduced mass flow point (PPR), the efficiency was reduced by 1.6% when the R-S gap is reduced by 40%. The stator passage exhibited

more total pressure losses when compared with the gap region. The stator suction surface boundary layer separation increased when the R-S gap was reduced resulting in more losses. At the PPR point, the unsteady forces on the stator blade were higher with the smaller gaps. However at the HE point, the largest gap showed the highest unsteady forces on the stator blade. There were no significant differences in the time-averaged forces with respect to the examined R-S gaps.

It has been suggested that reducing the axial gap improved the efficiency due to the reduction in viscous mixing of the rotor wake. Therefore, the decay of the rotor wake was studied to investigate the contribution of the viscous and stretching (reversible) mechanisms. The simple 2D model developed in previous studies showed that the majority of the wake decay in the stator passage was due to reversible stretching. The model predicted higher viscous decay with the smallest gap configuration at the PPR point. On the other hand, the viscous dissipation showed that the smallest gap had the highest wake recovery values. This could be due to a deeper initial wake for the small gap which enhanced viscous effects. A case with no downstream stator revealed that the rotor wake decay was slower than the cases with the stator. The viscous mixing was the only mechanism responsible for the wake decay for the case without the stator. Overall, for the small gap, the efficiency gain from wake recovery was insignificant compared to the losses due to boundary layer separation.

In conclusion, this work contributed to providing a better understanding of turbulence modelling and performance of state of the art centrifugal and axial aeroengine compressors. A curvature correction turbulence model is examined on the centrifugal stage. It was found to be both accurate and time efficient. A general blockage method was developed and examined on the axial stage. The method gave insight about the possible mechanisms of stall in the stage. The influence of the axial gap between the rotor and stator of the axial stage on the compressor global and local losses was investigated. The study provided a better understanding for the contribution of sources of losses in the axial stage.

5.2 Recommendations for future work

The centrifugal stage has been investigated by the steady RANS method. It is recommended to examine the performance of the turbulence models using the time transformation approach which allows modelling a single impeller passage and a single diffuser with unequal passage count. Another recommended turbulence model is the two-equation Explicit Algebraic Reynolds Stress Model (EARSM). This model includes the effects of the turbulence anisotropy without the need to solve the Reynolds stresses transport equations, therefore, it takes the same computational time as any two-equation model. However, due to the complexity of the model, care should be taken when initializing the solution.

The maximum limit of the production multiplier (1.25) is a case dependent value which is selected by the model developers. However, if a reference case, such as a Large Eddy Simulation (LES) solution is provided, a rescaling of the upper limit of the production multiplier might be needed.

The wakes of the IGV have shown a significant influence on the blockage calculations in the axial stage. The IGV wakes are rescaled according to the R-IGV blade count since the profile transformation is used at the R-IGV interface. The use of multiple time transformation (TT) at the IGV-R and R-S interfaces causes a discontinuity in the wake profile at the R-S interface. The newest version of ANSYS CFX (CFX 17.2) provides the capability to simulate two successive interfaces using the TT approach.

Blockage is the main cause of stall in compressors. The spike stall mechanism in a compressor stage is not fully understood. All the transient interface approaches are not designed to capture the initiation of stall since these methods are based on the periodicity of the solution. A full wheel simulation will not be feasible with a limited number of processors. The blade counts might be rescaled to reach a unity pitch ratio at the interfaces and, therefore, a reduced sliding mesh simulation can be carried out. The blade chord, tip gap, and blade angle should be redesigned to give the same blockage parameter as the

baseline design. In this way, the modified blade count design will be a good representation of the original design and more time saving in terms of spike stall investigation.

This work numerically investigated the first stage of a multistage compressor using 60 parallel processors for the URANS simulations. Each case took around 2-3 weeks to converge. In industrial applications, steady solutions (RANS) are implemented for the preliminary design phase. RANS predicts the time-averaged flow field while URANS can predict the wake effects and secondary flows. The compressor efficiency predictions are very sensitive to the modelling approach as has been shown in this study. Moreover, the effects of turbulent transition and turbulent scales are not captured by RANS and URANS which can influence the global performance predictions. A well-resolved LES will be capable of capturing the separations and spike stall more accurately. However, LES is not feasible for industrial applications due to its high computational cost (10,000 to 1000,000 times the cost of URANS). The computational cost ratio can be reduced by using the TT method along with LES but this will not be suitable for aperiodic phenomena such as spike stall. However, hundreds of processors will be needed for this purpose.

The IGV indexing with respect to the stator is the circumferential adjustment of the IGV blades while keeping the stator blades fixed. This process affects the IGV wake transport across the downstream components. It is recommended to investigate the effect of IGV indexing in regards to the R-S axial gap. The stator blade count, as well as the stator angle, is an interesting problem to be investigated with regards to the R-S gap. If the new TT method in CFX 17.2 is used at the IGV-R interface, the combined effect of the IGV-R and R-S gaps on the compressor performance and the wake decay is recommended for future research.

Appendices

Appendix A

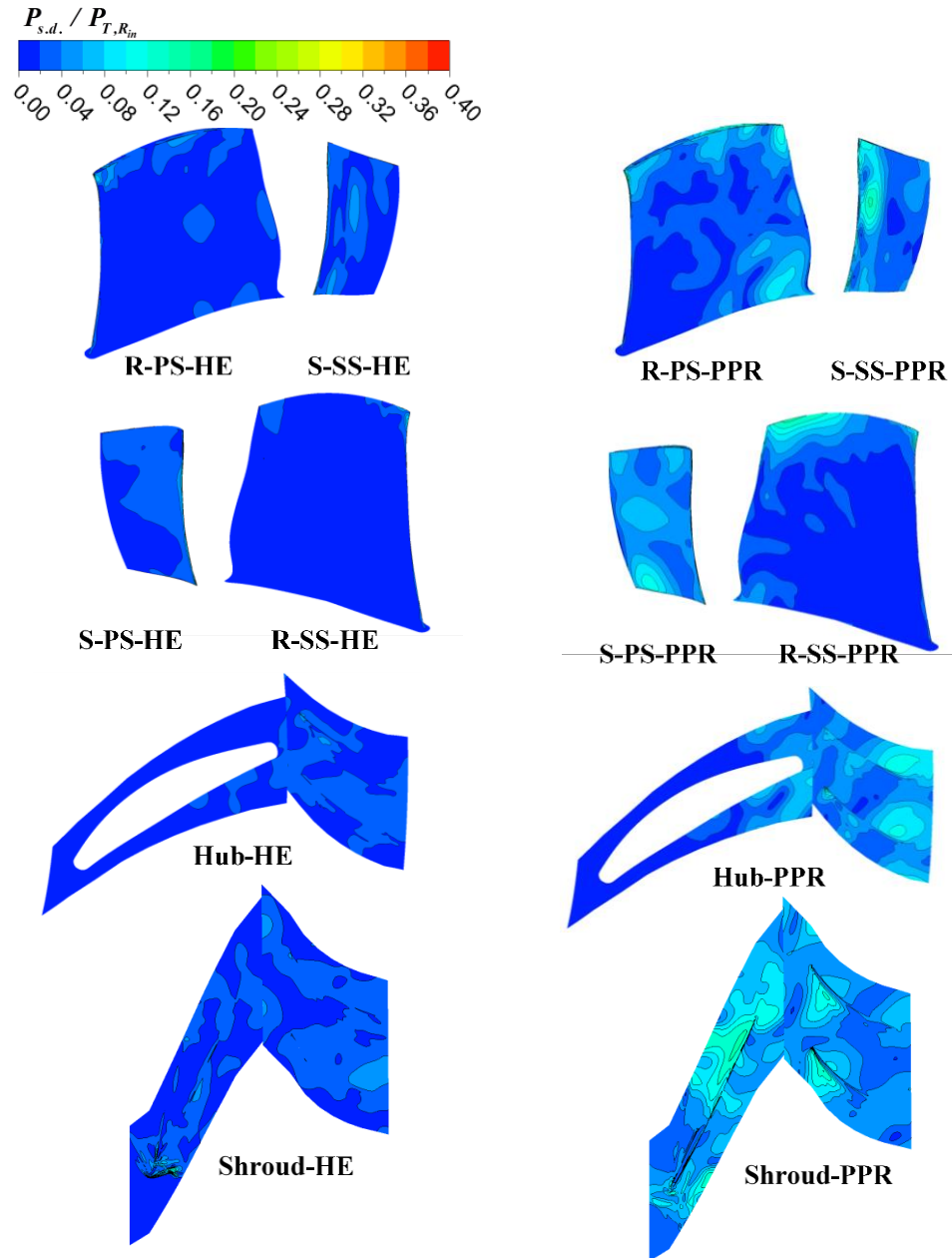


Figure A-1 Standard deviation of the pressure on the rotor and stator blades and on their hub and shroud at HE and PPR. The values are normalized by the rotor inlet total pressure.

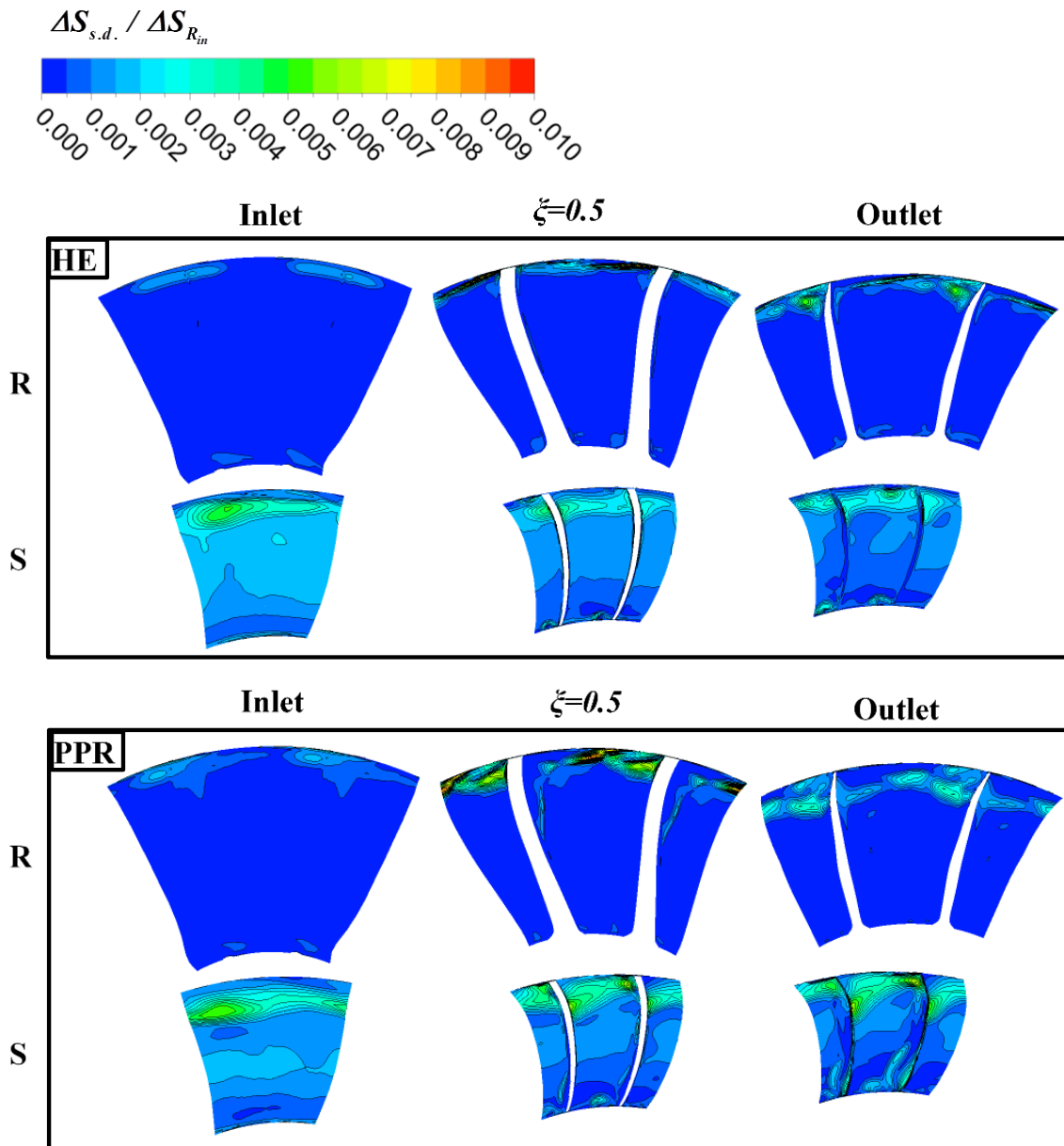


Figure A-2 Standard deviation of the entropy within the rotor and stator passages at HE and PPR. The values are normalized by the rotor inlet entropy.

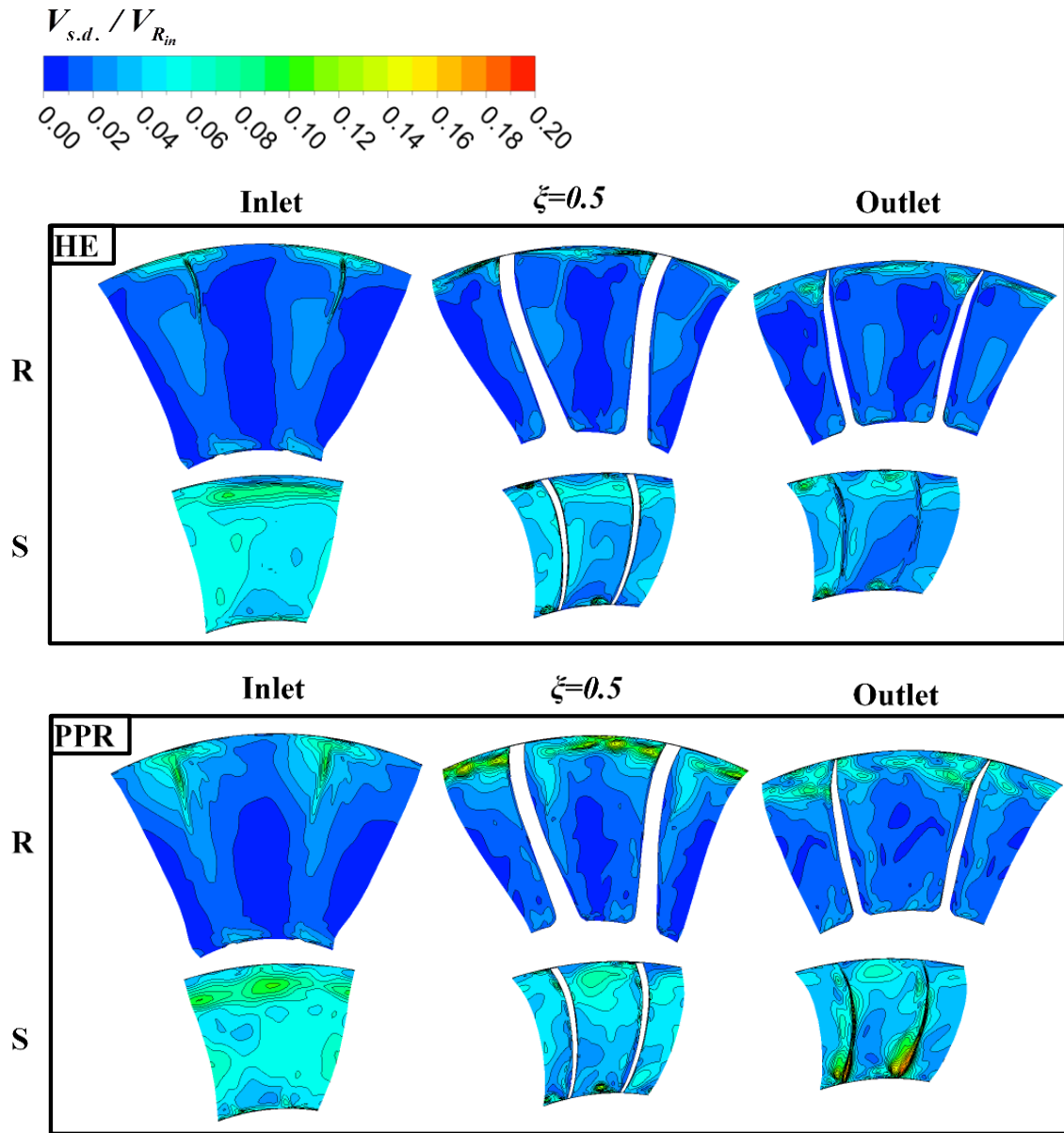


Figure A-3 Standard deviation of the velocity magnitude within the rotor and stator passages at HE and PPR. The values are normalized by the rotor inlet.

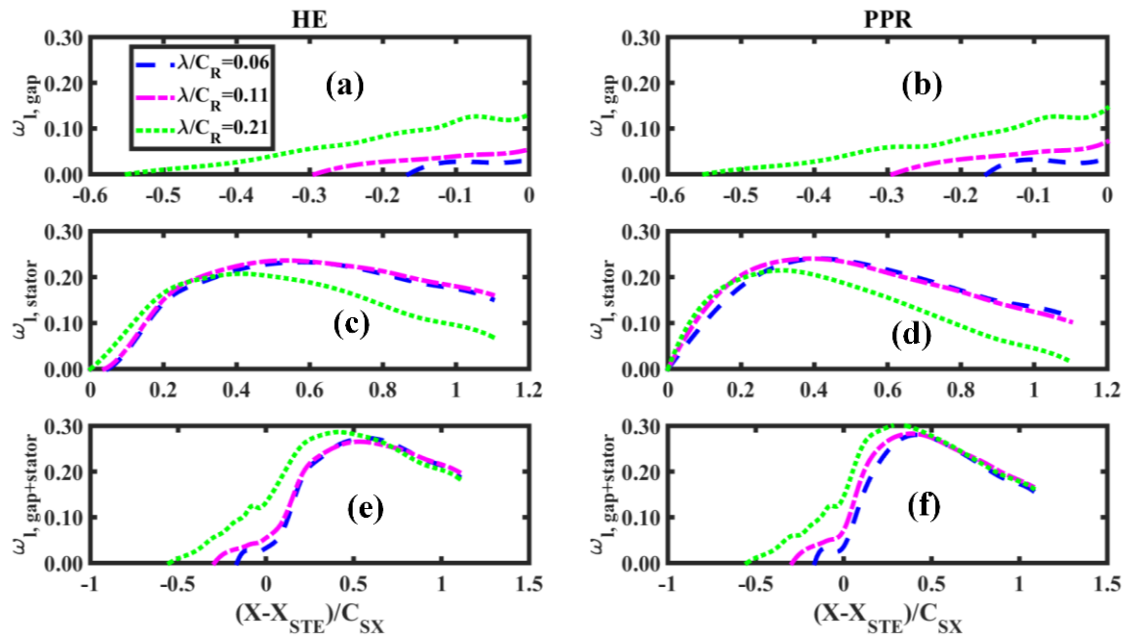


Figure A-4 Total pressure loss coefficient at 1% spanwise section for (a,b) the gap, (c,d) the stator and (e,f) the gap and stator combined. The left and right column figures are calculated at the HE and PPR points, respectively.

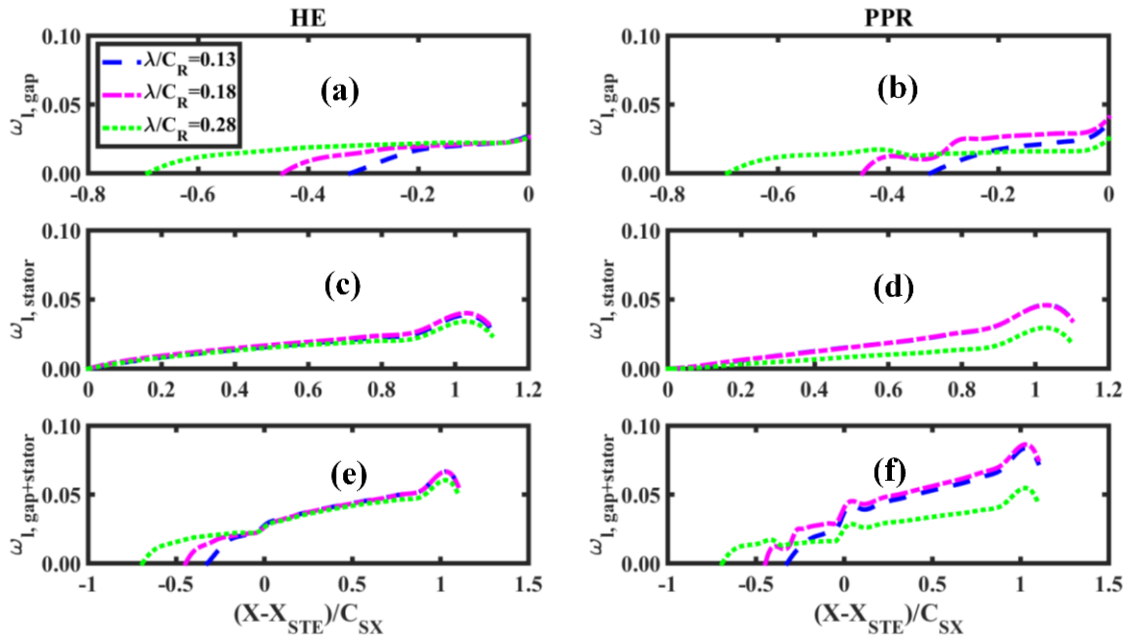


Figure A-5 Total pressure loss coefficient at 25% spanwise section for (a,b) the gap, (c,d) the stator and (e,f) the gap and stator combined. The left and right column figures are calculated at the HE and PPR points, respectively.

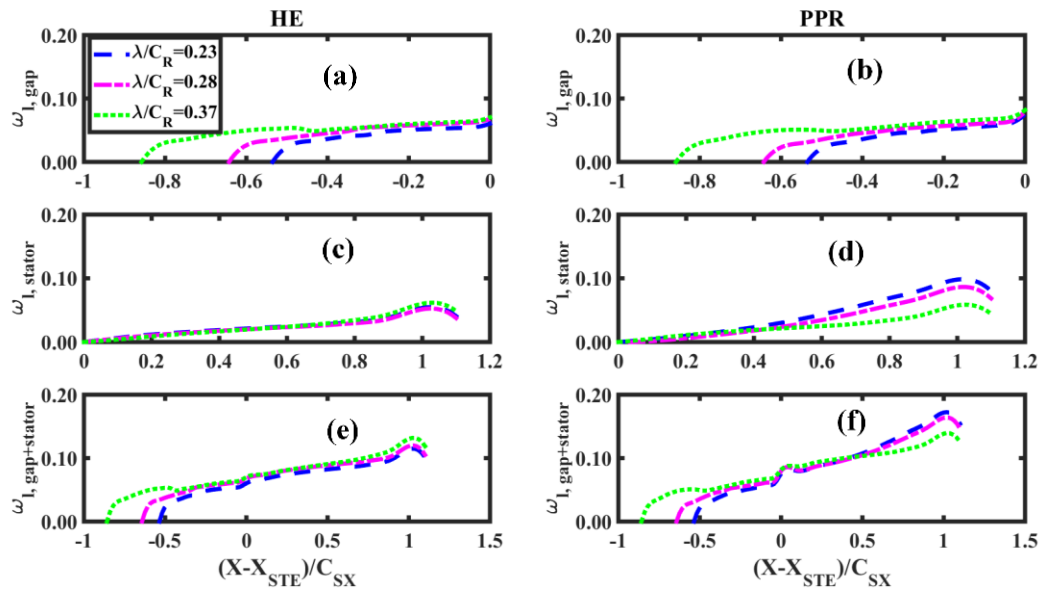


Figure A-6 Total pressure loss coefficient at 75% spanwise section for (a,b) the gap, (c,d) the stator and (e,f) the gap and stator combined. The left and right column figures are calculated at the HE and PPR points, respectively.

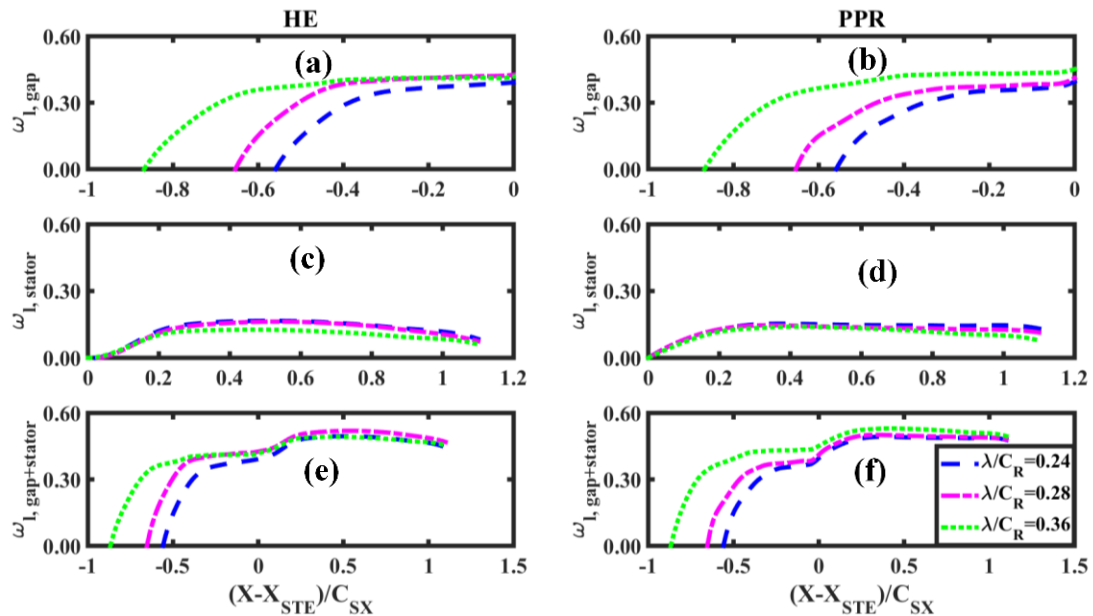


Figure A-7 Total pressure loss coefficient at 99% spanwise section for (a,b) the gap, (c,d) the stator and (e,f) the gap and stator combined. The left and right column figures are calculated at the HE and PPR points, respectively.

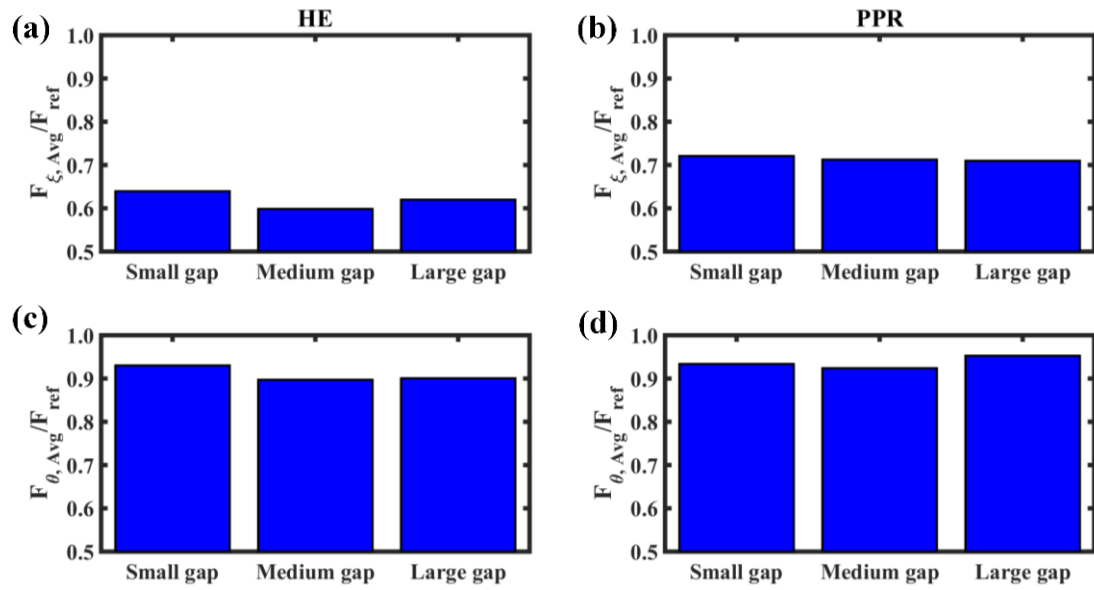


Figure A-8 The time average of the streamwise component (a b) and tangential component (c,d) of the total forces on the stator blade. The left and right column figures are calculated at the HE and PPR points, respectively.

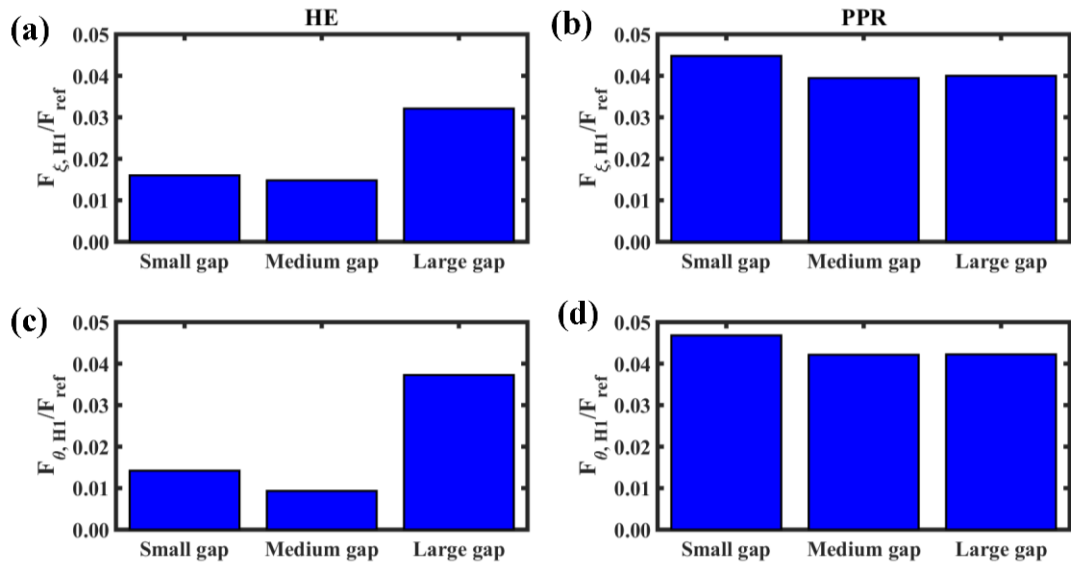


Figure A-9 The first Fourier harmonic of the streamwise component (a,b) and tangential component (c,d) of the total forces on the stator blade. The left and right column figures are calculated at the HE and PPR points, respectively.

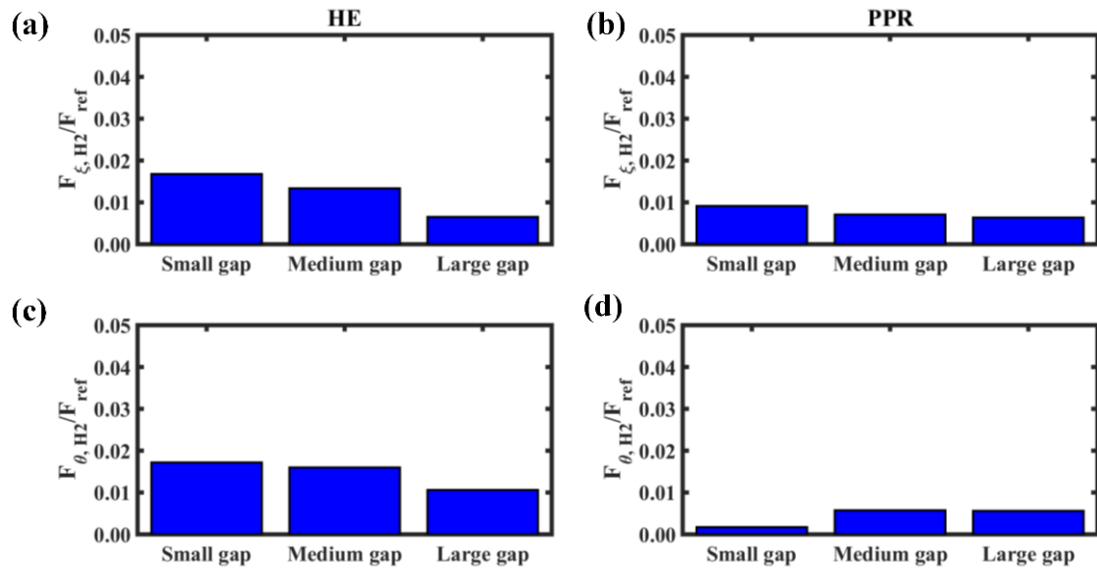


Figure A-10 The second Fourier harmonic of the streamwise component (a,b) and tangential component (c,d) of the total forces on the stator blade. The left and right column figures are calculated at the HE and PPR points, respectively.

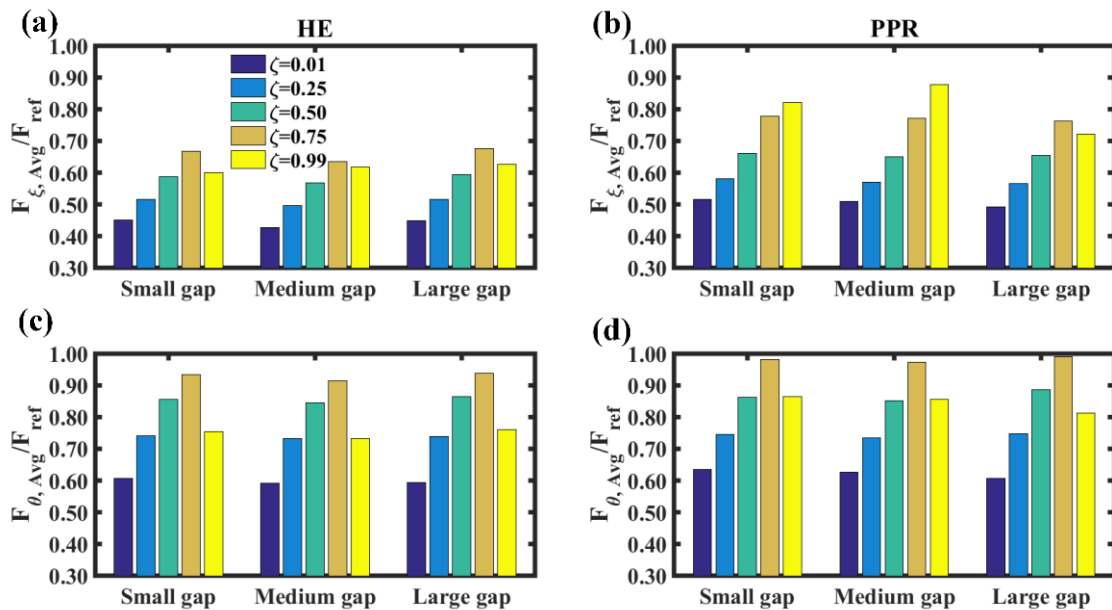


Figure A-11 The time average of the streamwise component (a,b) and tangential component (c,d) of the forces on the stator blade at spanwise locations of 1%, 25%, 50%, 75% and 99%. The left and right column figures are calculated at the HE and PPR points, respectively.

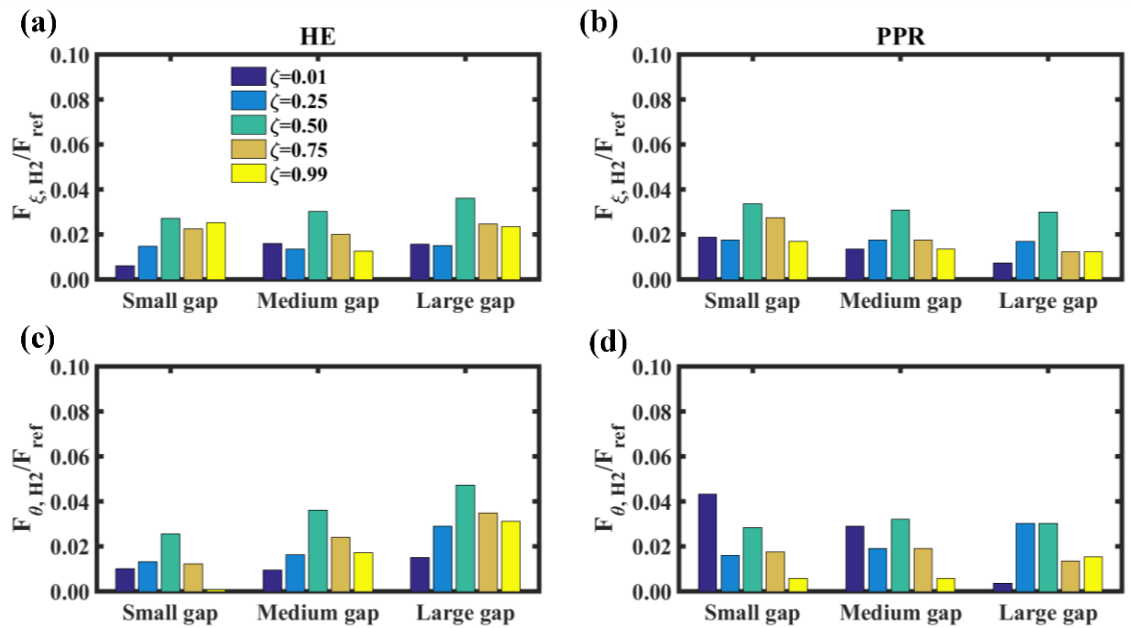


Figure A-12 The second Fourier harmonic of the streamwise component (a,b) and tangential component (c,d) of the forces on the stator blade at spanwise locations of 1%, 25%, 50%, 75% and 99%. The left and right column figures are calculated at the HE and PPR points, respectively.

Curriculum Vitae

Name: Shady Ali

**Post-secondary
Education and
Degrees:** Cairo University
Cairo, Egypt
2005-2009 B.A.

Cairo University
Cairo, Egypt
2009-2012 M.A.

The University of Western Ontario
London, Ontario, Canada
2012-present Ph.D.

**Related Work
Experience** Teaching and Research Assistant
The University of Western Ontario 2012-2016

Publications and Conferences:

S. Ali, K. J. Elliott, E. Savory, C. Zhang, R. J. Martinuzzi, and W. E. Lin, "Investigation of the performance of turbulence models with respect to high flow curvature in centrifugal compressors," *ASME J. Fluids Eng.*, vol. 138, no. 5, pp. 1–10, 2015.

S. Ali, E. Savory, and C. Zhang, "Numerical investigation of blockage development in an aeroengine transonic axial compressor stage," in *Proc. 25th Canadian Congress of Applied Mechanics (CANCAM)*, London, Ontario, Canada, 2015.

S. Ali, E. E. Khalil, and M. A. Fouad, "Effect of fire locations on the performance of impulse ventilation system in an underground car park," in *Proc. 51st AIAA Aerospace Sciences Meeting including the New Horizons Forum and Aerospace Exposition*, Grapevine (Dallas/Ft. Worth Region), Texas, USA, 2013.

S. Ali and E. E. Khalil, "Numerical investigation of impulse ventilation for smoke control in an underground car park," in *Proc. 10th International Energy Conversion Engineering Conference*, Atlanta, Georgia, USA, 2012.